PREDICTING AND MONITORING DRAINAGE CHEMISTRY DURING MINERAL WEATHERING FOR CO_2 SEQUESTRATION

A thesis submitted to Committee of Graduate Studies in Partial Fulfillment of the Requirements for the Degree of Master of Science in the Faculty of Arts and Science

TRENT UNIVERSITY
Peterborough, Ontario, Canada

Environmental and Life Sciences M.Sc. Graduate Program
May 2023

ABSTRACT

Predicting and monitoring drainage chemistry during mineral weathering for CO_2 sequestration

Duncan Thomas Emil McDonald

Mineral feedstocks, including alkaline mine wastes, can sequester CO_2 as a dissolved phase (e.g., HCO_3^-) or a solid carbonate via enhanced rock weathering (ERW). For this thesis, the release of easily accessible Ca and Mg from non-carbonate sources was determined for kimberlite residues from several diamond mines and commonly proposed ERW rock types, including wollastonite and olivine. Batch leaches determined the CO_2 sequestration potentials of kimberlites to be in the range of 3–12 kg CO_2/t, which was exceeded by most ERW feedstocks. Leaches also assessed the release of Ni and Cr, elements of concern in ERW settings, and P and K, which benefit agricultural soils. Year-long leaching columns were deployed using kimberlite from the Gahcho Kué and Venetia diamond mines, wollastonite skarn, and olivine sand from the initial assessment. The kimberlite residues sequestered 0.03 kg CO_2/t as dissolved inorganic carbon and 0.6 kg CO_2/t as solid total inorganic carbon. Weathering of wollastonite skarn resulted in CO_2 removal rates via mineral trapping of CO_2 of 6.31 kg CO_2/t, while the olivine sand yielded rates of 0.5 kg CO_2/t via solubility trapping. Both methodologies used in this study demonstrated value in the prediction and monitoring of drainage chemistry as it relates to ERW and CO_2 mineralization. Implementation of these strategies can progress ERW efforts by providing confidence in feedstock selection and the verification of carbon offsets.

Keywords: Mine wastes, CO_2 mineralization, enhanced weathering, drainage chemistry, CO_2 fluxes, mineral trapping, solubility trapping, CO_2 sequestration, leaching columns, carbon accounting

Co-authorship statements

Contributors to Chapter 2 include D.T.E. McDonald, I.M. Power, C. Paulo, A.R. Stubbs, J.A. Lockhart, and S.A. Wilson. McDonald prepared samples for characterization analysis, performed total inorganic analysis, conducted experiments, interpreted the data, prepared figures, and wrote the chapter. Paulo conducted surface area analysis and developed the experimental design. Power conceptualized the study and supervised on all aspects of this chapter. Stubbs provided characterization data for mineral samples. Lockhart conducted particle area analyses and Wilson conducted quantitative X-ray diffraction analyses.

Contributors of Chapter 3 include D.T.E. McDonald, I.M. Power, and C. Paulo. McDonald conducted the experiments, performed analyses wrote the chapter, prepared figures, and analyzed the data. Power designed the columns, conceptualized the study, and oversaw on all aspects of this chapter. Paulo assisted in experimental design, data analysis and interpretation.

Acknowledgments

Funding was provided by the Natural Science and Engineering Research Council Grant to I.M. Power. I would like to state my profound appreciation of my supervisor, Ian Power, who has made such a positive impact on my life over the past 4 years. Being hired by Ian as a research assistant in the PowerGeolab in the Fall of 2018 has been a more significant event than I ever could have imagined and changed the course of my educational career for the better, more than once. Ian has proven to be an exceptional supervisor and role model, time and time again, and will continue to inspire me once my time in his lab is done. In addition, thank you to Dr. Huy Dang for being on my supervisory committee members, and for all the assistance and expertise provided along the way.

I would also like to recognize everything Carlos Paulo has done for me over the past 4 years but am afraid the page count would exceed both of my experimental chapters. Carlos has not only been instrumental in the progress of my education, but has also been a role model for me, and I hope to remain connected in the future.

My lab mates over the past number of years have made significant contributions to my research, and my enjoyment of the process. Thank you, Zivi, for helping take flux measurements, micronize samples, run carbon analysis, and for looking after my cats while I was away. Thank you to Justin for all your help with XRD patterns, particle size analysis, and planning our trip to the Yukon. Thank you, Kwon, for your help with alkalinity analysis and dismantling my columns.

I would also like to thank Bob Vasily of Canadian Wollastonite, Ryan Brophy of V6 agronomy, and De Beers Group of Companies, for providing the rock and mineral samples that made this research possible.

Finally, I would like to thank my family and friends for their unwavering support and encouragement, which means so much to me. To my parents, Tom, and Karen, thank you for the constant encouragement and support – none of this would have been possible without you. To my brothers, Sam, and Trevor, thanks for the laughs. Finally, a very special thank you to my cats, Ellie, and Burrow.

Table of Contents

Abstract ii
Co-authorship Statements iii
Acknowledgements iv
Table of Contents vi
List of Figures vii
List of Tables xi
List of Abbreviations and Symbols xii

Chapter 1: Introduction
1.1 Climate change and the need for carbon dioxide removal 1
1.2 Fundamental processes of ERW 2
1.3 Enhanced rock weathering 5
1.4 CO_2 sequestration via weathering of mine wastes 11
1.5 Drainage chemistry and the characterization of mine wastes 13
1.6 Research objectives 16
1.7 References 18

Chapter 2: CO_2 batch leaches for evaluating reactivity and element release from enhanced rock weathering feedstocks
2.1 Introduction 28
2.2 Methods 32
2.2.1 Sample acquisition and preparation 32
2.2.2 Particle size and surface area 32
2.2.3 Mineralogical analysis 33
2.2.4 Geochemical analysis 33
2.2.5 CO_2 batch leaches 35
2.3 Results 37
2.3.1 Characterization 37
2.3.2 Batch leaches 45
2.4 Discussion 50
2.4.1 Mineral dissolution and cation release 50
2.4.2 CO_2 sequestration 58
2.4.3 Deleterious metals 66
2.4.4 Nutrients 72
2.4.5 Feedstock comparison and implications 77
2.5 Conclusion 83
2.6 References 85

Chapter 3: Field-deployable drainage columns for monitoring enhanced weathering of kimberlite, olivine, and wollastonite

3.1 Introduction 99
3.2 Methods 103
3.2.1 Column design 103
3.2.2 Experimental methods 104
3.2.3 Column characterization 107
3.2.4 Water analysis 108
3.2.5 CO_2 fluxes and measurements 110
3.2.6 Solid analysis 111
3.2.7 PHREEQC modelling 112
3.3 Results 113
3.3.1 Water chemistry 113
3.3.2 CO_2 fluxes and pore gas concentrations 122
3.3.3 Total inorganic carbon of final solids 128
3.4 Discussion 130
3.4.1 Weathering processes 130
3.4.2 CO_2 removal and carbon accounting 139
3.4.3 Implications 149
3.5 Conclusion 157
3.6 References 158

Chapter 4: Conclusions

4.1 Summary of research outcomes 173
4.2 Applications of experimental apparatus 175
4.3 Applications of feedstocks 176
4.3.1 Mining 176
4.3.2 ERW 177
4.4 Suggestions for future research 178
4.5 References 180

List of Figures

Figure 2.1. Proportions of Si, Ca, and Mg in samples as determined using XRF. 42

Figure 2.2. Leached Ca (A), Mg (B), and Si (C) compared between kimberlite and other rock types. Concentrations are represented as the mass of the cation released per mass of sample in g/kg. Results are an average of triplicate leaches with standard deviation presented as error bars. 46

Figure 2.3. Comparison of TIC (%) in feedstocks pre- and post-leach. Values are an average of triplicate leaches with standard deviations being represented with error bars 47

Figure 2.4. Changes in pH values observed in initial leaching solution and final solution post-leach. Initial values of 3.9 are determined through PHREEQC, and final values are an average of n=3 with error bars representing the standard deviation. 47

Figure 2.5. Phosphorus (A) and potassium (B) leached from the sample, represented as the mass of the cation released per mass of sample (mg/kg). Results are an average of triplicate leaches with standard deviations represented with error bars. 48

Figure 2.6. Nickel (A) and chromium (B) leached from the sample, represented as the mass of the cation released per mass of sample (mg/kg). Results are an average of triplicate leaches with standard deviations represented error bars. 49

Figure 2.7. A) Maximum capacity for CO_2 sequestration based on whole rock geochemistry assuming 100% carbonation of Ca and Mg from non-carbonate sources to form a carbonate with a 1:1 cation: carbon molar ratio. B) CO_2 sequestration potential of feedstocks based on easily extractable cations, assuming 100% conversion of Ca and Mg released to form carbonates with a 1:1 molar ratio, corrected for Ca and Mg contributions from carbonate sources. Values are an average of triplicate leaches with standard deviations being represented with error bars. 60

Figure 2.8. Maximum capacity for CO_2 sequestration versus potential for CO_2 sequestration based on easily extracted cations from non-carbonate sources. Potential values are an average of triplicate leaches with standard deviations represented with error bars. 60

Figure 2.9. The concentrations of Ni (A) and Cr (B) that comprise the geochemistry of each feedstock plotted versus the amount of each element released during the leaches, indicating the feedstocks ability to provide the nutrients that they contain. 68

Figure 2.10. Concentration of Ni and Cr found in the whole rock geochemistry of kimberlite samples in the GEOROC database and their averages (n=88), and the concentration of each element found in our kimberlites. 70

Figure 2.11. The concentrations of P (A) and K (B) that comprise the geochemistry of each feedstock plotted against the amount of each element released during the leaches, indicating the feedstock's ability to provide the nutrients that they contain. 77

Figure 2.12. Concentration of P and K found in the whole rock geochemistry of kimberlite samples in the GEOROC database and their averages (n=1830), and the concentration of each element found in out kimberlites. 75

Figure 3.1. Precipitation and temperature data for the lab and outdoor phases. The outdoor phase data was obtained from the Trent Weather Monitoring Station. 108

Figure 3.2. Ca, Mg, and Si concentrations (A), DIC (B), and pH values (C) of the discrete leachate samples for GK columns. Gaps in the data occur when there was no drainage to collect. Reservoir water samples of the lab and outdoor phases are represented by symbols that do not connect to the lines. 114

Figure 3.3. Ca, Mg, and Si concentrations (A), DIC (B), and pH values (C) of the discrete leachate samples for DVK columns. Gaps in the data occur when there was no drainage to collect. There was not a lab phase for the DVK columns. Reservoir water samples of the outdoor phase is represented by symbols that do not connect to the lines. 116

Figure 3.4. Ca, Mg, and Si concentrations (A), DIC (B), and pH values (C) of the discrete leachate samples for WOL columns. Gaps in the data occur when there was no drainage to collect. Reservoir water samples of the lab and outdoor phases are represented by symbols that do not connect to the lines. 117

Figure 3.5. Ca, Mg, and Si concentrations (A), DIC (B), and pH values (C) of the discrete leachate samples for OLI columns. Gaps in the data occur when there was no drainage to collect. Reservoir water samples of the lab and outdoor phases are represented by symbols that do not connect to the lines. 119

Figure 3.6. The average (n=2) amount of K (A) and P (B) released each column type (mg/kg) during the lab and outdoor phases, represented by bars (Y-axis). The average concentration of each element in reservoir leachates (mg/L for K and µg/L for P) are represented by circles on the secondary Y-axis. 121

Figure 3.7. The average (n=2) amount of Ni (A) and Cr (B) released from each column type (µg/kg) during the lab and outdoor phases, represented by bars (Y- 122

axis). The average concentrations of each element in the reservoir leachate (μg/L) are represented by circles on the secondary Y-axis.

Figure 3.8. 1) CO_2 flux (g $CO_2/m^2/yr.$), water saturation (%), and temperature (ºC) data for GK1 (A) and GK2 (B) columns. Positive and negative values represent effluxes and influxes of CO_2, respectively. Blue and red lines represent the water saturation and temperature of the solids, respectively. 2) Pore CO_2 concentrations (ppm) as measured using a soil gas lance and Vaisala CO_2 meter. 123

Figure 3.9 1) CO_2 flux (g $CO_2/m^2/yr.$), water saturation (%), and temperature (ºC) data for DVK1 (A) and DVK2 (B) columns. Positive and negative values represent effluxes and influxes of CO_2, respectively. Blue and red lines represent the water saturation and temperature of the solids, respectively. 2) Pore CO_2 concentrations (ppm) as measured using a soil gas lance and Vaisala CO_2 meter. 125

Figure 3.10. 1) CO_2 flux (g $CO_2/m^2/yr.$), water saturation (%), and temperature (ºC) data for WOL1 (A) and WOL2 (B) columns. Positive and negative values represent effluxes and influxes of CO_2, respectively. Blue and red lines represent the water saturation and temperature of the solids, respectively. 2) Pore CO_2 concentrations (ppm) as measured using a soil gas lance and Vaisala CO_2 meter. 126

Figure 3.11. 1) CO_2 flux (g $CO_2/m^2/yr.$), water saturation (%), and temperature (ºC) data for OLI1 (A) and OLI2 (B) columns. Positive and negative values represent effluxes and influxes of CO_2, respectively. Blue and red lines represent the water saturation and temperature of the solids, respectively. 2) Pore CO_2 concentrations (ppm) as measured using a soil gas lance and Vaisala CO_2 meter. 127

Figure 3.12. The total inorganic carbon (%C) measured at each layer of the column after the conclusion of the experiment for GK (A), DVK (B), WOL (C), and OLI (D). Open symbols represent column 1 of that type, and closed symbols represent column 2. Triplicate measurements were performed at each horizon, with each symbol representing one value. Average initial TIC values (n=3+) are represented by a solid grey line, with those values standard deviation represented by dotted grey lines 129

Figure 3.13. Forecasted CO_2 sequestration at the Gahcho Kué Diamond Mine, based on the rates reported in this study and publicly available mine operations data. 152

List of Tables

Table 2.1. Sample inventory of feedstocks analyzed in this chapter, including their background and physical characteristics. 32

Table 2.2. Quantitative mineralogy (wt.%) for kimberlite residue samples. 38

Table 2.3. Quantitative mineralogy (wt.%) for other rock samples. 38

Table 2.4. Geochemical composition (wt.%) determined by XRF and carbon coulometry. 40

Table 2.5. Trace element abundances in solid samples as determined by 4-acid digestion and ICP-MS 43

Table 2.6. Summary of initial concentrations, and the percentage that was lost during leaches. 44

Table 2.7. Summary of the key results from the kimberlite leaching tests. Each feedstock has been given a relative grade on their use for CO_2 sequestration, release of elements of concern (EOC), and elements of interest (EOI). Three grade levels are employed, with "+" representing the worst, and "+ + +" representing the best. 81

Table 2.8. Summary table of key results of kimberlites used in Chapter 2. Each feedstock has been given a grade based on their results for the parameters of CO_2 sequestration, elements of concern (EOC), and elements of interest (EOI). Three grade levels are employed, with "+" representing the worst, and "+ + +" representing the best. 82

Table 3.1. The physical properties of the columns, and the geochemical composition and mineralogy of the materials used. Precipitation includes the total water additions during the lab phase and rainfall during the outdoor phase. Drainage is the total amount of water that passed through each column during both phases, including sample and reservoir waters. Target minerals identified include potential sources of Ca and Mg and the wt.% they constitute in the solids. 106

Table 3.2. Saturation indices of aragonite, calcite, hydromagnesite, and amorphous silica in the reservoir waters sampled at the conclusion of the lab phase (LP) and outdoor phase (OP). Values are an average of the two columns of each type. 119

Table 3.3. Average (n=2) CO_2 sequestration rates based on changes observed in DIC (solubility trapping) and TIC (mineral trapping) for each column. Negative values indicate the storage of CO_2, while positive values indicate the loss of CO_2 from the material. 132

Table 3.4. Average (n=2) CO_2 sequestration rates (g CO_2/kg) based on changes observed in DIC (solubility trapping) and TIC (mineral trapping) for each column. Positive values indicate the storage of CO_2, while negative values indicate the loss of CO_2 from the material. 140

Table 3.5. Summary of carbon verification methods, including their advantages, disadvantages, and examples of how each affected result 154

List of Abbreviations and Symbols

ERW	Enhanced rock weathering
CDR	Carbon dioxide removal
NET	Negative emissions technology
BET	Brunauer–Emmett–Teller
cm	Centimetres
Gt	Gigatonnes
IPCC	Intergovernmental Panel on Climate Change
M	Molarity
Min	Minute
mL	Millilitre
mm	Millimetre
mol	Moles
Mt	Megatonne
pH	$-\log[H^+]$
ppm	Parts per million
ppb	Parts per billion
s	Seconds
TIC	Total inorganic carbon
DIC	Dissolved inorganic carbon
wt.%	Weight percent
XRD	X-ray diffraction
XRF	X-ray fluorescence
°C	Celsius (degrees)
Δ	Delta
µL	Microlitre
mg	Milligram
kg	Kilogram
t	Tonne
µm	Micrometre
yr	Year

Chapter 1
Introduction

1.1 Climate change and the need for carbon dioxide removal

The increase in atmospheric CO_2 caused by anthropogenic greenhouse gas emissions has led to a global rise in temperature that surpassed 1 °C in 2017 and continues to rise at a rate of 0.2 °C a decade (IPCC, 2018). This is a result of the concentration of atmospheric CO_2 increasing from 280 ppm in 1750 (IPCC, 2018) to 417 ppm in 2020 (NOAA 2020). The Intergovernmental Panel on Climate Change (IPCC) states that global warming needs to be limited to a maximum of 1.5 °C above Earth's average preindustrial temperature (IPCC, 2018). A drastic reduction in CO_2 emissions is necessary, but natural CO_2 drawdown and switching to green energy and technologies will be insufficient to meet targets (Broecker, 2007). The current carbon budget states that no more than 200 Gt CO_2 can be emitted before every additional tonne needs to be offset to meet the target of 1.5 °C (Minx et al., 2017).

All potential pathways to limit global warming below 1.5 °C without overshooting require large-scale carbon dioxide removal (CDR) and a period of net-negative emissions at some point in the 21st century (Beuttler et al., 2019). In response to this challenge, a less ambitious goal of 2 °C has been proposed by the IPCC that still requires net-zero CO_2 emissions this century, aided by long-term net-negative carbon emissions on the scale of -26 Gt CO_2/yr (Sanderson et al., 2016). With the need for negative emissions technologies (NETs) becoming essential for keeping human-induced warming below either of the two targets, further research and development of these processes needs to

occur. Proposed NETs and CDR approaches include afforestation/reforestation, bioenergy with carbon capture and storage (BECCS), direct air capture and storage (DACS), ocean fertilization, and enhanced rock weathering (Beuttler et al., 2019; Minx et al., 2017).

Enhanced rock weathering (ERW) sequesters CO_2 though the conversion of its gaseous form in the atmosphere, to a stable aqueous form (typically bicarbonate), and potentially a solid phase (carbonate minerals). This process relies on the dissolution of finely ground mineral feedstocks that have been dispersed over large areas and allowed to react with CO_2 equilibrated rainwater. Weathering products in solution are transported through groundwater and runoff to the oceans where they provide a long-term sink of atmospheric CO_2. ERW as a NET is predicated on accelerating natural silicate weathering that occurs passively at an approximated rate of 0.3 Gt CO_2/yr in natural settings (Hartmann et al., 2013; Moosdorf et al., 2014). Passive weathering has also been observed in disturbed environments like in mine residues (Mervine et al., 2018; Stubbs et al., 2022; Wilson et al., 2014), making the facilities that currently holds these materials a prospective location for large scale deployment of ERW technologies (Power et al., 2014). There is currently no single NET that has the capacity to remove CO_2 from the atmosphere at a rate and scale needed to meet the targets (Minx et al., 2017), but ERW has the potential to contribute large offsets of CO_2 at low cost and energy.

1.2 Fundamental processes

CO_2 sequestration via ERW is largely dependent on the mineralogical composition of the powdered rock. Mafic and ultramafic (Mg-rich) rocks have received most of the

attention, but Ca-rich rocks are also being investigated as a potential feedstock. Proposed rock and minerals for ERW and CO_2 mineralization include olivine (Renforth et al., 2015a; ten Berge et al., 2012), wollastonite (Di Lorenzo et al., 2018; Haque et al., 2020b, 2019), brucite (Harrison et al., 2013), serpentinite (Daval et al., 2013; Power et al., 2020), basalt (Lefebvre et al., 2019; Oelkers et al., 2008), and kimberlite (Mervine et al., 2018; Paulo et al., 2021; Wilson et al., 2011).

The dissolution rates of minerals will directly affect the rates of CO_2 removal and can vary by orders of magnitude. Dissolution rates are influenced by solution chemistry, mainly pH. Generally, minerals will dissolve faster at lower pH values regardless of crystal chemistry (Power et al., 2013), due to the liberation of cations and their replacement with H^+ ions, as seen in the dissolution of forsterite (Eq. 1), which for example, can lead to the complete dissolution of minerals in acidic solutions (Teir et al., 2007).

$$Mg_2SiO_{4(s)} + 4H^+ \rightarrow 2Mg^{2+} + H_4SiO_4 \quad (1)$$

Proposed methods for pH adjustments have been investigated and include amending ultramafic tailings with acid-generating bacteria (Power et al., 2010), inclusion of sewage sludge in mine waste facilities (Forsberg and Ledin, 2006), and CO_2 injection (Gislason et al., 2010).

Crystal chemistry is also an important factor affecting dissolution rates and ultimately rates of sequestration. The dissolution rate is reliant on the destruction of metal/metalloid-oxygen bonds (e.g. Si-O), which results in faster rates of dissolution in single oxide minerals like brucite [$Mg(OH)_2$) compared to multi-oxide minerals including olivine, pyroxene, and aluminosilicates (Schott et al., 2009). In the structure of a silicate

mineral the hardest bond to break is typically the Si-O bond, which leads to rates being dependent on silica polymerization, which is the average number of Si-O-Si bonds in the crystal structure (Schott et al., 2009). Orthosilicates including forsterite are unpolymerized and display rates of dissolution that are higher than polymerized phyllosilicates such as diopside and enstatite (Brantley, 2008; Schott et al., 2009). Brucite has no Si-O bonds and therefore has a dissolution rate that is orders of magnitude faster than Mg-silicate minerals (Pokrovsky and Schott, 2004).

The availability of CO_2 can act as a limiting factor for ERW when its supply does not allow for the solubilization of CO_2 (Harrison et al., 2013; Wilson et al., 2010). Aqueous CO_2 in equilibrium with the atmosphere (Eq.2) can disassociate to form carbonic acid (Eq. 3), which when consumed by the neutralization of a solid base (Eq. 1) can lead to the formation of bicarbonate (HCO_3^-) and carbonate (CO_3^{2-}) anions in solution (Eq. 4, 5). These anions can be used as a stable sink of CO_2 or reacted with cations released through dissolution (Eq. 1) to precipitate a stable phase of carbonate minerals such as calcite, under specific conditions (Eq. 6).

$$CO_{2(g)} \leftrightarrow CO_{2\,(aq)} \quad (2)$$

$$CO_{2\,(aq)} + H_2O \leftrightarrow H_2CO_3 \quad (3)$$

$$H_2CO_3 \leftrightarrow H^+ + HCO_3^- \quad (4)$$

$$HCO_3^- \leftrightarrow H^+ + CO_3^{2-} \quad (5)$$

$$Ca^{2+} + CO_3^{2-} \text{ « } CaCO_3 \quad (6)$$

The two key processes for carbonate precipitation include 1) the formation of a stable nucleus, which is controlled by the saturation index and temperature, and 2) crystal growth, which is a function of reactive surface area of the mineral and the solution

chemistry (Giammar et al. 2005; Morse et al., 2007). The rate of secondary carbonate precipitation is limited by the solution's saturation state (Saldi et al., 2012), which partly depends on available cations. Thus, primary mineral dissolution is an essential consideration of CO_2 mineralization. Generally, mineral dissolution will be rate-limiting with recalcitrant silicates (e.g. multi oxide silicates), while CO_2 supply will be rate-limiting with highly reactive phases. At Earth's surface conditions, calcite ($CaCO_3$) can precipitate if solutions are saturated; however, anhydrous magnesium carbonate minerals including magnesite ($MgCO_3$) and dolomite [$MgCa(CO_3)_2$] are limited by slow precipitation kinetics, resulting in the prevalence of hydrated phases (Case et al., 2011; Hänchen et al., 2008; Power et al., 2017). While solubility trapping remains the focus of most ERW studies, potential secondary carbonate minerals to form out of solution that may be used for CO_2 removal include but are not limited to: calcite, hydromagnesite ($Mg_5[CO_3]_4[OH]_2 \cdot 4H_2O$), aragonite ($CaCO_3$), and trona ($Na_2CO_3 \cdot NaHCO_3 \cdot 2H_2O$).

1.3 Enhanced rock weathering

Enhanced rock weathering is the process of accelerating reactions between CO_2 and Mg- and Ca-rich rocks with the goal of sequestering atmospheric CO_2 and stabilizing climatic conditions (Beerling et al., 2018). This approach involves enhancing natural weathering by pulverizing appropriate rock types, often ultramafic and mafic rocks, and widely dispersing this powder to maximize exposure to CO_2, which can be stored as either a dissolved or solid phase (Assima et al., 2014; Beerling et al., 2018; Bach et al., 2019). The natural process that ERW aims to accelerate results in an increase of dissolved inorganic carbon (DIC) in the waters, in the form of bicarbonate, via pH neutralization,

which can then be transported to oceans via runoff and subsurface flow (Berner, 2003). These processes are a major part of Earth's natural carbon cycle, currently removing ~1.1 Gt CO_2/yr from the atmosphere (Amann et al., 2020; Strefler et al., 2018a). These processes represent long-term cycling of carbon and must be accelerated to fit the application of meeting target concentrations of CO_2 in the atmosphere. The idea of ERW addresses the need for accelerating weathering rates through the application of powdered rocks and minerals to terrestrial or marine environments to increase dissolution and ultimately, CO_2 consumption (Hartmann et al., 2013).

Well-informed feedstock selection via thorough characterization is critical to optimize the benefits of ERW. The ideal feedstock would be readily available, have high concentrations of Ca and Mg found in reactive minerals, contain little or no total inorganic carbon (TIC), have nutrients (e.g., P, K) that could be a co-benefit to soils, and no elements of concern (e.g., Ni, Cr). Feedstocks are often selected based on their geochemical parameters, which cannot be changed, but physical attributes like grain size can be optimized for increased ERW suitability. Grain size is important due to its relation to surface area, and thus dissolution rates. As a result, fine milling of minerals can enhance rates of CO_2 drawdown that greatly exceed those of coarser materials (Rigopoulos et al., 2018). It has been estimated that when basalt is allowed to weather over 10 years it will dissolve by 99.9% when milled to a grain size of <1μm, but only reach 55% dissolved at <10 μm, and 16% at <100 μm (Rinder and von Hagke, 2021). The particle size that will facilitate optimal CO_2 sequestration has been suggested between 10–30 μm, but it is largely dependent on factors like the mineralogy of the feedstock, climactic conditions, mineral to water ratio, and biologic activity (Beerling et

al., 2018). However, environmental and financial costs increase with decreasing grain size, leading to a 30% reduction of CO_2 sequestration efficiency for feedstocks milled to 1μm (Hangx and Spiers, 2009). The proximity of the feedstock source to its dispersal site is also an important consideration, as transporting the feedstock is one of the highest costs of ERW along with processing (Schuiling and Krijgsman, 2006). The challenges of balancing the benefit of finer grain sizes with inefficiencies of further processing and transportation can be mitigated by using mine residues which are already being produced at the Gt scale, with grain sizes ranging from 10- 1000 μm (Bullock et al., 2021).

Although a feedstock's maximum capacity to sequester CO_2 sequestration is easily determined through geochemical analyses, rates of CO_2 sequestration will vary depending on the type of rock powder and dispersal site. These rates will largely depend on the properties of the rock powder (e.g., mineralogy and grain size), dosage per area (i.e., tonnes per square kilometre), and the environmental conditions of the dispersal site, including climate and soil properties (e.g., soil chemistry and microbial processes). Thus, determining reliable rates of CO_2 sequestration is important for developing enhancements to current methods and quantifying carbon offsets. CO_2 sequestration rates can be determined using field-deployable equipment, and potentially inferred from lab-based experiments. Laboratory studies combine experiments including leaches, reactors, and columns with analysis of stable carbon isotopes, geochemistry, quantitative mineralogy, and carbon coulometry to determine rates and capacities of CO_2 sequestration (Harrison et al., 2013; Paulo et al., 2021; Power et al., 2020; Rigopoulos et al., 2018). Stubbs et al. (2022) conducted a laboratory study to assess rates of CO_2 drawdown into ultramafic mine wastes and common ERW target minerals (wollastonite, olivine, brucite). The

authors used a dosage resulting in an 8.5 cm layer of each sample, and tested parameters including wetting/drying cycles, and surface tilling. This study determined that the mineralogical composition of the feedstocks has the greatest impact on its sequestration capacity, and that mineral water interactions can be optimized to target labile cations that promote CO_2 sequestration. Montserrat et al. (2017) used batch reactions of olivine in sea water to simulate ERW in coastal environments. This study found an increase of DIC that was attributed to the dissolution of the olivine, resulting in CO_2 sequestration.

1.3.1 Carbon verification

Field studies use similar analytical methods to assess rates on a larger scale and under more complex conditions, often employing long-term monitoring through changes in geochemistry (Haque et al., 2020), soil flux chambers (Chiodini et al., 1998), and quantitative mineralogy (Wilson et al., 2014). In Haque et al. (2020), a field study was conducted to assess CO_2 sequestration via annual wollastonite amendments to leafy vegetable fields over a 3-year period. The authors used initial dosages of 1.24 t/ha in the first year, followed by 2.5 t/ha in the following 2 years. The results of this field trial show an increase in soil inorganic carbon indicating sequestration of 2.4, 4.2, and 6.1 tonne CO_2/ha after 12, 24, and 36 months respectively. Amann et al. (2020) carried out experiments aimed at evaluating the efficiency of ERW through the application of olivine rich dunnite to agricultural soils in a rain barrel mesocosm study. This involved dosing each barrel of soil with 22 kg/m^2 of olivine rich dunnite and exposing it to a total of 800 mm of rainfall. Coupling Mg fluxes with DIC concentrations, the authors were able to extrapolate a CO_2 sequestration rate of 4.9 t CO_2/km^2/yr. Large scale ERW projects are

being conducted including OceanNETs (2021) aimed at increasing ocean alkalinization, Project Carbdown (2021) which incentivizes the spreading of ultramafic rock powder on agricultural lands, and Project Vesta (2021) with the goal of facilitating CO_2 sequestration through spreading olivine in coastal environments.

1.3.2 ERW applications and challenges

Several dispersal sites have been proposed for ERW. Many studies have investigated the possibility of using rock-based amendments on agricultural soils. Rocks and minerals that have been tested as soil amendments on arable land include wollastonite (Haque et al., 2019), basalt (Gillman et al., 2002; Nunes et al., 2014), olivine (ten Berge et al., 2012), and kimberlite (Miller and Naeth, 2017). The advantages of rock-based fertilizers include enhancing the concentrations of micro and macro nutrients (e.g. P, K, Ca, Mg, Zn, Mn) and pH adjustment similar to liming (Reid and Naeth, 2005; Theodoro and Leonardos, 2006). Rock-based fertilizers need to be selected to address specific needs of the soils including grain size, pH, organic matter, total nitrogen, macronutrient availability (e.g., P and K), micronutrient availability (e.g., Fe, Mn, Cu, Zn, B, Mo), and cation exchange capacity. Some mafic and ultramafic rocks (e.g. basalt, kimberlite) are suitable candidates as an amendment based on their high rates of cation release and often adequate concentrations of nutrients as well as their ultrabasic composition needed for pH adjustment (Beerling et al., 2018; Gillman et al., 2002). Agricultural soils that have been amended with Ca- or Mg-rich rocks have seen an increase in crop yield, as documented in small scales in the highly weathered tropical soils of Africa, Brazil, Malaysia, and Mauritius (Beerling et al., 2018). Cocoa plants amended with basalt in Brazil showed

higher concentrations of K (1.4 times control), Mg (10 times control), and P (1.7 times control), with treated plants growing 50% taller and 60% thicker than controls (Anda et al., 2013a). In Mauritius, basalt was used in conjunction with standard N-P-K fertilizers to increase crop yields by 17%–29% when compared to control samples using only fertilizer with no basalt, which indicates a favourable interaction between fertilizers and rock-based amendments (Edwards et al., 2017). Enhanced weathering of mafic and ultramafic rocks when used as soil amendments has also been documented to release silica into the soil as an available nutrient required for some crop growth, aiding in pest and disease resistance as well as water use efficiency (Hartmann et al., 2013). The application of crushed ultramafic rocks on highly weathered soils has the potential to improve the pH and mitigate soil acidification, which is an effect that mirrors conventional liming agents used in modern agriculture (ten Berge et al., 2012).

Other proposed dispersal sites for ERW also include coastal environments (Meysman and Montserrat, 2017; Montserrat et al., 2017) , which provide the co-benefit of mitigating ocean acidification (Hartmann et al., 2013). Terrestrial locations that exclude arid and polar regions have also garnered significant attention as locations for ERW deployment, with optimistic models indicating 14,700,00 km^2 of potential application sites, which largely consist of arable land (Moosdorf et al., 2014).

Understanding the composition of a feedstock is important for the prediction and monitoring of ERW effluent. In addition to releasing Ca and Mg that are needed for CO_2 mineralization and nutrients for plant growth, rock powders for ERW may also release elements of concern. Of the most concern is the potential to leach Ni and Cr, which are commonly found in feedstocks like olivine, basalt, and kimberlite, potentially leading to

adverse effects on plant and human health when found above acceptable levels. Toxicity mechanisms of Ni include 1) disruption of ion regulation (primarily Ca, Mg, and Fe), 2) respiratory epithelia, an allergic type reaction, and 3) oxidative stress (Flipkens et al., 2021). In aqueous systems, Cr is found in its bioavailable form of chromate (CrO_4^{2-}) or dichromate ($Cr_2O_4^{2-}$), which can reduce from Cr (IV) to Cr (III) causing damage to cell membranes, DNA, and proteins. Concentrations of Ni and Cr can vary greatly across rock types, and between the same rock type from different sources. Because of this, there is a need for individual assessment and judicious selection of ERW feedstocks. Ultramafic rocks that are rich in olivine (Peridotites: dunite, harzburgite, lherzolite, wehrlite) often contain elevated concentrations of Ni, and Cr (Beerling et al., 2018), where Ni is found to be released through weathering experiments in a bioavailable form at low pH (ten Berge et al., 2012). Ni and Cr that is released from olivine may not be of concern in the effluent, but rather as an accumulation in the soil profile (Renforth et al., 2015a), or in soil sediments of aquatic systems (Flipkens et al., 2021). Further research is needed to determine the potential for introduction of elements of concern to agricultural systems through ERW, and the effects this may have on the environment, food supply, and ultimately human health.

1.4 CO_2 sequestration via weathering of mine wastes

Certain mines are sources of ultramafic and mafic feedstocks due to high quantities of processed rock already being produced, offering an often-untapped potential to be used for long-term storage of CO_2. It is estimated that globally, nickel, platinum group metals, asbestos, diamonds, chromite, and talc mines process about 419 Mt of mafic and

ultramafic tailings annually (Power et al., 2014), making these mines a good target for feedstocks.

Passive CDR has been reported in mine wastes under ambient conditions but is typically limited to offsetting a very small portion of a mines carbon emissions. This has been documented in waste facilities of asbestos mines (Assima et al., 2014a; Hamilton et al., 2021), nickel mines (Wilson et al., 2014) and the kimberlite residues of diamond mines (Mervine et al., 2018; Wilson et al., 2011). Rates of passive CO_2 sequestration at these mines have been determined using combinations of field and laboratory techniques including mineralogy, C isotopes, total inorganic carbon measurements, and kinetic leach columns. Monitoring of passive CO_2 sequestration in mine wastes faces the challenges of representative sampling over millions of tons of tailings (Wilson et al., 2014), distinguishing between primary and secondary carbonates (Turvey et al., 2018), and difficulties tracking waters in an open system. Prominent studies in this field include work done by Lechat et al. (2016) which investigated passive carbonation at the closed Thetford Mine, determining a sequestration rate of 4 $kg/m^2/yr$, attributed to the low CO_2 concentrations (<50 ppm) and presence of hydromagnesite in experimental cells. A similar study was conducted at Dumont Nickel Project by Gras et al. (2017) who set up field cells which were observed to have low concentrations of CO_2 (~100 ppm) indicating its consumption by carbonate minerals (aragonite, nesquehonite, dypingite and hydromagnesite) which were not found in unweathered residues.

Diamond mines and their kimberlite residues have garnered significant attention as facilities to promote weathering and increase CO_2 sequestration. Mervine et al. (2018) estimates maximum CO_2 sequestration capacities based on geochemistry ranging from

0.5–1.51 Mt CO_2 for 5 diamond mines (Venetia, Voorspoed, Gahcho Kué, Victor, and Snap Lake). A further investigation into the CO_2 sequestration at the Venetia Diamond Mine has been conducted by Stubbs et al. (2022), which documented evidence of passive carbonation as minor cementations on the residues, likely driven by the overconcentration of ions as the process waters evaporates. A laboratory experiment conducted by the authors measured CO_2 drawdown into unweathered residues, measuring a peak influx of -870 g/CO_2/yr at 48% saturation. Further investigation of kimberlite residues for CDR is needed, as they hold the potential to provide many Mt of pre-milled, accessible feedstocks.

Like ERW studies, these rates of CO_2 sequestration in mine wastes are typically a function of the feedstocks composition and physical characteristics, climatic conditions that control temperature and available water. Other important considerations that are not applicable to ERW is the chemistry of reacting process waters, and the design of the tailings storage facility (Power et al., 2014). The only factors that can realistically be altered without massive changes to processing circuits to facilitate enhanced CO_2 sequestration in mine wastes is the storage conditions and the grainsize of the tailings. The identification of pathways to optimization by addressing rate limitations is important on a mine to mine basis, which needs to be addressed to facilitate large scale CO_2 sequestration at mine sites.

1.5 Drainage chemistry and the characterization of mine wastes

Drainage chemistry controls the suitability of a given mine waste to function as a feedstock for CO_2 sequestration. Considerations for this include concentrations of

carbonate forming cations (Ca, Mg) being released, alkalinity and dissolved inorganic carbon that represents solubility trapping of CO_2, and the release of potentially beneficial or deleterious elements. Mines have the capability to monitor effluent in the context of contamination, but in the scope of CO_2 sequestration, the prediction and monitoring of drainage water chemistry has not been adopted. Mine drainage chemistry is hydro-geologically complex and is difficult to accurately predict due to variations in mineralogy, climate, tailings storage conditions, microbial processes, and hydrologic factors (Jamieson et al., 2015). Geochemical modelling using parameters measured at mines can simulate processes and predict mine water chemistry but is not a substitute for long-term monitoring. Five factors that govern drainage chemistry and can be used to predict effluent quality are 1) production rates of metals, non-metals, acidity, and alkalinity, 2) the volume and rate of flow through the rock pile, 3) the time between infiltration events, 4) the residence time of water within the feedstock, and 5) the percentage of rock flushed by water (Morin and Hutt, 1994). Mineralogical and geochemical characterization of any rock or mineral that water may interact with at a mine is important for understanding environmental and human health risks including acid generation, increased contaminant concentrations, and inhalation, or ingestion of contaminants by humans (Helser and Cappuyns, 2021). Understanding mineral-water interactions within mine wastes is fundamental for assessing and eventually controlling the risks of mine water drainage and has applications in the field of ERW and CO_2 sequestration.

There are many tools for assessing mine water effluent in the context of acid generation, or deleterious metal release, but in the scope of ERW and CO_2 mineralization,

progress needs to be made. Kinetic tests are a common method used in ERW studies and operate similarly to what is done for assessing mine effluent. Columns and leaches are commonly used as a tool for assessing ERW. Studies like Power et al. (2020) have used flow through experiments and columns to assess reactivity of feedstocks, and direct air capture of CO_2. Kandji et al. (2017) conducted column experiments using residues from the Dumont Nickel Project to evaluate the carbonation potential. Outdoor experiments like that of Hamilton et al. (2021) have taken a similar approach to leaching columns but applied them to a larger area in the form of test plots. Renforth (2015) coupled the control of a laboratory leaching column with the complexity of an outdoor experiment by applying olivine to an intact soil core extracted from an agricultural field. An aspect missing from most ERW studies is the monitoring of their effectiveness by tracking carbon. Monitoring of feedstocks weathering for CO_2 sequestration is important for several reasons, ranging from accurate reporting to financial incentives, to human health impacts. Progress towards widespread adoption of ERW requires technology and protocols to be developed for predicting and monitoring CO_2 sequestration, and drainage chemistry.

Analytical methods for characterizing mine wastes include X-ray fluorescence (XRF) for elemental analysis, X-ray diffraction (XRD) for mineralogical analysis, scanning electron microscopy (SEM), and destructive methods including inductively coupled plasma-atomic emission spectroscopy (ICP-AES) or inductively coupled plasma-mass spectroscopy (ICP-MS; Jamieson et al., 2015). A thorough understanding of the mineralogy and geochemistry of a mine's wastes can play a large role in other parameter tests including acid base accounting (ABA) to determine potential for acid generation, or

kinetic tests including columns and humidity cells for analyzing solutes (Jamieson, 2011). Concerns about kinetic tests center on the easily extractable elements of interest and the uncertainty about their mineral association, which can lead to issues when extrapolating these results to a larger scale (Jaimeson et al., 2015). While some standard mine waste characterization methodologies are applicable to CO_2 sequestration, expansions to include tailor-made approaches for predicting and assessing CO_2 sequestration rates is critical for the success of this NET.

1.6 Research objectives

Alkaline mineral feedstocks, including mine wastes, have considerable potential for ERW and CO_2 mineralization as a means of removing CO_2 from the atmosphere. The two main goals of this research are to develop a rapid test for assessing feedstock reactivity and release of elements of interest (e.g., divalent cations, nutrients, and metals) and to develop a field-deployable column for determining the rates of CO_2 sequestration for long-term monitoring of ERW rates.

Chapter 2 aimed to assess the reactivity of each feedstock through batch leaches intended to facilitate the release of easily extractable elements. Through this process, we were able to quantify the release of divalent metal cations (Ca^{2+}, Mg^{2+}) from non-carbonate sources, used to calculate the feedstock's potential for CO_2 sequestration. The secondary goal of this experiment was to quantify the release of nutrients (e.g., P, K) and potentially deleterious metals and metalloids (e.g., Ni, Cr) to assess the ability of these feedstocks to be used in an agricultural setting. The goal is that this experimental protocol can be used as a predictive tool for evaluating the reactivity of feedstocks for ERW.

The study described in Chapter 3 employs long-term leaching columns using four of the same feedstocks from Chapter 2 to determine their rate of CO_2 sequestration. The objectives were to: (1) develop field-deployable leaching columns for monitoring ERW and drainage chemistry in future pilot studies and (2) accurately track carbon as a solid, dissolved, and gas phase as it moves through the column, ultimately creating a carbon-mass balance.

1.6 References

IPCC: Amann, T., Hartmann, J., Struyf, E., De Oliveira Garcia, W., Fischer, E.K., Janssens, I., Meire, P., Schoelynck, J., 2020. Enhanced Weathering and related element fluxes - A cropland mesocosm approach. Biogeosciences 17, 103–119. https://doi.org/10.5194/bg-17-103-2020

Anda, M., Shamshuddin, J., Fauziah, C.I., 2013. Increasing negative charge and nutrient contents of a highly weathered soil using basalt and rice husk to promote cocoa growth under field conditions. Soil Tillage Res. 132, 1–11. https://doi.org/10.1016/j.still.2013.04.005

Assima, G.P., Larachi, F., Molson, J., Beaudoin, G., 2014. Comparative study of five Québec ultramafic mining residues for use in direct ambient carbon dioxide mineral sequestration. Chem. Eng. J. https://doi.org/10.1016/j.cej.2014.02.010

Beerling, D.J., Leake, J.R., Long, S.P., Scholes, J.D., Ton, J., Nelson, P.N., Bird, M., Kantzas, E., Taylor, L.L., Sarkar, B., Kelland, M., DeLucia, E., Kantola, I., Müller, C., Rau, G., Hansen, J., 2018. Farming with crops and rocks to address global climate, food and soil security /631/449 /706/1143 /704/47 /704/106 perspective. Nat. Plants 4, 138–147. https://doi.org/10.1038/s41477-018-0108-y

Berner, R.A., 2003. The long-term carbon cycle, fossil fuels and atmospheric composition. Nature. https://doi.org/10.1038/nature02131

Beuttler, C., Charles, L., Wurzbacher, J., 2019. The Role of Direct Air Capture in Mitigation of Anthropogenic Greenhouse Gas Emissions. Front. Clim. 1, 1–7. https://doi.org/10.3389/fclim.2019.00010

Brantley, S.L., 2008. Kinetics of mineral dissolution, in: Kinetics of Water-Rock

Interaction. https://doi.org/10.1007/978-0-387-73563-4_5

Broecker, W.S., 2007. CO_2 Arithmetic. Science 315, 1371.

Bullock, L.A., James, R.H., Matter, J., Renforth, P., Teagle, D.A.H., Bullock, L.A., 2021. Global Carbon Dioxide Removal Potential of Waste Materials From Metal and Diamond Mining 3, 1–12. https://doi.org/10.3389/fclim.2021.694175

Chiodini, G., Cioni, R., Guidi, M., Raco, B., Marini, L., 1998. Soil CO2 flux measurements in volcanic and geothermal areas. Appl. Geochemistry 13, 543–552. https://doi.org/10.1016/S0883-2927(97)00076-0

Daval, D., Hellmann, R., Martinez, I., Gangloff, S., Guyot, F., 2013. Lizardite serpentine dissolution kinetics as a function of pH and temperature, including effects of elevated pCO_2. Chem. Geol. https://doi.org/10.1016/j.chemgeo.2013.05.020

Di Lorenzo, F., Ruiz-Agudo, C., Ibañez-Velasco, A., Gil-San Millán, R., Navarro, J.A.R., Ruiz-Agudo, E., Rodriguez-Navarro, C., 2018. The carbonation of wollastonite: A model reaction to test natural and biomimetic catalysts for enhanced CO_2 sequestration. Minerals. https://doi.org/10.3390/min8050209

Edwards, D.P., Lim, F., James, R.H., Pearce, C.R., Scholes, J., Freckleton, R.P., Beerling, D.J., 2017. Climate change mitigation: Potential benefits and pitfalls of enhanced rock weathering in tropical agriculture. Biol. Lett. 13. https://doi.org/10.1098/rsbl.2016.0715

Flipkens, G., Blust, R., Town, R.M., 2021. Deriving Nickel (Ni(II)) and Chromium (Cr(III)) Based Environmentally Safe Olivine Guidelines for Coastal Enhanced Silicate Weathering. Environ. Sci. Technol. 55, 12362–12371. https://doi.org/10.1021/acs.est.1c02974

Forsberg, L.S., Ledin, S., 2006. Effects of sewage sludge on pH and plant availability of metals in oxidising sulphide mine tailings. Sci. Total Environ. 358, 21–35. https://doi.org/10.1016/j.scitotenv.2005.05.038

Gillman, G.P., Burkett, D.C., Coventry, R.J., 2002. Amending highly weathered soils with finely ground basalt rock. Appl. Geochemistry 17, 987–1001. https://doi.org/https://doi.org/10.1016/S0883-2927(02)00078-1

Gislason, S.R., Wolff-Boenisch, D., Stefansson, A., Oelkers, E.H., Gunnlaugsson, E., Sigurdardottir, H., Sigfusson, B., Broecker, W.S., Matter, J.M., Stute, M., Axelsson, G., Fridriksson, T., 2010. Mineral sequestration of carbon dioxide in basalt: A pre-injection overview of the CarbFix project. Int. J. Greenh. Gas Control 4, 537–545. https://doi.org/10.1016/j.ijggc.2009.11.013

Gras, A., Beaudoin, G., Molson, J., Plante, B., Bussière, B., Lemieux, J.M., Dupont, P.P., 2017. Isotopic evidence of passive mineral carbonation in mine wastes from the Dumont Nickel Project (Abitibi, Quebec). Int. J. Greenh. Gas Control 60, 10–23. https://doi.org/10.1016/j.ijggc.2017.03.002

Hamilton, J.L., Wilson, S.A., Turvey, C.C., Morgan, B., Tait, A.W., McCutcheon, J., Fallon, S.J., Southam, G., 2021. Carbon accounting of mined landscapes, and deployment of a geochemical treatment system for enhanced weathering at Woodsreef Chrysotile Mine, NSW, Australia. J. Geochemical Explor. 220. https://doi.org/10.1016/j.gexplo.2020.106655

Hangx, S.J.T., Spiers, C.J., 2009. Coastal spreading of olivine to control atmospheric CO_2 concentrations: A critical analysis of viability. Int. J. Greenh. Gas Control 3, 757–767. https://doi.org/10.1016/j.ijggc.2009.07.001

Haque, F., Santos, R.M., Chiang, Y.W., 2020a. CO_2 sequestration by wollastonite-amended agricultural soils – An Ontario field study. Int. J. Greenh. Gas Control. https://doi.org/10.1016/j.ijggc.2020.103017

Haque, F., Santos, R.M., Chiang, Y.W., 2020b. CO_2 sequestration by wollastonite-amended agricultural soils – An Ontario field study. Int. J. Greenh. Gas Control 97, 103017. https://doi.org/10.1016/j.ijggc.2020.103017

Haque, F., Santos, R.M., Dutta, A., Thimmanagari, M., Chiang, Y.W., 2019. Co-Benefits of Wollastonite Weathering in Agriculture: CO_2 Sequestration and Promoted Plant Growth. ACS Omega 4, 1425–1433. https://doi.org/10.1021/acsomega.8b02477

Harrison, A.L., Power, I.M., Dipple, G.M., 2013. Accelerated carbonation of brucite in mine tailings for carbon sequestration. Environ. Sci. Technol. https://doi.org/10.1021/es3012854

Hartmann, J., West, A.J., Renforth, P., Köhler, P., De La Rocha, C.L., Wolf-Gladrow, D.A., Dürr, H.H., Scheffran, J., 2013. Enhanced chemical weathering as a geoengineering strategy to reduce atmospheric carbon dioxide, supply nutrients, and mitigate ocean acidification. Rev. Geophys. https://doi.org/10.1002/rog.20004

Helser, J., Cappuyns, V., 2021. Trace elements leaching from Pb[sbnd]Zn mine waste (Plombières, Belgium) and environmental implications. J. Geochemical Explor. 220, 106659. https://doi.org/10.1016/j.gexplo.2020.106659

Jamieson, H.E., 2011. Geochemistry and mineralogy of solid mine waste: Essential knowledge for predicting environmental impact. Elements 7, 381–386. https://doi.org/10.2113/gselements.7.6.381

Jamieson, H.E., Walker, S.R., Parsons, M.B., 2015. Mineralogical characterization of

mine waste. Appl. Geochemistry 57, 85–105. https://doi.org/10.1016/j.apgeochem.2014.12.014

Krüger, L., 2007. Technical Note TN 2007-07-01 KIMBERLITE AS LOW GRADE FERTILIZER - A REVIEW 1–20.

Lefebvre, D., Goglio, P., Williams, A., Manning, D.A.C., de Azevedo, A.C., Bergmann, M., Meersmans, J., Smith, P., 2019. Assessing the potential of soil carbonation and enhanced weathering through Life Cycle Assessment: A case study for Sao Paulo State, Brazil. J. Clean. Prod. 233, 468–481. https://doi.org/10.1016/j.jclepro.2019.06.099

Mervine, E.M., Wilson, S.A., Power, I.M., Dipple, G.M., Turvey, C.C., Hamilton, J.L., Vanderzee, S., Raudsepp, M., Southam, C., Matter, J.M., Kelemen, P.B., Stiefenhofer, J., Miya, Z., Southam, G., 2018. Potential for offsetting diamond mine carbon emissions through mineral carbonation of processed kimberlite: an assessment of De Beers mine sites in South Africa and Canada. Mineral. Petrol. 112, 755–765. https://doi.org/10.1007/s00710-018-0589-4

Meysman, F.J.R., Montserrat, F., 2017. Negative CO_2 emissions via enhanced silicate weathering in coastal environments. Biol. Lett. 13. https://doi.org/10.1098/rsbl.2016.0905

Miller, V.S., Naeth, M.A., 2017. Amendments and substrates to develop anthroposols for northern mine reclamation. Can. J. Soil Sci. 97, 266–277. https://doi.org/10.1139/cjss-2016-0145

Minx, J.C., Lamb, W.F., Callaghan, M.W., Bornmann, L., Fuss, S., 2017. Fast growing research on negative emissions. Environ. Res. Lett. 12.

https://doi.org/10.1088/1748-9326/aa5ee5

Montserrat, F., Renforth, P., Hartmann, J., Leermakers, M., Knops, P., Meysman, F.J.R., 2017. Olivine Dissolution in Seawater: Implications for CO_2 Sequestration through Enhanced Weathering in Coastal Environments. Environ. Sci. Technol. 51, 3960–3972. https://doi.org/10.1021/acs.est.6b05942

Moosdorf, N., Renforth, P., Hartmann, J., 2014. Carbon dioxide efficiency of terrestrial enhanced weathering. Environ. Sci. Technol. 48, 4809–4816. https://doi.org/10.1021/es4052022

Morin, K.A., Hutt, N.M., 1994. An Empirical Technique for Predicting the Chemistry of Water Seeping from Mine-Rock Piles. J. Am. Soc. Min. Reclam. https://doi.org/10.21000/jasmr94010012

Morse, J.W., Arvidson, R.S., Lüttge, A., 2007. Calcium carbonate formation and dissolution. Chem. Rev. https://doi.org/10.1021/cr050358j

Nunes, J.M.G., Kautzmann, R.M., Oliveira, C., 2014. Evaluation of the natural fertilizing potential of basalt dust wastes from the mining district of Nova Prata (Brazil). J. Clean. Prod. https://doi.org/10.1016/j.jclepro.2014.04.032

Oelkers, E.H., Gislason, S.R., Matter, J., 2008. Mineral carbonation of CO_2. Elements. https://doi.org/10.2113/gselements.4.5.333

Paulo, C., Power, I.M., Stubbs, A.R., Wang, B., Zeyen, N., Wilson, S.A., 2021. Evaluating feedstocks for carbon dioxide removal by enhanced rock weathering and CO_2 mineralization. Appl. Geochemistry 129, 104955. https://doi.org/10.1016/j.apgeochem.2021.104955

Pokrovsky, O.S., Schott, J., 2004. Experimental study of brucite dissolution and

precipitation in aqueous solutions: Surface speciation and chemical affinity control. Geochim. Cosmochim. Acta 68, 31–45. https://doi.org/10.1016/S0016-7037(03)00238-2

Power, I.M., Dipple, G.M., Bradshaw, P.M.D., Harrison, A.L., 2020. Prospects for CO_2 mineralization and enhanced weathering of ultramafic mine tailings from the Baptiste nickel deposit in British Columbia, Canada. Int. J. Greenh. Gas Control 94, 102895. https://doi.org/10.1016/j.ijggc.2019.102895

Power, I.M., Dipple, G.M., Southam, G., 2010. Bioleaching of ultramafic tailings by Acidithiobacillus spp. for CO_2 sequestration. Environ. Sci. Technol. https://doi.org/10.1021/es900986n

Power, I.M., Harrison, A.L., Dipple, G.M., Wilson, S.A., Kelemen, P.B., Hitch, M., Southam, G., 2013. Carbon mineralization: From natural analogues to engineered systems. Rev. Mineral. Geochemistry 77, 305–360. https://doi.org/10.2138/rmg.2013.77.9

Power, I.M., Kenward, P.A., Dipple, G.M., Raudsepp, M., 2017. Room Temperature Magnesite Precipitation. Cryst. Growth Des. https://doi.org/10.1021/acs.cgd.7b00311

Power, I.M., McCutcheon, J., Harrison, A.L., Wilson, S.A., Dipple, G.M., Kelly, S., Southam, C., Southam, G., 2014. Strategizing carbon-neutral mines: A case for pilot projects, Minerals. https://doi.org/10.3390/min4020399

Reid, N.B., Naeth, M.A., 2005. Establishment of a vegetation cover on tundra kimberlite mine tailings: 1. A greenhouse study. Restor. Ecol. 13, 594–601. https://doi.org/10.1111/j.1526-100X.2005.00076.x

Renforth, P., Pogge von Strandmann, P.A.E., Henderson, G.M., 2015. The dissolution of olivine added to soil: Implications for enhanced weathering. Appl. Geochemistry. https://doi.org/10.1016/j.apgeochem.2015.05.016

Rigopoulos, I., Harrison, A.L., Delimitis, A., Ioannou, I., Efstathiou, A.M., Kyratsi, T., Oelkers, E.H., 2018. Carbon sequestration via enhanced weathering of peridotites and basalts in seawater. Appl. Geochemistry 91, 197–207. https://doi.org/10.1016/j.apgeochem.2017.11.001

Rinder, T., von Hagke, C., 2021. The influence of particle size on the potential of enhanced basalt weathering for carbon dioxide removal - Insights from a regional assessment. J. Clean. Prod. 315. https://doi.org/10.1016/j.jclepro.2021.128178

Sanderson, B.M., O'Neill, B.C., Tebaldi, C., 2016. What would it take to achieve the Paris temperature targets? Geophys. Res. Lett. 43, 7133–7142. https://doi.org/10.1002/2016GL069563

Schott, J., Pokrovsky, O.S., Oelkers, E.H., 2009. The link between mineral dissolution/precipitation kinetics and solution chemistry. Rev. Mineral. Geochemistry 70, 207–258. https://doi.org/10.2138/rmg.2009.70.6

Schuiling, R.D., Krijgsman, P., 2006. Enhanced weathering: An effective and cheap tool to sequester CO_2. Clim. Change. https://doi.org/10.1007/s10584-005-3485-y

Strefler, J., Amann, T., Bauer, N., Kriegler, E., Hartmann, J., 2018. Potential and costs of carbon dioxide removal by enhanced weathering of rocks. Environ. Res. Lett. 13. https://doi.org/10.1088/1748-9326/aaa9c4

Stubbs, A.R., Paulo, C., Power, I.M., Wang, B., Zeyen, N., Wilson, S.A., 2022. Direct measurement of CO_2 drawdown in mine wastes and rock powders: Implications for

enhanced rock weathering. Int. J. Greenh. Gas Control 113. https://doi.org/10.1016/j.ijggc.2021.103554

Teir, S., Revitzer, H., Eloneva, S., Fogelholm, C.J., Zevenhoven, R., 2007. Dissolution of natural serpentinite in mineral and organic acids. Int. J. Miner. Process. https://doi.org/10.1016/j.minpro.2007.04.001

ten Berge, H.F.M., van der Meer, H.G., Steenhuizen, J.W., Goedhart, P.W., Knops, P., Verhagen, J., 2012. Olivine weathering in soil, and its effects on growth and nutrient uptake in ryegrass (Lolium perenne L.): A pot experiment. PLoS One. https://doi.org/10.1371/journal.pone.0042098

Theodoro, S.H., Leonardos, O.H., 2006. The use of rocks to improve family agriculture in Brazil. An. Acad. Bras. Cienc. https://doi.org/10.1590/s0001-37652006000400008

Turvey, C.C., Wilson, S.A., Hamilton, J.L., Tait, A.W., McCutcheon, J., Beinlich, A., Fallon, S.J., Dipple, G.M., Southam, G., 2018. Hydrotalcites and hydrated Mg-carbonates as carbon sinks in serpentinite mineral wastes from the Woodsreef chrysotile mine, New South Wales, Australia: Controls on carbonate mineralogy and efficiency of CO_2 air capture in mine tailings. Int. J. Greenh. Gas Control 79, 38–60. https://doi.org/10.1016/j.ijggc.2018.09.015

Wilson, S.A., Barker, S.L.L., Dipple, G.M., Atudorei, V., 2010. Isotopic disequilibrium during uptake of atmospheric CO_2 into mine process waters: Implications for CO_2 sequestration. Environ. Sci. Technol. https://doi.org/10.1021/es1021125

Wilson, S.A., Dipple, G.M., Power, I.M., Barker, S.L.L., Fallon, S.J., Southam, G., 2011. Subarctic weathering of mineral wastes provides a sink for atmospheric CO_2.

Environ. Sci. Technol. https://doi.org/10.1021/es202112y

Wilson, S.A., Harrison, A.L., Dipple, G.M., Power, I.M., Barker, S.L.L., Ulrich Mayer, K., Fallon, S.J., Raudsepp, M., Southam, G., 2014. Offsetting of CO_2 emissions by air capture in mine tailings at the Mount Keith Nickel Mine, Western Australia: Rates, controls and prospects for carbon neutral mining. Int. J. Greenh. Gas Control 25, 121–140. https://doi.org/10.1016/j.ijggc.2014.04.002

Chapter 2
CO_2 batch leaches for evaluating reactivity and element release from enhanced rock weathering feedstocks

2.1 Introduction

Increasing anthropogenic CO_2 concentrations in the atmosphere has necessitated the development of large-scale carbon dioxide removal (CDR) to mitigate the effects of climate change (IPCC, 2018; Beuttler et al., 2019). All emissions pathways presented by the IPCC (2018) require the use of CDR to remain within 1.5 °C of Earth's preindustrial temperatures, a critical target in the Paris Agreement. Rapid adoption of negative emissions technologies (NETs) for CDR is required to achieve this, (IPCC 2018, 2019; Sanderson et al., 2016) despite current knowledge being considered incomplete, albeit rapidly expanding (Minx et al., 2018). Enhanced rock weathering (ERW) and CO_2 mineralization are prospective NETs that use silicate and hydroxide minerals to sequester CO_2 (Meysman and Montserrat, 2017; Power et al., 2013; Renforth, 2012). The passive weathering of silicate minerals is a massive sink of atmospheric CO_2 and plays a crucial role in Earth's carbon cycle, currently removing ~1.1 Gt/yr. (Amann et al., 2020; Strefler et al., 2018a), with the potential for significant improvement through ERW.

ERW consists of three key stages, 1) the acceleration of alkaline mineral dissolution rates, 2) the release of divalent metal cations (Ca^{2+}, Mg^{2+}), and 3) the storage of CO_2 as a soluble phase (e.g. HCO_3^-), or potential precipitation as a carbonate (e.g. $CaCO_3$, $MgCO_3$), resulting in long term storage of CO_2 (Assima et al., 2014b; Lefebvre et al., 2019; Power et al., 2013; Veetil and Hitch, 2020). Mineral dissolution and cation release are the driving processes behind ERW but are often considered rate-limiting. Recent studies have demonstrated that ERW within alkaline feedstocks may be

accelerated through the use of physical, chemical, and microbial treatments that accelerate cation release (Haque et al., 2020c; Oelkers et al., 2018; Power et al., 2014, 2010; Veetil and Hitch, 2020). The extent to which ERW can be used to sequester CO_2 is largely dependent on the physical and chemical properties (e.g., mineralogy, specific surface area) of the feedstock (Power et al., 2013; Schott et al., 2009; Zhao et al., 2010). Ideal feedstocks for ERW are rich in divalent cations (chiefly, Ca^{2+} and Mg^{2+}), available in large quantities, boast high rates of reactivity and dissolution, and include olivine (Renforth et al., 2015a; ten Berge et al., 2012), wollastonite (Di Lorenzo et al., 2018; Haque et al., 2020b, 2019), brucite (Harrison et al., 2013), serpentine minerals (Daval et al., 2013; Power et al., 2020), basalt (Lefebvre et al., 2019; Oelkers et al., 2008), and kimberlite in the form of mine residues (Mervine et al., 2018; Paulo et al., 2021; Wilson et al., 2011).

Elements of interest (EOI) that may be released into solution through mineral weathering can include deleterious metals and metalloids, and conversely, nutrients that may be beneficial for plant growth. Studies that investigate the release of EOIs from ERW feedstocks have focused on predicting and monitoring Ni and Cr as a detriment in the leachate, and P, K, and Si as a benefit (Beerling et al., 2018; Haque, et al., 2020; Montserrat et al., 2017; ten Berge et al., 2012). ERW feedstocks have the potential to release Ni and Cr at concentrations that may have adverse effects on soils, natural waters, and human health (Mehta et al., 2019; Renforth et al., 2015a). As such, feedstocks must be carefully selected and evaluated for the potential release of these elements.

Feedstock evaluation for ERW and CO_2 mineralization has typically consisted of laboratory experiments including flow-through columns, kinetic leach tests, CO_2 fluxes,

and more theoretical approaches like mineralogical and geochemical assessment (Harrison et al., 2015; Power et al., 2020; Turvey et al., 2018; Wilson et al., 2014). Given that the ability for a feedstock to sequester CO_2 is largely governed by its compositions, the amount of Ca and Mg (often represented as CaO and MgO) can be used to calculate a total capacity for CDR. A theoretical approach assuming complete conversion of all CaO and MgO to a carbonate sink at a 1:1 molar ratio, or a feedstocks total CDR capacity (R_{CO_2} measured in kg of CO_2 per tonne of material) is defined in Equation 2.1:

$$R_{CO_2} = \frac{M_{CO_2}}{100}\left[\left(\frac{\%CaO}{M_{CaO}} + \frac{\%MgO}{M_{MgO}}\right) - molC_{TIC}\right] \times 1000 \quad (2.1)$$

where M_{CaO}, M_{MgO}, and M_{CO2} represent the molar masses of CaO, MgO, and CO_2 respectively, and $molC_{TIC}$ represents the mols of total inorganic carbon (TIC) present in the sample. This equation (Eq.1) considers the whole rock geochemistry under the assumption that 100% of all Ca and Mg from non-carbonate sources will become available. What this equation fails to account for is the reactivity and dissolution rate of the feedstock, which governs the timeline that the sequestration capacity is met. Cation release as a determinant of ERW suitability, has been extensively studied during laboratory experiments using leaching tests as a predictive tool, and is also applicable for assessing reactivity, acid-generating potential, or effluent quality (Hesler and Cappuyns, 2020; Jamieson, 2011; Paulo et al., 2021). Until recently there has been the need for a simplified protocol for feedstock assessment that is easily accessible yet accurate. A robust, comprehensive, and simple approach for measuring easily extractable cations from non-carbonate sources has been developed by Paulo et al. (2021) to evaluate the suitability of several feedstocks for large scale CO_2 sequestration. However, there has been a lack of research investigating the release of EOI's in ERW experiments, and its

implications for environmental health. In this chapter, the methods of Paulo et al. (2021) have been modified to also assess the quality of drainage, including beneficial nutrients and harmful metals and metalloids, a critical consideration of a feedstocks suitability which is often overlooked.

This study investigates the CO_2 sequestration potential and capacities of rock and mineral feedstocks through enhanced weathering. Feedstocks evaluated in this study include kimberlite residues from the Gahcho Kué, Venetia, and Voorspoed Diamond Mines, as well as wollastonite skarn, olivine sand, metabasalt soil amendment, and tailings from the Mount Keith Nickel Mine. Evaluations of these feedstocks included: 1) predicting the labile cation release from non-carbonate sources and 2) predicting the release of EOI, including potential nutrients and deleterious cations. To accomplish these evaluations the feedstocks physical, chemical, and mineralogical characterization were coupled with the results of batch leaching tests. The results of this study will contribute to the understanding of each feedstock and its potential to be used in large-scale CDR projects while further developing the use of CO_2 batch leaches to assess reactivity and elemental release.

2.2 Materials and methods

2.2.1 Sample acquisition and preparation

Mineral samples comprised of wollastonite skarn, forsterite, and quartz were used in this chapter. Wollastonite skarn samples were provided as soil amendment packages from the Canadian Wollastonite quarry near Kingston, Ontario, Canada. Forsterite and quartz sand was purchased from Bell & MacKenzie, Ontario, Canada. A metabasalt sample used as a soil amendment has been provided by V6 Agronomy, Rouleau, Saskatchewan, Canada. Kimberlite samples were provided by the Gahcho Kué Diamond Mine, Northwest Territories, Canada, The Diavik Diamond Mine, Northwest Territories, Canada, The Venetia Diamond Mine, Limpopo Province, South Africa, and Voorspoed Diamond Mine, Kroonstad, Free State, South Africa. Mine tailings were provided by the Mount Keith Nickel Mine, Western Australia.

Table 2.1. Sample inventory of feedstocks analyzed in this Chapter, including their background and physical characteristics. Materials also used in Chapter 3 of this thesis are noted.

Sample name	Sample ID	Rock type	Locality	Used in Ch.3	D50 particle size (μm)	BET (m^2/g)
Gahcho Kué fine residues	GK	Kimberlite	Canada	Yes	70.6	20.6
Venetia fine residues	DVK	Kimberlite	South Africa	Yes	249.1	13.6
Voorspoed fine residues	VSD T3	Kimberlite	South Africa		86.9	6.5
Voorspoed fine residues	VSD T5	Kimberlite	South Africa		181.1	7.9
Diavik fine residues	DIV	Kimberlite	Canada		37.6	47.9
Wollastonite	WOL	Wollastonite Skarn	Canada	Yes	242.2	0.8
Olivine	OLI	Forsterite sand	N/A	Yes	423.2	0.2
Quartz sand	QTZ	Quartz sand	N/A	Yes	259.9	0.1
Mount Keith tailings	MKM	Serpentine tailings	Australia		50.9	9.4
Metabasalt soil amendment	MBA	Metabasalt	Canada		11.7	1.73

2.2.2 Particle size and surface area

Solid samples were analyzed using a Horiba LA-950V2 laser scattering particle size distribution analyzer (Teledyne: USA) at Trent University. Sodium hexametaphosphate (30 g/L) was used as a dispersant agent to prevent flocculation of

samples, which were added to this solution, sonicated for 1 min, and then analyzed. This procedure was repeated three times to ensure samples were dis-agglomerated. This method is accurate within ±0.6% and has a reproducibility of ±0.1% or less.

A nitrogen gas (N_2) adsorption method was used to determine the Brunauer–Emmett–Teller (BET) specific surface areas at Trent University. First, samples were degassed overnight using a Smart VacPrepTM 067 (Micromeritics, Norcross, GA, USA), with samples kept at a temperature of 200 ºC for 10 h. Analysis was performed at 77 K (-196 ºC) on the Micromeritics TriStar II Plus adsorption unit (Micromeritics, Norcross, GA, USA) and N_2 isotherms were acquired using a p/p0 range of 0.01–0.90. All data processing was conducted on MicroActive Interactive software (Micromeritics, Norcross, GA, USA).

2.2.3 Mineralogical analysis

For all mineralogical and geochemical analyses, dried aliquots of each sample were micronized for 7 min in anhydrous ethanol using a McCrone Micronizing Mill, then dried in a fume hood before being disaggregated with an agate mortar and pestle. Cations within the interlayer spacings of the clay minerals in the kimberlite residues were exchanged with calcium prior to XRD analysis. Samples were added to a solution (150 mL) of 1.0 M $CaCl_2 \cdot 2H_2O$ in 250 mL Schott bottles and agitated on a shaker table overnight. Suspended solids were vacuum filtered using Millipore Isopore™ membrane filters (0.4 μm) and PALL 47 mm magnetic filter funnels. Samples on filters were rinsed with deionized water (18.2 MΩ·cm) and anhydrous ethanol before being removed from the filter paper, dried, and disaggregated.

XRD patterns were collected at the University of Alberta using a Rigaku Ultima IV IV θ–θ powder X-ray diffractometer equipped with aD/Tex Ultra detector. Data was collected using a long, fine-focus Co X-ray tube that was operated at 38 kV and 38 mA. All patterns were collected over a 2θ range of 5–80° with a step size of 0.02°/step at a rate of 1.2°2θ/minute. Mineral phase identification was conducted using the DIFFRAC.EVA XRD phase analysis software (Bruker) with reference to the International Center for Diffraction Data Powder Diffraction File 4+ database (ICDD PDF4+).

X-ray diffraction patterns for each feedstock were obtained from micronized samples under the same humidity conditions (20–30%) using a Bruker D8 Advance θ–θ powder X-ray diffractometer equipped with a LYNXEYE XE 1D Position Sensitive Detector in the Environmental Economic Geology Laboratory, University of Alberta.

2.2.4 Geochemical analysis

The bulk geochemical composition of mineral specimens was analyzed using X-ray fluorescence (XRF) spectroscopy with detection limits of 0.01% for all oxides. The trace element composition was determined through 4-acid digestion (HCl, HNO_3, HF, $HClO_4$), with detection limits of 1 ppm for Ni and Cr, and 0.5, 2, 3, 100, ppm for Cu, Pb, As, and Fe, respectively. Both analyses were conducted by SGS Minerals, Burnaby, British Columbia, Canada.

Total inorganic carbon (TIC) was determined using a Model CM5017 Coulometer from UIC Inc. at Trent University. Calibration of the instrument was conducted daily using blanks and $CaCO_3$ standards (Alfa Aesar; 99.95–100.05% purity). Detection limits

of this instrument are between 0.0001-100% C with a precision of 0.01 μg C. Samples were micronized using the previously mentioned method to ensure complete reaction of carbonates and reduce analysis time. Samples (250 mg) were digested in 2N H_2SO_4 (10 mL), mixed with an 8 mm stir bar at 50 °C, with a carrier gas rate of 100 mL/min through the acidification module. The pre-scrubber removed any CO_2 present in the carrier gas using potassium hydroxide (45%), while the post scrubber removed H_2S, SO_x, and/or halogens using silver nitrate (3 v/v%). The colorimetric cell contained monoethanolamine mixed with a colour indicator and two electrodes (platinum and silver), creating a titratable acid, changing the colour of the solution (and its % transmittance), proportional to the concentration of inorganic carbon injected into the cell.

2.2.5 CO_2 batch leaches

Batch leaches were conducted in 125 mL polycarbonate flasks with a stir bar and 100 mL of deionized water (18.2 MΩ·cm). Each flask was weighed before and after the addition of water and sample material, then placed on a multipoint magnetic stir plate set at 525 rpm (Cimarec™, Telesystem, Thermo Scientific). Dry CO_2 gas was bubbled through the deionized water using Tygon® tubing and a FM-1050 (E606) flow meter (Matheson, USA) connected to a CO_2 tank (>99%; 10 psi gauge pressure). The flow rate was set to constant rate of 0.35 Standard Liters Per Minute (SLPM). After 1 h, waters had reached equilibrium with CO_2 as indicated by pH of 3.9, confirmed by PHREEQC (Parkhurst and Appelo, 1999). Mineral samples (0.25 ± 0.01 g) were then added to the flasks without the interruption of CO_2 bubbling. CO_2 was bubbled uninterrupted for 48 h.

All leaches were run in triplicate at ambient laboratory temperature (~23 °C) with a flask of deionized water alone used as a blank.

After 48 h, the CO_2 supply was stopped, and the weight of the flasks were recorded to calculate evaporation. Leachate samples were filtered (0.22 μm) and acidified (2% v/v ultrapure HNO_3, Aristar ®, UK). Cation analysis was performed by inductively coupled plasma - optical emission spectrometry (ICP-OES) with an Optima 7000 DV (Perkin Elmer, USA) with detection limits (MDL) for Ca, Mg, Na, and Si at 0.13, 0.01, 0.05, and 0.06 mg/L, respectively. Anion analyses was performed on un-acidified samples by ion chromatography (IC) using a Dionex/ Thermo Scientific ICS-1100 with detection limits for Fl, Cl, NO_3^-, and PO_4^{3-} at 0.035, 0.048, 0.014, and 0.046 mg/L, respectively. Trace element analysis was performed by the Trent Water Quality Centre using inductively coupled plasma - mass spectroscopy (ICP-QQQ-MS) using an Aligent 8000 Triple Quadrupole ICP-MS with detection limits for Al, Cr, Co, Ni, and Cu at 0.633, 0.097, 0.0024, 0.095, and 0.024 ppb, respectively. Blanks and standards (10 ppm Ca standard for ICP-OES, Ricca Chemical, USA, and VeriSpec© Mixed Anion Standard 7, Ricca Chemical, USA) were used to verify the accuracy of these methods.

Suspensions of reacted solids were transferred to 50 mL plastic tubes and centrifuged (Sorvall™ ST 16, Thermo Fisher Scientific) at 13,000 rpm for 30 min. Supernatants were decanted, and the solids were rinsed by resuspending the solids in anhydrous ethanol by vortexing to prevent the precipitation of evaporites. This procedure was repeated 3 times. The recovered solids were dried at laboratory temperature for 24 h prior to being prepared for TIC and XRD analysis following the methods previously described.

2.3 Results

2.3.1 Characterization

Gahcho Kué kimberlite

The Gahcho Kué (GK) kimberlite residues are dominated by lizardite (29.4 wt.%), a target mineral for ERW and CO_2 mineralization. Other potential sources of Ca and Mg include phlogopite, forsterite, and saponite, which comprise 15.1, 9.2, and 21.5 wt.%, respectively. Calcite, the only carbonate mineral detected, accounts for 1.9 wt.% (Table 2.2). Regarding their geochemical composition, SiO_2, MgO and CaO constitute 43.0, 27.1 and 4.1 wt.%, respectively, of the residues (Table 2.4). Total inorganic carbon is present at 0.24± 0.01% (Table 2.4). The proportions of Mg, Ca, and Si for all samples, normalized to 100%, are displayed in Figure 2.1. The residues also contained 0.27 wt.% P_2O_5 and 2.46 wt.% K_2O, two important nutrients for plant growth. Ni and Cr, two elements of concern (EOC) in ERW studies, were present at concentrations of 1111 and 800 mg/kg, respectively (Table 2.5).

Venetia dark volcanoclastic kimberlite

Venetia dark volcanoclastic kimberlite (DVK) contains 26.5 wt.% lizardite. Other minerals that contain Ca and Mg include phlogopite, clinochlore, smectite, hydroxylapatite, and talc and have a combined abundance of 34.1 wt.% (Table 2.2). TIC and calcite comprise 0.86 ± 0.02% and 6.2 wt.% with the latter being the only carbonate detected. The DVK residues contain 20.2 wt.% MgO and 6.9 wt.% CaO, while SiO_2 makes up 41.7 wt.% (Table 2.3; Fig. 2.1). P_2O_5 and K_2O are present at 0.25 and 1.88 wt.%, respectively, while Ni and Cr were present at 771 and 539 ppm, respectively (Table 2.5).

Table 2.2. Quantitative mineralogy (wt.%) for kimberlite residue samples.

	Ca- and Mg-bearing minerals											Carbonates		Non-Ca, Mg minerals								
Sample	**Dio**	**Trm**	**Lz**	**Phl**	**Sap**	**Fo**	**Clc**	**Smc**	**Vrm**	**Hap**	**Tlc**	**Cal**	**Dol**	**Qtz**	**Mc**	**Ms**	**Prp**	**Plag**	**Ab**	**Or**	**Aug**	**Sep**
GK*			29.4	15.1	21.5	9.2	0.8				2.2	1.9		2.7	12.1				1.7		1.1	2.4
DVK*	7.9	5.1	26.5	8.4			7.9	13.6		0.9	3.3	6.2		3.2					5.5	2.3		
VSD T3	8.5	0.6	4.1	5.4			1.1	33.5			2.1	7.3	0.3	6.6	19.4				11.4			
VSD T5	9.2	0.5	4.5	4.3			1.3	35.5			1.2	6.8	0.6	4.2	19.4				12.4			
DIV	1.3		48.2	3.7		25.2			9.8			3.7				3.5	1	2.1				

Minerals identified include Dio– diopside, Trm– tremolite, Lz–lizardite, Phl– phlogopite, Sap–saponite, Fo– forsterite, Clc– clinochlore, Smc– smectite, Vrm– vermiculite, Hap–hydroxylapatite, Tlc– talc, Cal– calcite, Dol– dolomite, Qtz– quartz, Mc– microcline, Ms– muscovite, Prp– pyrope, Plag– plagioclase, Ab– albite, Or– orthoclase, Aug– augite, Sep– sepiolite. Retained weight percentages for GK, DVK VSD T3, and VSD T5 are 13.9, 7.9, 10.1, and 11.5, respectively. All samples sum to 100. Samples used in both Chapter 2 and 3 denoted with an asterisk.

Table 2.3. Quantitative mineralogy (wt.%) for other rock samples. Non-Ca/Mg bearing minerals comprise 33.1 wt.%, 1.1 wt.%, 3.8 wt.%, and 20.4 wt.% for WOL, OLI, QTZ, MKM, and MBA, respectively.

	Ca and Mg sources																Carbonates		
Sample	**Dio**	**Phl**	**Clc**	**Tlc**	**Trm**	**Lz**	**Fo**	**Ens**	**Wol**	**Ant**	**Brc**	**Io**	**Wod**	**An**	**Prg**	**Act**	**Cal**	**Dol**	**Mgs**
WOL*	38.9								20.6								2.6		
OLI*		0.16	1.3	0.2	0.1	7.9	81.8	7.5											
QTZ*																			
MKM										81	2.5	5.8	2.9					0.6	3.4
MBA			30.3											14.5	12.1	13.3	1.9		

Minerals identified include Dio– diopside, Phl– phlogopite, Clc– clinochlore, Tlc- talc, Trm– tremolite, Lz– lizardite, Fo– forsterite, Ens– enstatite, Wol– wollastonite, Ant– antigorite, Brc– brucite, Io– iowaite, Wod– woodalite, Cal– calcite, Dol– dolomite, Mgs– magnesite, Or– orthoclase, Qtz– quartz, Ab– albite, Ms– muscovite, Mt– magnetite, Hl–halite. Retained weight percentage for WOL is 12.4. all samples sum to 100. Samples used in both Chapter 2 and 3 denoted with an asterisk.

Voorspoed T3 and T5

Both Voorspoed samples (VSD T3 and VSD T5) share similar mineralogy, dominated by smectite (33.5 wt.% each), with Mg-bearing minerals including diopside (8.5 wt.% and 9.2 wt.%), and lizardite (4.1 wt.% and 4.5 wt.%). Calcite and dolomite comprise 7.3 wt.% and 0.34 wt.% of VSD T3, and 6.8 wt.% and 0.58 wt.% of VSD T5, respectively (Table 2.2), resulting in TIC values measured at 0.98 ± 0.04 % and 0.82 ± 0.03 %, respectively (Table 2.4). VSD T3 and VSD T5 are dominated by SiO_2, comprising 46.6 wt.% and 47.9 wt.%, respectively (Table 2.4). The CaO and MgO in both samples constitute 8–9 wt.% (Table 2.4). VSD T3 and VSD T5 contained 0.32 wt.% and 0.31 wt.% of P_2O_5, and 2.74 wt.% and 2.72 wt.% of K_2O (Table 2.4). Ni was found at 173 and 201 ppm concentrations, while Cr was found at concentrations of 341 and 335 ppm Cr, in VSD T3 and VSD T5, respectively (Table 2.5).

Diavik kimberlite

Residues from Diavik Diamond Mine (DIV) are primarily comprised of lizardite, representing 48.2 wt.% (Table 2.2), while other minerals with the potential to contribute Mg include forsterite (25.2 wt.%) and vermiculite (9.8 wt.%). Calcite (3.7 wt.%) is the only carbonate detected (Table 2.2), resulting in a TIC concentration of 0.69 ± 0.01% (Table 2.4). The geochemical composition shows 41.1 wt.%, 3.7 wt.%, and 32.5 wt.% SiO_2, CaO and MgO (Table 2.4; Fig. 2.1). P_2O_5 and K_2O comprise 0.18 wt.% and 0.58 wt.%, respectively (Table 2.4), while Ni and Cr comprise 1190 and 618 ppm, respectively (Table 2.5).

Table 2.4. Geochemical composition (wt.%) determined by XRF and carbon coulometry.

Sample	SiO_2	Al_2O_2	Fe_2O_3	MgO	CaO	K_2O	Na_2O	TiO_2	MnO	P_2O_5	Cr_2O_3	V_2O_5	LOI	TIC (n≥3)
Kimberlites														
GK*	43.01	5.09	7.03	27.1	4.05	2.46	0.57	0.54	0.12	0.27	0.16	0.01	9.32	0.24 ± 0.01
DVK*	41.77	6.71	8.14	20.24	6.91	1.88	1.01	0.76	0.16	0.25	0.15	0.02	11.69	0.86 ± 0.02
VSD T3	46.56	11.07	9.71	9.23	8.52	2.74	1.99	1.17	0.21	0.32	0.07	0.05	7.88	0.98 ± 0.04
VSDT5	47.91	10.93	10.02	8.12	8.69	2.72	1.93	1.23	0.21	0.31	0.07	0.04	6.99	0.82 ± 0.03
DIV	41.13	3.59	7.59	32.52	3.72	0.58	<0.01	0.38	0.12	0.18	0.15	<0.01	9.61	0.69 ± 0.01
Other rocks														
WOL*	56.73	4.07	2.08	5.81	26.27	0.91	1.66	0.21	0.04	0.05	0.02	<0.01	2.21	0.29 ± 0.06
OLI*	42.03	0.39	7.21	49.82	0.21	0.03	<0.01	0.01	0.11	<0.01	0.22	<0.01	0.61	0.01 ± 0.006
QTZ*	98.27	0.21	0.21	0.28	0.18	0.03	0.03	0.03	<0.01	<0.01	0.05	<0.01	0.81	0.005 ± 0.003
MKM	31.07	0.32	6.75	40.32	0.26	0.18	0.66	<0.01	0.09	<0.01	0.18	<0.01	20.36	0.63 ± 0.005
MBA	44.31	4.52	13.46	9.26	8.89	0.45	1.86	1.86	0.23	0.21	0.03	0.05	4.96	0.09 ± 0.001
Detection limits (%)	0.01	0.01	0.01	0.01	0.01	0.01	0.01	0.01	0.01	0.01	0.01	0.01	-10	<2 µg C

TIC values are based on an average (n≥3), with their standard deviation represented. Samples used in both Chapter 2 and 3 denoted with an asterisk. LOI is the loss on ignition at determine gravimetrically at 1000 °C.

Wollastonite skarn

The wollastonite skarn (WOL) contains a greater abundance of diopside (38.9 wt.%) than wollastonite (20.6 wt.%). The only detectable carbonate is calcite, which is present at 2.6 wt.% (Table 2.3), constituting at 0.29 ± 0.06% TIC (Table 2.4). Non-Ca or Mg-bearing minerals comprise the remaining 37.9 wt.% (Table 2.3). CaO, MgO, and SiO_2 constitute 26.3, 5.8, and 56.7 wt.% of the geochemical composition, respectively (Fig. 2.1). P_2O_5 and K_2O make up 0.05 wt.% and 0.91 wt.%, respectively (Table 2.4). Ni and Cr have concentrations of 16 and 2.3 ppm, respectively (Table 2.5).

Olivine sand

This olivine sample (OLI) contains 81.8 wt.% forsterite, 7.9 wt.% lizardite, and 7.1 wt.% enstatite. The remaining 2.8 wt.% was made up of clinochlore, phlogopite, talc, and tremolite (Table 2.3). No carbonate minerals were detected in OLI, although it was found to have 0.01 ± 0.006% TIC (Table 2.4). The geochemistry shows CaO, MgO, and SiO_2 constitute 0.2 wt.%, 49.8 wt.%, and 42 wt.%, respectively (Table 2.4). P_2O_5 and K_2O comprise <0.01 wt.% and 0.03 wt.%, respectively (Table 2.4). The concentrations of Ni and Cr are 2276 and 695 ppm, respectively (Table 2.5).

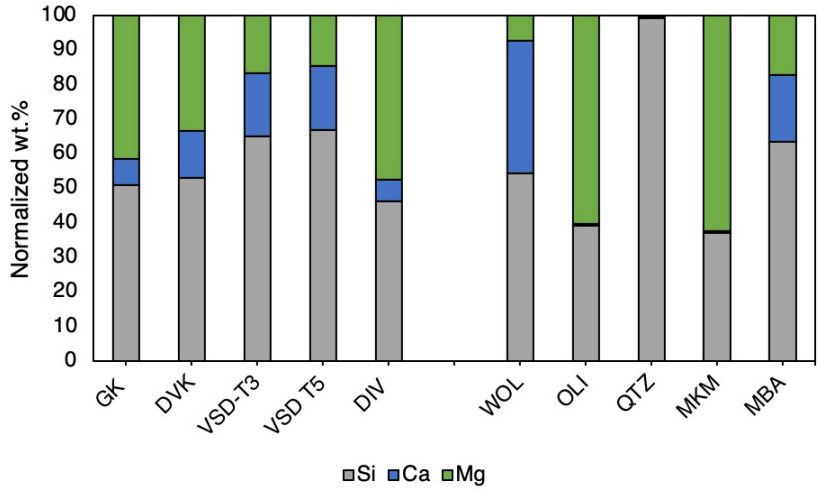

Figure 2.1. Proportions of Si, Ca, and Mg in samples determined as oxides by XRF and converted to cation concentrations.

Quartz sand

Quartz (QTZ) has a geochemical composition of 98.27 wt.% SiO_2, 0.18 wt.% CaO, and 0.28 wt.% MgO (Table 2.4). No minerals other than quartz were identified (Table 2.3), yet TIC was found at 0.005 ± 0.003% (Table 2.4). P_2O_5 was found below detection (<0.01%), while K_2O was determined to make up 0.03 wt.% (Table 2.4). The concentrations of Ni and Cr are 9 and 12 ppm, respectively (Table 2.5).

Mount Keith tailings

The tailings from the Mount Keith Nickel Mine (MKM) are dominated by antigorite, making up 81 wt.% of the sample, while Mg-hydroxides brucite, iowaite, and woodalite comprise 2.5 wt.%, 5.8 wt.%, and 2.9 wt.%, respectively. Dolomite and magnesite were found to make up 0.6 wt.% and 3.4 wt.%, respectively (Table 2.3), representing the only two carbonates identified, yielding 0.63 ± 0.005% TIC (Table 2.4). MKM tailings contain 0.26, 40.3, and 31 wt.% CaO, MgO, and SiO_2, respectively (Table

2.4; Fig. 2.1). P_2O_5 is found below detection limits (<0.01 wt.%), while K_2O was determined to contribute 0.18 wt.% to MKM's composition (Table 2.4). Ni and Cr are present in MKM at 1680 and 1015 ppm concentrations, respectively (Table 2.5).

Table 2.5. Trace element abundances in solid samples as determined by ICP-MS

(mg/kg)	As	Ba	Co	Cr	Cu	Li	Ni	Pb	S (%)	Sr	Ti (%)	Zn	Zr
Kimberlites													
GK*	5	1336	73	800	52.5	48	1111	10	0.08	528	0.32	73	124
DVK*	<3	649	57	539	104	25	771	7	0.05	375	0.42	77	75.5
VSD T3	12	1869	37	341	92.2	16	173	9	0.42	560	0.71	90	142
VSD T5	7	1160	41	335	103	15	201	7	0.17	543	0.67	103	149
DIV	6	883	76	618	36.7	25	1190	8	0.19	348	0.22	63	50.5
Other rocks													
WOL	<3	148	5	23	15.7	12	16	<2	0.63	1457	0.12	23	27.6
OLI	<3	12	115	695	3	1	2276	<2	0.02	19.7	<0.01	41	2.7
QTZ	<3	15	1	12	4.4	1	9	<2	0.02	10.5	0.02	12	115
MKM	8	7	41	1015	113	<1	1680	5	0.85	14.7	0.02	45	2.5
MBA	<3	196	67	153	48.8	25	146	<2	0.06	171	1.09	120	34.4
Detection limits	3	1	1	1	0.5	1	1	2	0.01	0.5	0.01	1	0.5

Metabasalt amendment

This metabasalt sample (MBA) contains 30.3 wt.% clinochlore, 14.5 wt.% antigorite, 12.1 wt.% pargasite, and 13.3 wt.% actinolite (Table 2.3). CaO, MgO and SiO_2 comprise 8.9 wt.%, 9.2 wt.%, and 44.3 wt.% of the sample's geochemistry (Table 2.4; Fig. 2.1). Measurements of TIC indicate its presence at 0.09 ± 0.001% (Table 2.4), contributed by the 1.9 wt.% calcite that comprises the sample. P_2O_5 and K_2O are present in MBA at concentrations of 0.21 wt.% and 0.45 wt.%, respectively (Table 2.4). The amount of Ni and Cr was determined to be 146 and 153 ppm, respectively (Table 2.5).

Table 2.6. Summary of initial concentrations (g/kg), and the percentage that was lost during leaches.

	Concentration (g/kg)						% Leached					
	Ca	**Mg**	**Si**	**Ni**	**Cr**	**TIC_I (%)**	**Ca**	**Mg**	**Si**	**Ni**	**Cr**	**TIC_L (%)**
Kimberlites												
GK	28.91	163.29	200.97	1.12	0.77	0.24± 0.01	33.9± 0.04	2.9± 0.07	1.2± 0.01	0.007	1.1E-05	83.9± 16.8
DVK	49.29	122.31	195.23	0.77	0.54	0.86± 0.02	41.7± 5.19	2.4± 0.41	0.3± 0.04	0.006	2.0E-05	73.2± 13.1
VSD T3	60.89	55.77	217.61	0.20	0.34	0.98± 0.04	28.3± 6.57	0.8± 0.25	0.1± 0.03	0.001	0.0	77.1± 1.7
VSD T5	62.11	49.06	223.87	0.17	0.34	0.82± 0.03	38.7± 4.65	0.9± 0.15	0.1± 0.01	0.001	0.0	69.9± 15
DIV	26.58	196.49	192.23	1.19	0.62	0.69± 0.01	67.7± 0.74	4.4± 0.06	1.5± 0.06	0.024	2.9E-05	98.1± 0.5
Other rocks												
WOL	187.74	35.04	265.14	0.02	0.02	0.29± 0.06	15.1± 1.22	0.1± 0.03	1.1± 0.13	0.007	3.0E-04	88± 6.2
OLI	1.43	301.02	196.44	2.28	0.71	0.01± 0.01	6.1± 1.46	0.7± 0.17	0.6± 0.14	0.001	7.0E-05	b.l.
QTZ	1.29	1.69	459.29	0.01	0.01	0.005± 0.0	20.8± 5.77	6.6± 1.9	0.01± 0.0	0.009	1.5E-04	b.l.
MKM	1.86	243.62	145.21	1.68	1.02	0.63± 0.01	95.3± 1.18	15.2± 0.19	0.7± 0.05	0.039	3.2E-06	86.4± 9.5
MBA	63.53	55.95	207.05	0.15	0.15	0.09± 0.0	26.7± 4.94	4.3± 0.37	0.3± 0.05	0.004	2.3E-04	96.9± 0.5

Analytes that were below detection are noted as b.l.

2.3.2 Batch leaches

Ca, Mg and C release

The release of Ca from kimberlite samples ranged from 9.8–24 g/kg, with all samples other than GK yielding >15 g/kg (Fig. 2.2A). What was observed in the leachate corresponds to a release of between 28.3%–41.7% of the samples Ca in all samples other than DIV which released 67.7% of its Ca (Table 2.6). The only other feedstocks to release significant amounts Ca were WOL (28.2 g/kg) and MBA (16.9 g/kg), which equate to 15.1% and 26.7% of their total Ca, respectively (Table 2.6).

Mg released by kimberlites showed a range of 0.4–8.7 g/kg (Fig 2.2B). The 0.4 g/kg released by VSD T3 and VSD T5 represent <1% of the total Mg in the sample, while the Mg observed in the leachates of GK (4.8 g/kg), DVK (2.9 g/kg), and DIV (8.7 g/kg) equate to 2.9%, 2.4%, and 4.4%, respectively (Table 2.6). The Mg released from OLI and QTZ is similar, with 1.9 and 2.3 g/kg observed in the leachate, respectively, representing 0.7% and 4.3% of their total Mg (Table 2.6). MKM released the most Mg, measuring at 36.9 g/kg (Fig 2.2B), which equals 15.2% of the total concentration in the sample. Less than 0.1 g/kg was released from both WOL and QTZ, which represent 0.1% and 6.6%, respectively.

Apart from GK and DIV which produced 2.4 and 2.9 g/kg, respectively, Si released to the leachate from kimberlites were all below 0.5 g/kg (Fig 2.2C). The values observed in the GK, and DIV leachate represent 1.2% and 1.5% of their respective Si concentrations, while the remaining kimberlites released <0.3% (Table 2.6). WOL released the highest Si values observed in the other feedstocks at 2.9 g/kg, representing 1.1% of its total Si. OLI, MKM, and MBA released 1.1, 1, and 0.6 g/kg, which equals 0.6%, 0.7%, and 0.3% of each samples total Si, respectively.

A loss of 70%–98% TIC was observed in kimberlites (Table 2.6), with all final solids containing <0.25% TIC (Fig. 2.3). The lowest final values were observed in DIV and GK, which were 0.04% and 0.01%, respectively, indicating a loss of 84% and 98% of their initial concentrations. WOL, MKM, and MBA lost between 88% and 97% of their TIC during the leaches, resulting in final values <0.03% TIC (Fig. 2.3). The change in TIC observed in OLI and QTZ falls within the detection limits of the instrument (Fig. 2.3), leading to the assumption that 100% of each samples TIC was leached (Table 2.6).

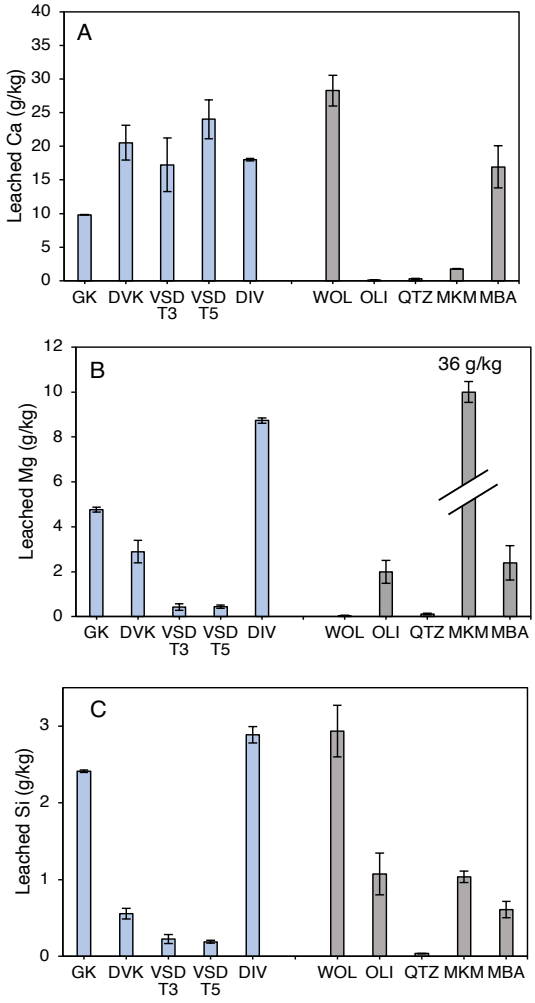

Figure 2.2. Leached Ca (A), Mg (B), and Si (C) compared between kimberlite (blue bars) and other rock types (grey bars). Concentrations are represented as the mass of the cation released per mass of sample in g/kg. Results are an average of triplicate leaches with standard deviation presented as error bars.

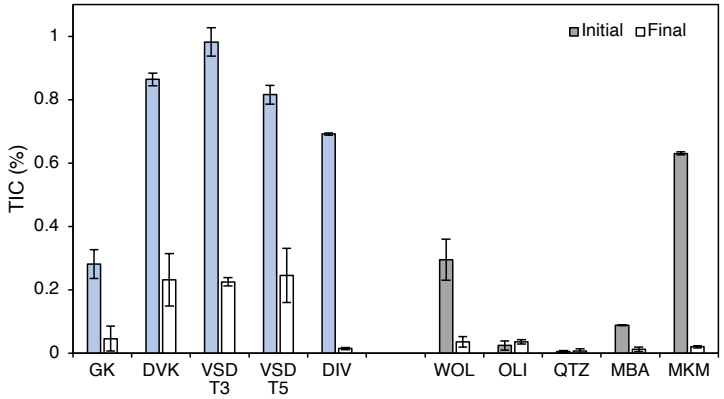

Figure 2.3. Comparison of TIC (%) in feedstocks pre- and post-leach. Values are an average of triplicate leaches with standard deviations being represented with error bars.

pH

An initial pH of 3.9 was observed, given the equilibrium between deionized water and 100% CO_2, as confirmed by geochemical modelling using PHREEQC. All kimberlite columns buffered the pH of the solution into the range of 5.22–5.42 with the highest final pH observed in the leachates of DIV (Fig. 2.4). WOL, MKM, and MBA buffered the solution to 5.31, 5.24, and 5.36, respectively (Fig. 2.4). OLI provided the least buffering of all feedstocks, with a final pH of 4.41, while QTZ experienced no change between the initial and final pH of the solution (Fig. 2.4).

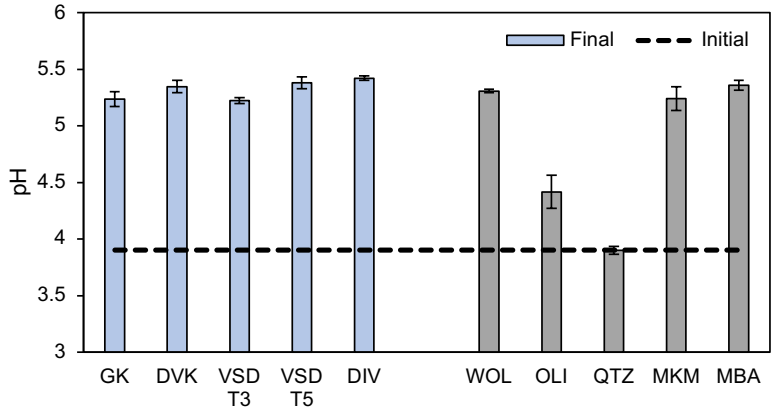

Figure 2.4. Changes in pH values observed in initial leaching solution and final solution post-leach. Initial values of 3.9 are determined through PHREEQC, and final values are an average of n=3 with error bars representing the standard deviation.

P and K release

Kimberlite samples varied greatly in the amount of P released during leaching, with VSD T3, VSD T5, and GK releasing 41.2, 57.4, and 59.7 mg/kg, respectively, while DVK and DIV released 14.1 and 9.8 mg/kg, respectively (Fig. 2.5a). MBA released the most P of all non-kimberlites, at 42.5 mg/kg, while WOL released 9.4 g/kg (Fig. 2.5a). No release of P was measured for OLI, QTZ, or MKM.

Release of K was observed to be <1.5 g/kg from both VSD samples and DIV, while GK and DVK released 2 and 4.5 g/kg, respectively (Fig. 2.5b). Both WOL and OLI released <0.25 g/kg, while QTZ showed no release of K (Fig. 2.5b). MKM and MBA released 1.3 and 2.6 g/kg, respectively (Fig. 2.5b).

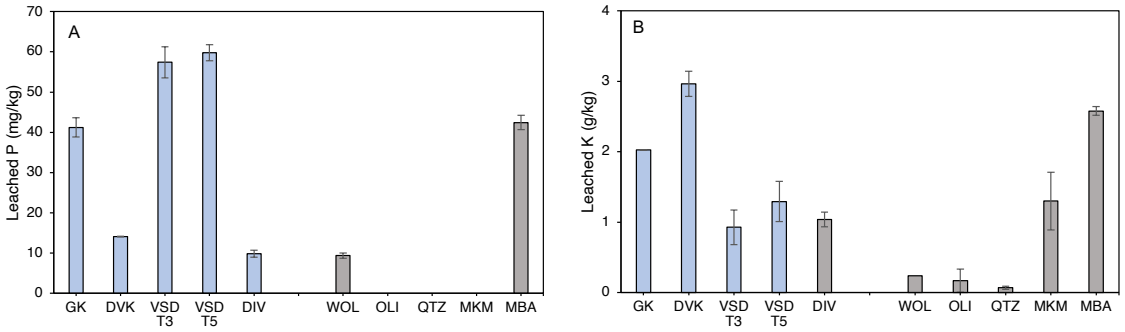

Figure 2.5. Phosphorus (A) and potassium (B) leached from the sample, represented as the mass of the cation released per mass of sample (mg/kg). Results are an average of triplicate leaches with standard deviations represented with error bars.

Ni and Cr release

The release of other trace elements outside the scope of this study was observed to be low and likely do not constitute a risk to environmental or human health, although further investigation may be required. High release of Ni was observed in DIV (290 mg/kg), compared to GK and DVK which released 77.5 and 45.9 mg/kg, respectively,

while VSD T3 and VSD T5 each released <2 mg/kg (Fig. 2.6a). Apart from MKM which showed Ni release of 682.4 mg/kg, all non-kimberlite samples released <1.3 mg/kg. The release of Cr from kimberlite samples was relatively low and ranged from 0.1–2.1 mg/kg. Similar values were observed in the leachates of the other samples, ranging from 0.1–0.7 mg/kg (Fig. 2.6B)

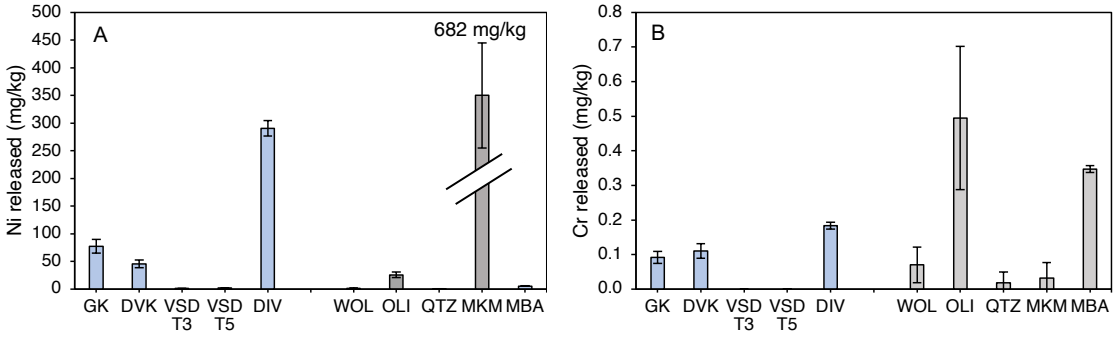

Figure 2.6. Nickel (A) and chromium (B) leached from the sample, represented as the mass of the cation released per mass of sample (mg/kg). Results are an average of triplicate leaches with standard deviations represented error bars.

2.4 Discussion

2.4.1 Mineral dissolution and cation release

The reactivity tests used in this study will aid in predicting the release of cations in mining environments or large-scale ERW projects. In addition, these tests can differentiate between non-carbonate (desirable) and carbonate (undesirable) sources of weathering products (Paulo et al., 2021) while assessing the release of beneficial nutrients and elements of concern. In this study, we demonstrate that batch leach tests are a valuable tool for predicting water chemistry in carbonic acid leaching environments and should be incorporated into the assessment and decision-making process of feedstock selection for geochemical CO_2 removal.

Kimberlites

Ca release from the kimberlite samples (~9–24 mg/kg; Fig. 2.2a) was significantly greater than Mg release (~0.5–9 g/kg; Fig. 2.2b), despite Mg (4.9–20.1 wt.%) being present at greater concentrations in the kimberlites than Ca (2.8–6.2 wt.%). The predominance of Ca in the leachate can be explained by the presence of highly soluble Ca-carbonate minerals (~2–7 wt.%), including calcite (Table 2.2), which was the predominant carbonate in all kimberlites, while VSD T3 and VSD T5 had dolomite present at low abundances of 0.34 wt.% and 0.58 wt.%, respectively (Table 2.2). Thermodynamics indicates that dolomite displays greater absolute and relative solubility to calcite below 25ºC and typically weathers preferentially in temperate watersheds (Drever, 2005; Langmuir, 1997; Szramek et al., 2011), although the samples with dolomite yielded the lowest Mg and two of the highest Ca concentrations of all

kimberlites (Fig. 2.2b). Leaching removed 70–80% of the TIC present in the kimberlites (Figure 2.3). The substantial loss of TIC validates that carbonate dissolution is a significant source Ca and Mg in kimberlite leachates, as made evident by buffering capacity observed in all kimberlites (Fig. 2.4).

The release of Si from the kimberlite samples was low (<3 g/kg; Fig. 2.2c) yet strongly correlated to the Mg leached (r^2=0.94), with values decreasing from 8.73–0.42 g/kg for samples DIV>GK>DVK>VSD. Dissolution of Mg-silicates is expected to be non-stochiometric due to the presence of labile Mg that can be released without the weathering of the bulk silicate structure (Vanderzee et al., 2019). Relevant target minerals for Mg leaching include lizardite ($Mg_3Si_2O_5[OH]_4$), forsterite (Mg_2SiO_4), and diopside ($MgCaSi_2O_6$). Slow dissolution kinetics of these silicate minerals can be attributed to the strength of Si-O bonds that hinder the release of Mg (Oelkers et al., 2018; Schott et al., 2009). The dissolution of Mg-silicate minerals has been the focus of many ERW studies (Assima et al., 2014b; Montserrat et al., 2017; Renforth et al., 2015a; Rinder and von Hagke, 2021). This source of weathering products is preferred for secondary carbonate precipitation because of the favourable kinetics of hydrated Mg-carbonate minerals (Hänchen et al., 2008), that can form at ambient temperature and pressure (Hamilton et al., 2021; Lechat et al., 2016; Power et al., 2009; Turvey et al., 2018; Wilson et al., 2014).

The percentages of Ca, Mg, and Si that were released from each sample indicate the reactivity of the feedstock and can be used for determining CO_2 sequestration potential. This is predicated on the conditions of the experiment being designed to facilitate the release of cations that are easily accessible and would comprise most of the reactivity observed under real-world conditions. The percentage of Ca released was

higher than any other cation, with values ranging between 28%–41%, except for DIV, which released 67%, while losing 98% TIC (Table 2.6). Furthermore, the Ca-bearing silicate minerals, including diopside, tremolite, and smectite (Table 2.2) are present at lower abundances than Mg-silicates. Smectite in DVK (13.6 wt.%) and both VSD samples (33.5 wt.% and 35.3 wt.%) is assumed to contribute to the release of cations via acid activation that results in the replacement of ions with protons (i.e., H^+) within the interlamellar layers of this clay mineral, an expected result given the constant supply of 100% CO_2 (Komadel, 2003; Paulo et al., 2021; Zeyen et al., 2022). Moreover, Zeyen et al. (2022) demonstrated that smectite minerals in kimberlites are a source of labile Ca^{2+} and Mg^{2+} for carbonation as shown by a positive correlation between cation exchange capacity and the abundance of saponite, a smectite group mineral. Ca contribution from the interchangeable layers of smectite may be occurring in our samples where the mineral is present (DVK, VSD T3, and VSD T5), which release the three highest amounts of Ca for kimberlites (Fig. 2.2a), although these samples also contain the most calcite.

The proportions of Mg released are much lower than Ca, with no sample releasing more than 5% of its total Mg content (Table 2.6). This finding is explained by the samples lack of easily dissolved Mg-carbonates and the slow dissolution rates of Mg silicates present which are not easily extractable without the use of high temperature and pressures (Power et al., 2020). The Mg released from the Mg-silicates within the kimberlites is labile, i.e., the readily released Mg from the very outer layers of the silicate structure (Thom et al., 2013a; Vanderzee et al., 2019). The low percentages of Si released from kimberlites (<1.6% of total Si) also emphasize the insufficiency of silicate weathering and indicates that the relatively high Ca releases originated from more labile

sources than Ca-bearing silicates (e.g., diopside). Dissolution rates for calcite are 10^{-10} to 10^{-7} mol/cm^2/s depending on pH, while most silicates have significantly slower rates between 10^{-16} and 10^{-10} mol/cm^2/s (Brantley and Olsen, 2014; Declercq and Oelkers, 2014). The correlation between Mg and Si release and the absence of Mg-carbonates (dolomite) in most kimberlites demonstrates Mg-silicate weathering. In contrast, the greater release of Ca, minor calcite abundances, and high loss of TIC during leaching are all indicative of carbonate weathering. Furthermore, the high buffering capacity of these kimberlites which raise the pH of the initial solution from 3.9 to the range of 5.22–5.42 indicates carbonate weathering is occurring, which is evident in comparison to the QTZ sample acting as a control which did not alter the pH of the solution (Fig. 2.4).

The kimberlite residues had large variations in grain size and specific surface areas (6.5–48 m^2/g; Table 2.1), which significantly affect mineral dissolution rates (Power et al., 2013). However, kimberlite residues are mineralogically complex and contain several minerals, each with individual surface areas and reactivities, resulting in a wide range of dissolution kinetics within one sample. Moreover, the high abundances of clays, up to ~40 wt.%, give the kimberlites high specific surface areas, while surface areas of the target Mg- and Ca-bearing silicates are unknown and likely to be substantially lower than the bulk sample. Thus, the specific surface areas of these mineralogically complex samples are not useful for interpreting leaching data in the scope of this study. Additionally, this measurement does not consider the accessibility of the mineral surfaces, which impacts many variables, including the precipitation of secondary carbonates (Harrison et al., 2015; Hövelmann et al., 2012). Although the leaching environment created by bubbling 100% CO_2 into solution mitigates mineral

precipitation during the experiment, it is a possibility that previous weathering of these samples has led to some degree of surface passivation that inhibits weathering of the bulk material. Nevertheless, it is expected that this would not impact dissolution rates, given the nature of the experiment.

Other feedstocks

The most prominent controls on a mineral's dissolution rate are its crystal chemistry, surface area, and the chemistry of the reacting fluid, and temperature of the environment (Power et al., 2013). In reactivity tests, the temperature and initial solution chemistry were consistent across all samples, leaving the crystal chemistry and surface area as the most prominent variables. As such, the abundance and surface area of target minerals (Table 2.3) within feedstocks, including diopside, wollastonite ($CaSiO_3$), forsterite (Mg_2SiO_4), brucite [$Mg(OH)_2$], clinochlore [$Mg_5Al(Si_3O_{10})(OH)_8$] and antigorite [$(Mg_3Si_2O_5(OH)_4$] will have the greatest effect on cation release.

WOL exhibited the greatest release of Ca (Fig 2.2a), which poses challenges for determining the source of this cation as both Ca-carbonate (calcite) and Ca-silicates (diopside and wollastonite) are present (Table 2.3). While wollastonite and diopside yield fast dissolution rates (Knauss et al., 1993; Power et al., 2013), the dissolution rate of calcite far exceeds both, which is made evident by the buffering capacity displayed by WOL, increasing the pH from 3.9 to 5.3 (Fig. 2.4). Analysis of TIC has been proposed as a method for extrapolating carbonate contributions of easily extracted Ca without requiring long exposure times or analysis of surface passivation of amorphous silica (Paulo et al., 2021), two factors that have been documented to influence ion release from

wollastonite and diopside (Knauss et al., 1993; Schott et al., 2009). The Ca released represents 15% of the total Ca present in the bulk sample (Table 2.6), which indicates that while the high reactivity of WOL can provide accessible cations, a large capacity for Ca release remains untapped. The relatively low surface area of the WOL sample (0.8 m^2/g), compared to others (Table 2.1), was more than compensated for by the high reactivity of the minerals present, mainly wollastonite and calcite. The TIC in the WOL sample was mostly leached, yet this sample also released the highest concentration of Si, indicating that despite Ca contributions from calcite dissolution, silicate weathering is occurring to an extent not seen in the other feedstocks. Previous studies have shown that wollastonite requires a longer exposure time (3000 h) to reach stoichiometric dissolution under acidic conditions (Schott et al., 2012), which are conditions not met in this leach. However, it can be assumed that non-stoichiometric dissolution is occurring given the impurity of the sample and the presence of labile ions that are readily released, leading to doubt of the source of Si values observed.

The amount of Ca released from OLI, QTZ, and MKM was very low (<2 g/kg) yet represented large proportions of the total Ca present in MKM (95%) and QTZ (20%), but only 6% of OLI (Table 2.6). Low concentrations of a cation in leachates that constitute a high percentage released indicates a reactive yet trace source of the cation. The 86% loss of TIC observed in MKM resulted in Mg contributions from its magnesite and dolomite, with the latter nearly entirely dissolving, evident by the release of 95% of the Ca present in this sample. Alternatively, ~20% of the Ca comprising QTZ was released, indicating a source of Ca. Although not detected using XRD, carbonates were likely present in trace abundances yet do not account for the extent of reactivity observed

in MKM, which is evident given the samples initial TIC. This result emphasizes that utilizing multiple characterization methods is needed to develop a complete understanding of a feedstock's suitability for ERW.

The Ca released from MBA was within the range observed in kimberlites, yet without as significant a contribution from carbonates, which were present at 1.9 wt.%. MBA is cumulatively dominated by actinolite anorthite, and pargasite, which are likely predominant sources of Ca. Moreover, the wt.% of CaO in this sample is second only to WOL. The increase in pH was the highest observed, which can be attributed to the reactivity of this feedstock. Correlated to this is the D50 particle size, which was the lowest observed at 11.7 μm, and a resulting surface area of 1.73 m^2/g, with no clays identified.

The Mg concentrations of the WOL (0.04 g/kg) and QTZ (0.11 g/kg) leachates were relatively low, which is consistent with the low abundances of Mg in these feedstocks. Furthermore, no Mg-bearing mineral phases were detected with XRD. Thus, the sources of Mg were either due to small contributions of cation via substitution or to trace phases not detectable with XRD. The inability to confirm sources of cations can pose challenges with estimating sequestration potentials, which emphasizes the need for TIC analysis. In the case of QTZ, very low concentrations of TIC were measured before and after leaches, while WOL lost 88% TIC. This result does not indicate whether the Mg was present as a carbonate mineral, but it does ensure that the cation release from non-carbonate sources is not being overestimated.

MBA contains a similar wt.% MgO as both VSD samples, yet releases significantly more, due to its high reactivity. The most dominant mineral in MBA is

clinochlore at 30.3 wt.%. Furthermore, MBA releases more Mg than olivine despite containing 5 times less MgO, indicating the necessity of a reactive phase that has a surface area that will facilitate rapid dissolution. MBA also released one of the highest percentages of its Mg, and with no Mg-carbonates detected, it can be assumed to be sourced from silicates.

OLI contained the greatest proportion of Mg of all the samples. Yet, the Mg leached from olivine was relatively low (~0.6%). However, high release percentages are not expected when a feedstock contains large concentrations of a cation in its whole rock geochemistry without the presence of a very reactive phase. OLI had a coarse particle size and the lowest specific surface area of all the feedstocks analyzed. It has been estimated that olivine requires a particle size of <10 μm to fully dissolve within seawater over 100 years (Hangx and Spiers, 2009), while a particle size of 0.1–0.01 μm is needed for complete dissolution within five years when applying olivine to soil (Renforth et al., 2015a). The olivine used in this experiment has an average particle diameter of 453 μm, which is twice as large as WOL, and ten times as large as MKM, indicating a significantly lower surface area and resulting dissolution rate than what is required for accelerated cation release. If requisite dissolution for ERW cannot be met through a leach like the one performed in this study, changes need to be made to the feedstock for it to be suitable for large-scale deployment. While reducing the grain size of a feedstock can lead to faster weathering rates, it can also increase the energy requirement for ERW deployment, resulting in a decline in efficiency (Rinder and von Hagke, 2021).

The highest Mg release was observed in the leachate of MKM (36.9 g/kg), significantly greater than of MBA (2.3 g/kg), the second highest value seen in non-

kimberlite feedstocks. This release is attributed to the highly reactive nature of the Mg-bearing minerals found in MKM, which include brucite, iowaite ($Mg_6Fe^{3+}_2[OH]_{16}Cl_2$ $4H_2O$), and woodalite ($Mg_6Cr_2[OH]_{16}Cl_2$ $4H_2O$). Brucite is a well-studied target mineral for CO_2 sequestration (Entezari Zarandi et al., 2016; Harrison et al., 2013; Pokrovsky and Schott, 2004; Power et al., 2020; Stubbs et al., 2022), and while iowaite and woodalite have received less attention, they have been identified as minerals with considerable potential for CO_2 sequestration (Mills et al., 2011; Turvey et al., 2018; Wilson et al., 2014). The importance of such reactive mineral phases is emphasized by comparing the results of the MKM to OLI leaches. MKM released 18× more Mg than OLI, despite both samples very high Mg concentrations as a whole rock (243 and 301 g/kg, respectively). While differences in surface area play a role, the reactivity of Mg-hydroxide minerals has been documented to show that fast and near-complete dissolution can be met with increased pCO_2 (Harrison et al., 2013), making them significant target minerals for CO_2 sequestration (Entezari Zarandi et al., 2016; Power et al., 2020; Turvey et al., 2018; Zhao et al., 2010). However, a TIC loss of 86% was determined for MKM, resulting in identified carbonate phases (magnesite and dolomite) contributing to the values of Mg observed.

2.4.2 CO_2 sequestration

The total capacity for CO_2 sequestration of a given sample can be determined using its geochemical composition, and the assumption of complete conversion of its non-carbonate Ca and Mg content to carbonate products on a mole-per-mole basis (Eq. 2.1). These capacities are theoretical, and unlikely to be achieved in a realistic timeframe for use as an NET due to sluggish dissolution of most feedstocks at ambient temperature

and pressure (Assima et al., 2014b; Li et al., 2018; Power et al., 2013; Thom et al., 2013b). Therefore, a protocol has been developed by Paulo et al. (2021), that calculates a given feedstock's potential for CO_2 sequestration, based on easily released Ca and Mg from non-carbonate sources (Eq. 2.2):

$$CO_2(kg/t) = [(molC_{cation} - molC_{TIC}) \times M_C]\frac{M_{CO_2}}{M_C} \times \frac{1\ g}{1000\ kg} \quad (2.2)$$

where $molC_{cation}$ represents the equivalent moles of C based on the release of Ca and Mg on a per tonne basis, $molC_{TIC}$ is the moles of C released from the sample as a loss of TIC on a per tonne basis, while M_c and M_{CO2} are the molar masses (g/mol) of C and CO_2, respectively. This calculation assumes a 1:1 molar ratio between the cations being released into solution and C with the potential for mineralization. The subtraction of all moles of C released via the dissolution of carbonates, represented as TIC loss, ensures all Ca and Mg being considered is from non-carbonate sources, e.g., silicates or hydroxides. Moreover, treating Ca and Mg release as one entity and subtracting the TIC loss from their sum ensures that all sources of carbonates are being considered, including low abundance Mg-carbonate phases that may not be identified via XRD. Furthermore, Ca and Mg are the only cations considered due to their prevalence as secondary carbonate forming ions. This methodology allows for the distinguishment between CO_2 sequestration capacity (Fig. 2.7A) and CO_2 sequestration potential (Fig. 2.7B), which is an often overlooked yet critical aspect of feedstock evaluation (Paulo et al., 2021).

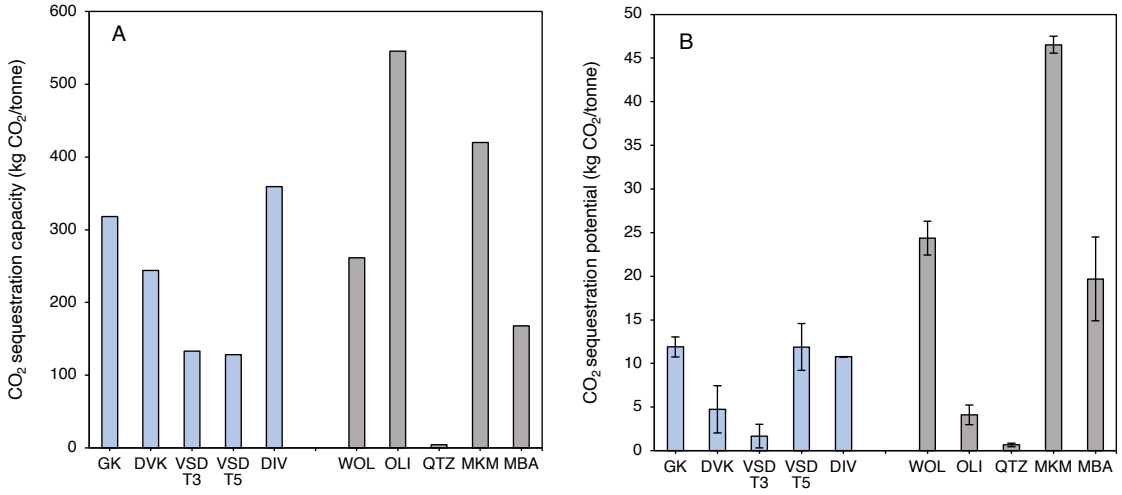

Figure 2.7. A) Maximum capacity for CO_2 sequestration based on whole rock geochemistry assuming 100% carbonation of Ca and Mg from non-carbonate sources to form a carbonate with a 1:1 cation: carbon molar ratio. B) CO_2 sequestration potential of feedstocks based on easily extractable cations, assuming 100% conversion of Ca and Mg released to form carbonates with a 1:1 molar ratio, corrected for Ca and Mg contributions from carbonate sources. Values are an average of triplicate leaches with standard deviations being represented with error bars.

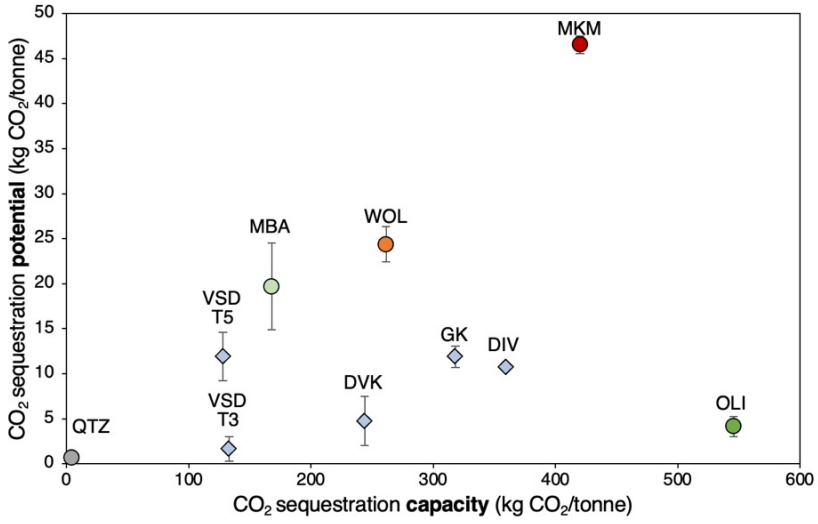

Figure 2.8. Maximum capacity for CO_2 sequestration versus potential for CO_2 sequestration based on easily extracted cations from non-carbonate sources. Potential values are an average of triplicate leaches with standard deviations represented with error bars.

Kimberlites

The CO_2 sequestration capacities of kimberlites range between 130–360 kg CO_2/t (Fig. 2.7A). The residues from Voorspoed (VSD T3, T5) show the two lowest capacities, attributed to their high TIC and lower abundances of Mg that were at least half of what is observed in other kimberlites (Table 2.4). Despite its low capacity, results of the leach indicate that VSD T5 is equal to the GK sample for the CO_2 sequestration highest of 11.9 kg CO_2/t (Fig. 2.7B). While VSD T5 had a greater capacity, VSD T3 showed the lowest potential for CO_2 sequestration of all kimberlites, yielding 1.7 kg CO_2/t (Fig. 2.7B). The discrepancies observed between capacity and potential for the VSD samples result from Ca being released at a higher proportion in T5, with less of these contributions attributed to carbonate sources. This result emphasizes the importance of TIC contributions when determining sequestration potentials. The potential CO_2 sequestration capacities of GK and DVK were estimated at 11.9 and 4.8 kg CO_2/t, respectively (Fig. 2.7B). Despite having a significantly higher capacity, the CO_2 sequestration potential of 10.7 kg CO_2/t for DIV is comparable to GK and VSD T5 estimates (Fig. 2.7B).

Ideal feedstocks have both high CO_2 sequestration capacities and potential (Fig. 2.8), the latter being an indication of reactivity. GK and DVK (Fig 2.8) have higher capacities and CO_2 sequestration potentials than the other kimberlites and would be best suited for CO_2 sequestration. Apart from the VSD samples, all kimberlites used in this study fit within the range of kimberlites analyzed by Paulo et al. (2021). Variances between the results of DVK measured by this study and Paulo et al. (2021) illustrate difficulties regarding the heterogeneity of kimberlites.

Kimberlites with low sequestration potentials can still be an asset for ERW given their sequestration capacities are high enough to warrant investments in pre-treatments like further grinding and processing. In our study, GK, DVK, and DIV are an example of this as they yield significant capacities that aren't fulfilled by their potentials. Although individual assessment of each feedstock is required to determine the feasibility of pre-treatment. Furthermore, these kimberlite residues have large CO_2 sequestration capacities due to the scale at which they are produced. For example, Venetia treated 4.7 Mt of kimberlite ore in 2016 with a maximum capacity to offset 0.84–1.47 Mt CO_2 assuming complete carbonation of all non-carbonate Ca and Mg (Mervine et al., 2018). However, the labile Ca and Mg released from non-carbonate sources is a more relevant assessment, as these cations provide the portion of CO_2 sequestration capacity that can be achieved in a more realistic time frame.

Passive CO_2 sequestration has been well documented at mines that produce ultramafic residues (Li et al., 2018; Power et al., 2020; Stubbs et al., 2022; Wilson et al., 2014). There are ~419 Mt of ultramafic and mafic mine tailings being produced annually that include those from diamond mines (Power et al., 2014). Furthermore, Bullock et al. (2021) estimate there is a potential to sequester ~1.1–4.5 Gt CO_2 annually using mine tailings, including those from non-mafic and ultramafic deposit types. Harnessing the often-untapped potential of mine wastes to sequester CO_2 sequestration can contribute to reducing a mine's net annual CO_2 emissions. Thus, knowledge of the capacity and potential for CO_2 sequestration of a mine's tailings can be of great importance for mining operations. In this study, the five ultramafic kimberlite residue samples and one ultramafic tailings sample from a nickel mine, yielded varying results. Despite very high

capacities in three of the five kimberlites, all potentials were relatively low compared to the nickel tailings. As a result, we see the importance of engineering storage environments to facilitate higher degrees of mineral dissolution needed for increasing CO_2 sequestration. For instance, Stubbs et al. (2022) recommends changes to the residue deposition plan at the Venetia Diamond Mine to optimize their saturation, expose mineral surfaces, and as a result, promote the release of easily extractable cations. Our methods can be used as a tool for the mining industry, ultimately resulting in increased success of efforts to facilitate CO_2 sequestration.

Other feedstocks

The CO_2 sequestration capacities of the non-kimberlite feedstocks varied considerably. The sample with the highest capacity was OLI (545 kg CO_2/t; Fig. 2.7A). Nearly half of this sample by mass is MgO, which resulted in a capacity that exceeds all other samples by at least 125 kg CO_2/t. However, this did not translate to any significant CO_2 sequestration potential, yielding only 4 kg CO_2/t (Fig. 2.7B). Despite OLI having approximately twice the capacity that was observed in WOL, its potential was a quarter of WOL (Fig 2.8). This lack of potential is attributed to lower reactivity, with wollastonite having a dissolution rate of 10^{-12} mol/cm^2/s compared to forsterites 10^{-13} mol/cm^2/s at the observed pH (Power et al., 2013). While olivine lacks the reactivity of hydroxide-bearing feedstocks, an important consideration in this study is the grain size and resulting surface area known to have significant impacts on dissolution and cation release. OLI has a D50 particle size of 423 μm, which was the highest observed, and a BET surface area of 0.2 m^2/g, the second lowest behind QTZ. Consequently, significant

grinding of this sample (and others) would be required to produce a grainsize conducive for large-scale CO_2 removal. Rinder and von Hagke (2021) estimate that the CO_2 removal facilitated by less reactive feedstocks, like basalt, will be cancelled out by processing and transportation emissions, at a grainsize of 100 μm. It is proposed that a grainsize of <10 μm is needed to contribute a significant CO_2 drawdown. Although, requisite grainsize for considerable CO_2 removal is in contention, with theoretical values indicating that the smaller grainsizes equal higher offsets, while it has been shown that hydrologic factors such as residence time and mineral to water ratio can be more important than grain size and surface area (Amann et al., 2022).

The highest CO_2 sequestration potential was observed from MKM due to the high reactivity of brucite. Similar batch leaches were performed on brucite slurries exposed to 100% CO_2 yielding the precipitation of nesquehonite, despite evidence indicating that the gaseous CO_2 being injected was not in equilibrium with the solution (Harrison et al., 2013). This result suggests that the limiting factor for brucite carbonation is the supply of CO_2, rather than dissolution limitations observed in less reactive feedstocks (Harrison et al., 2013). However, in our study, the conditions prevented the formation of secondary carbonates, including the constant supply of 100% CO_2 and the small mass of brucite present (~6.25 mg in 250 mg MKM). Thus, brucite dissolved during the experiment, contributing to the easily released Mg seen in this sample that led to its high sequestration potential. Although the extent of brucite dissolution cannot be determined within the parameters of this study, XRD analysis of the recovered solids may be capable of quantifying the percent of each mineral released. Despite this, it has been shown that brucite is highly reactive with CO_2 (Harrison et al., 2013; Pokrovsky and Schott, 2004;

Power et al., 2020; Stubbs et al., 2022; Zhao et al., 2010) and expected to make significant contributions to the CO_2 sequestration potential of MKM tailings, and while we see less silicate weathering than in the best performing kimberlites analyzed (Fig. 2.2), the capacity significantly greater than all other samples. Thus, emphasizing the importance of feedstock reactivity, and how small proportions of a highly reactive mineral (in this case, 2.5 wt.%) can have a significant impact on CO_2 sequestration potential.

The second highest CO_2 sequestration potential is seen in WOL with a value of 24.3 kg CO_2/t (Fig. 2.7B). Wollastonite has significantly faster dissolution rates than most Mg-silicates, and has shown great potential for carbonation (Huijgen et al., 2006). Fig 2.8 emphasizes the high capacity and reactivity of WOL, second only to MKM. Our results reinforce the potential for wollastonite skarn to be used as a feedstock for large-scale deployment of ERW, which has been proposed through recent findings (Haque et al., 2019), and realized through field trials (Haque et al., 2020; Taylor et al., 2021). The 15-year field trials in an experimental forest deployed by Taylor et al. (2021) captured 223 kg CO_2/t, approximately 10 times the sequestration potentials observed in our study. This discrepancy is likely be attributed to the grain sizes used and its impact on reactivity, as the wollastonite powder used by Taylor et al. (2021) was believed to have fully dissolved within 1 year of application. This finding is consistent with the CO_2 sequestration capacity of the wollastonite skarn used in our study that would capture ~250 kg CO_2/t assuming 100% conversion of Ca and Mg released to carbonates using a 1:1 molar ratio, corrected for Ca and Mg contributions from TIC loss. However, despite

how promising the results of large-scale ERW trials have been, it is essential to consider weathering products beyond those which can be mineralized for CO_2 sequestration.

2.4.3 Deleterious metals

Deleterious metals released into agricultural soils can cause environmental harm, particularly the introduction of Ni and Cr into the food chain and resulting bioaccumulation that can lead to adverse human health risks (Haque et al., 2020). Ni and Cr releases may limit the amount of ERW feedstocks that can be applied to agricultural soils (Vasiluk et al., 2019), thus reducing capacity to sequester CO_2. For these limits to be identified, comprehensive knowledge of the feedstocks and the soils they are being amended to is required.

No Ni-or Cr-bearing mineral phases were identified using XRD in any of the feedstocks, suggesting that these metals are present in minerals with abundances below detection or substituted in other phases. The Ni released on a per mass basis (mg/kg) shows considerable variation between kimberlites (Fig. 2.5A). DIV (290.7 mg/kg) released nearly 4× more Ni than GK and ~6× than DVK, despite similar Ni concentrations. This discrepancy could be attributed to a combination of DIVs large surface area, which is more than double GK and quadruple DVK, and likely a more recalcitrant source of Ni in these samples. The two VSD samples exhibited exceptionally low Ni release compared to other kimberlite samples and reflects the low Ni concentrations of these kimberlites (Table 2.5). The release of Cr was low for all kimberlites, with no sample releasing more than 0.2 mg/kg. The concentrations of Cr in the whole rock geochemistry for these kimberlites are not much less than what was

observed for Ni, but despite this, Ni releases on a g/kg basis were ~3 orders of magnitude greater than Cr in some instances (Fig. 2.5B). Ni mobilization via weathering results in the release relatively stable Ni^{2+} which has a high mobility in aqueous solutions, compared to less soluble Cr species, which are governed by its oxidation states (Kabata-Pendias, 2000). Cr observed in these feedstocks is likely Cr^{3+} which has a similar ionic size to Fe^{3+} and Al^{3+}, allowing for substitution into mineral structures, however, when released in oxidizing environments can form the very mobile chromate ion ($CrO^{2}_{4}{}^{-}$) that is easily adsorbed by clays (Kabata-Pendias, 2000). This process may be occurring during the leaches, with the most Cr being found in the leachate of the kimberlite with the lowest clay content (DIV), despite containing less Cr than samples with more clays (GK).

The Ni released from the other feedstocks was below 26 mg/kg, except for MKM that released 682 mg/kg. This latter result is consistent with the MKM tailings being from a low-grade nickel deposit, where the processing of the serpentinite ore can be inefficient, often resulting in the recovery of only 70% nickel (Senior and Thomas, 2005). Release of Ni from OLI totalled 26 mg/kg (Fig. 2.5), which is considerably higher than the findings of ten Berge et al. (2012) who reported a range 0.09–1.38 mg/kg of bioavailable Ni in their olivine treated ryegrass pots. The discrepancy can be attributed to the intensity of our leaches, which are designed to facilitate weathering thar far exceeds what would occur under the natural rates reported by ten Berge et al. (2012). As a result, the values reported in their study are significantly lower than the toxicity threshold of 10 mg/kg for bioavailable Ni (Kabata-Pendias, 2010), while even our Ni release is less than the soil quality guidelines for environmental health total Ni allowance of 45 mg/kg (Haque et al., 2020). The release of Cr from OLI was the highest observed at 0.5 mg/kg but showed a

considerable standard deviation of ±0.2 mg/kg. The release of 0.3 mg/kg observed for MBA is within the range of OLIs standard deviation and represents the second highest Cr release in this experiment. Cr composes relatively high concentrations of olivine-rich ultramafic rocks (e.g., peridotites including dunite, harzburgite, lherzolite, and wehrlite), according to a synthesis of published chemical analyses (Beerling et al., 2018), which validates our findings that OLI and MBA release the most Cr.

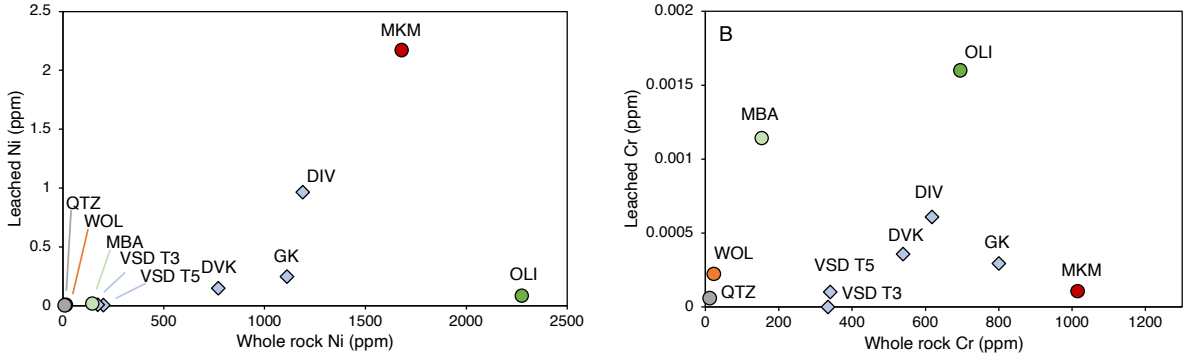

Figure 2.9. The concentrations of Ni (A) and Cr (B) that comprise the geochemistry of each feedstock plotted versus the amount of each element released during the leaches, indicating the feedstocks ability to provide the nutrients that they contain.

The proportions of Ni and Cr leached from each sample during the leaches plotted against total Ni and Cr provide insights into how a feedstock may pose an environmental risk based on its reactivity. Figure 2.9 A and B indicate a low total risk and minimal potential risk of Ni and Cr release for WOL, QTZ, VSD T3, and VSD T5. However, other feedstocks indicate more concerning risks for the release of these elements like MKM, OLI, DIV, and GK, in some instances. Most kimberlites fall within the same range in Figure 2.9 A and B, yet both VSD samples consistently contain and release less Ni and Cr. In the non-kimberlite feedstocks, OLI and MKM show the highest total

concentration and release for Ni, with OLIs potential to release the element not being met due to low reactivity and surface area (Fig. 2.9A).

The average Ni and Cr concentrations of kimberlites (n=89) found in the Geochemistry of Rocks of the Oceans and Continents (GEOROC) database show that this study's kimberlites are lower than the average Ni concentration, yet within the standard deviation (Fig. 2.10), indicating that these kimberlites are not outliers, and that the average kimberlite likely does not pose a significant risk of Ni release. Similarly, all kimberlites analyzed in this study are within the GEOROC database standard deviation for Cr concentration, despite being slightly higher than the average (Fig. 2.10). Placing our samples in the context of a more extensive database allows for judgements to be made about the potential element release from specific rock types. Our leach tests provide a unique opportunity to emulate this form of large-scale data sharing and create a database that would compile leaching data from various rock types, allowing for more well-informed decisions to be made regarding the investigation and deployment of feedstocks.

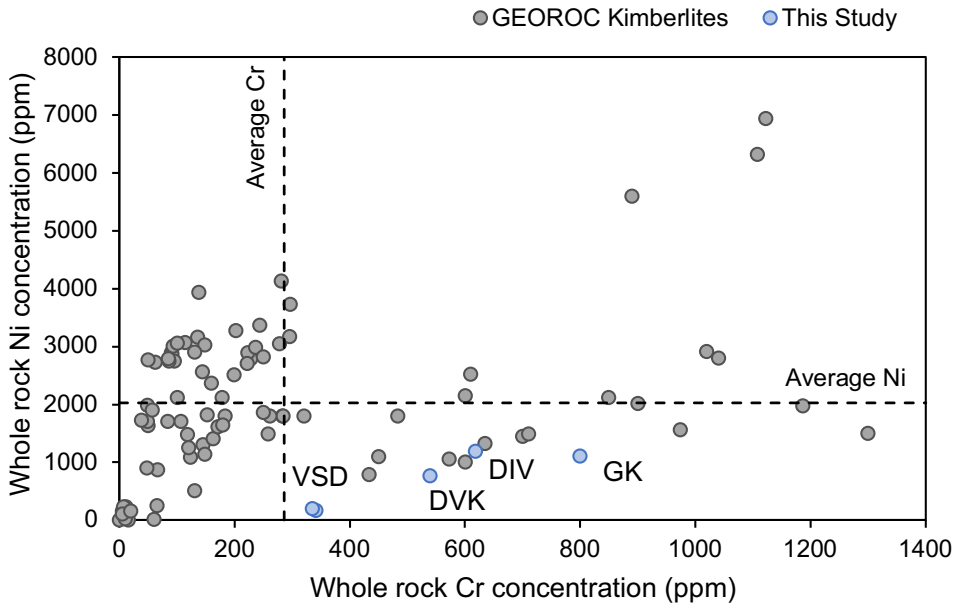

Figure 2.10. Concentration of Ni and Cr found in the whole rock geochemistry of kimberlite samples in the GEOROC database and their averages (n=88), and the concentration of each element found in our kimberlites.

Ultramafic minerals like olivine are the most studied feedstock for the release of Ni and Cr (Beerling et al., 2018; Haque et al., 2020; ten Berge et al., 2012). The high concentrations of these elements in olivine, which has a relatively fast dissolution rate poses a risk of adverse environmental effects. Studies of deleterious metal release from ERW feedstocks have primarily focused on laboratory experiments, with minimal field trials, likely due in part to the risk associated with an experimental design that involves amending soils with a material that has an unknown capacity to release potentially harmful metals. Our leach test can be used for preliminary testing of a feedstock's suitability for such field trials, by exposing these materials to accelerated natural weathering that overestimates the release of Ni and Cr, providing the confidence for deployment.

Mitigating Ni and Cr contamination risks may become necessary in soils where ERW feedstocks are applied (Vasiluk et al., 2019). Hyperaccumulating plants have been proposed as a method for removing Ni from these soils, offering the co-benefits of biomass for energy production and subsequent creation of Ni-rich ash which can be used as a "bio-ore" (Brooks et al., 1974; Kidd et al., 2018). As a result, this method can be an attractive option for sustainable recovery of Ni from mine wastes, such as those of the Mount Keith mine, offering a financial incentive for deploying ERW practices.

When the application of feedstocks off-site is required, the rate at which this is done must be considered. Equation 2.3 is used to manage the release of labile Ni and Cr by determining safe rates for feedstock application (Haque et al., 2020):

$$Rate\ of\ application\ (\frac{t}{ha}) = \frac{Critical\ value\ for\ element\ \times\ \rho_s\ \times\ D_{accumulation}}{Total\ extractable\ concentraion\ of\ element} \qquad (2.3)$$

where ρ_s is the density (g/cm^3) of the soils, and $D_{accumulation}$ is the depth of accumulation. Haque et al. (2020) found application rates for olivine containing 3 g Ni/kg and 150 mg Cr/kg to be 112.5 t/ha and 3,200 t/ha, respectively. The rate of application becomes more appropriate for a given deployment site as the density of the soils and accumulation depth are considered. Moreover, our leaches allow quantification of the denominator of this calculation, based on what is easily released, leading to more accurate determinations of application rates. This equation and others like it allow for a higher level of decision making for the application of ERW feedstocks to arable land, yet it emphasizes the importance of considering the characteristics of the application site.

Our leach tests can be used to assess the release of Ni, Cr, and other deleterious elements during ERW applications; however, environmental conditions that are not

accounted for in these leaches must also be considered on a case-by-case basis. For example, the soils to which these feedstocks are applied will affect the bioavailability of Ni and Cr based mainly on their pH, redox, and other parameters, including organic matter, cation exchange capacity, and physical attributes (Smolders et al., 2009; Soubrand-Colin et al., 2007). Moreover, organic matter can adsorb Ni via its precipitation as sulfides when sediments provide reducing conditions (Kabata-Pendias, 2000). The distribution of Ni throughout a soil profile is largely governed by this organic matter, but has also shown relations to amorphous oxides (chiefly MnO and FeO), and clay fractions (Kabata-Pendias, 2000). Similarly, the mobility and solubility of Cr is largely governed by the same parameters as Ni, but with notable differences observed between behaviours of its different redox states (from +2 to +6). Additionally, changes to soil parameters like pH and redox conditions may result in once immobile Ni and Cr becoming liberated over time (McClain and Maher, 2016). Consequently, multi-annual studies are required to observe the long-term effects on different types of crops and soils (ten Berge et al., 2012). Thus, while the results of this leach test show that some feedstocks will have insignificant risk of Ni and Cr release (VSD T3, VSD T5, WOL), even feedstocks that release moderate amounts of deleterious metals may find an application in an environment tailored towards the mitigation of their release.

2.4.4 Nutrients

Amending soils with rocks and minerals is a proven method of supplying essential macronutrients, chiefly P, K, Ca, Mg, and Si, to depleted soils (Anda et al., 2015, 2013b; Beerling et al., 2018; Van Straaten, 2006). The use of rock-based amendments in

conjunction with traditional nutrient delivery practices has the potential to offset the use of fertilizers, leading to reduced operating costs, while providing the co-benefit of CO_2 sequestration. Success of small-scale trials in the tropical soils of Africa, Brazil, Malaysia, and Mauritius indicate a positive outlook for large-scale deployment (Beerling et al., 2018). Consequently, a high level of confidence is needed before proceeding with the widespread application of these feedstocks. The batch leaching tests in this study can be used to rapidly estimate nutrient release prior to applying rock powders.

The release of P was significantly less than that of K in all feedstocks, which can be attributed to their geochemical concentrations being separated by nearly one order of magnitude. Mineral phases that contain P were not detected using XRD, suggesting mineral abundances were too low. Minerals containing K include microcline, muscovite, phlogopite, and orthoclase, found predominantly in these kimberlites, suggesting their presence as a target for selection of amendments. The proportions of P and K released were quite low, yet their potential for release based on the geochemistry of these samples is high. The P released relative to the total P in the feedstocks shows that both VSD samples perform the best compared to the other kimberlites (Fig. 2.11A). The only non-kimberlite feedstock with any significant release of P was MBA, and while WOL released small amounts, its total concentration is low, which indicates limited long-term potential as a slow-release fertilizer. Similarly, for K, where kimberlites yielded the most release relative to their total concentration, VSD samples indicate the most potential followed by GK then DVK, with DIV showing the least. (Fig. 2.11B).

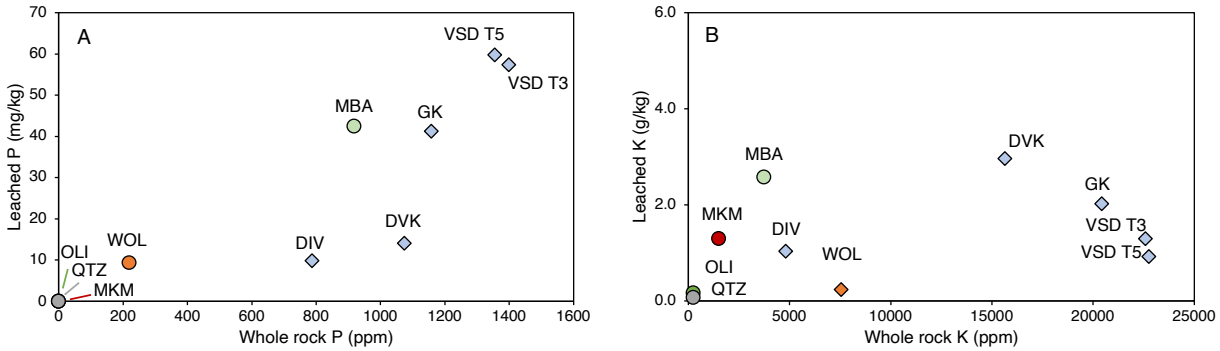

Figure 2.11. The concentrations of P (A) and K (B) that comprise the geochemistry of each feedstock plotted against the amount of each element released during the leaches, indicating the feedstock's ability to provide the nutrients that they contain.

The concentrations of P and K in kimberlites listed in the GEOROC database range from ~2,100–45,000 ppm and ~100–65,700 ppm, respectively (n=1830). All kimberlite samples analyzed in this study are within the ranges observed in the database. Although, all kimberlites analyzed in this study fall below the average P concentration found in the database (Fig. 2.12A), while far exceeding the average K concentration (Fig. 2.12B). This indicates that our kimberlites have a capacity to provide K as a nutrient that is significantly higher than most kimberlites found around the world.

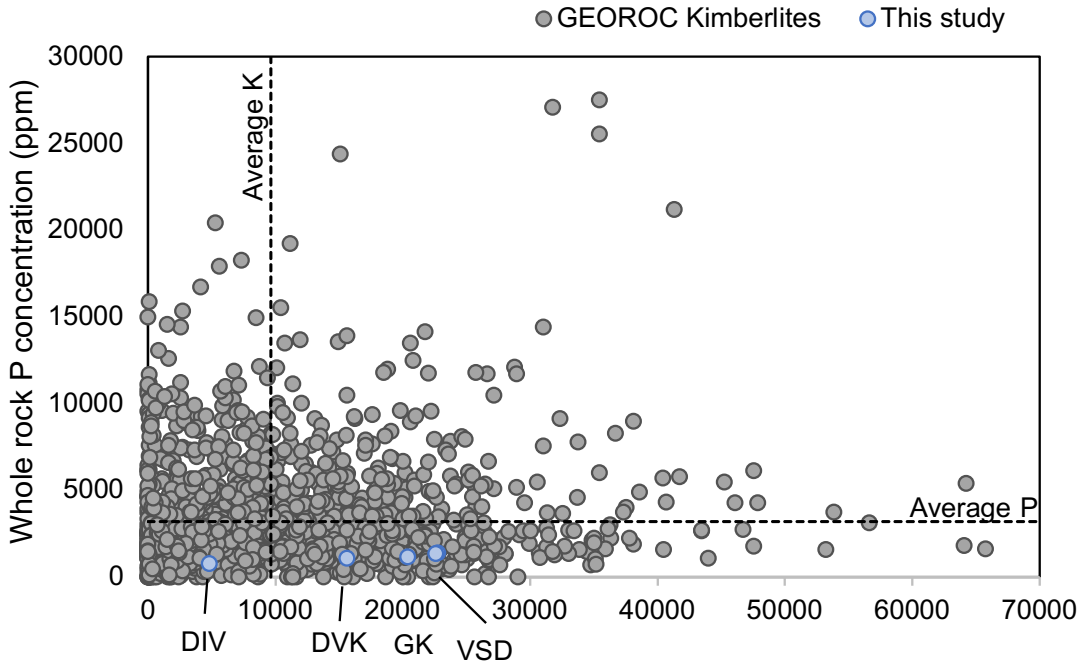

Figure 2.12. Concentration of P and K found in the whole rock geochemistry of kimberlite samples in the GEOROC database and their averages (n=1830), and the concentration of each element found in out kimberlites.

Basalt is the predominant rock studied as an agricultural fertilizer, with studies showing increased crop size and yield (Anda et al., 2013a; Edwards et al., 2017). Thus, research trials using other ERW feedstocks as potential fertilizers is warranted. Haque et al. (2019) studied the effects of wollastonite applications to beans and corn, resulting in a 117% and 90% increase in plant biomass, respectively. The wollastonite used by Haque et al. (2019) is sourced from the same mine as our WOL sample, which released comparatively insignificant amounts of P and K, indicating that perhaps a larger focus should be placed on the release of Ca and Si as macronutrients for plant growth. Si released via rock weathering is consumed as silicic acid by many crops, providing resistance to pests and disease, and increasing water efficiency by lowering leaf

transpiration rates (Keeping et al., 2014; Najihah et al., 2015), with the potential to improve drought resilience (Hartmann et al., 2013). Additionally, acidification of arable soils is a global concern, with approximately 30% of global soils having pH values <5.5 (Kantola et al., 2017), which can be reversed through the addition alkaline rock powders, benefiting nutrient uptake, root growth, and crop yield (Beerling et al., 2018). The ability of these feedstocks to buffer carbonic acid can be seen in the difference between the starting pH of the leachate and its final value. All samples started at a pH of 3.9 (deionized water equilibrated with pure CO_2), which was buffered to pH ~5.5 for all kimberlites, WOL, and MKM. The only feedstock that did not display this level of buffering was OLI, which had a final pH of 4.4. Not only does alkaline leachate contribute to buffering soil acidity it has also been suggested that it can lead to a decrease in cropland N_2O emissions (Islam et al., 2006; Nunes et al., 2014; Shaaban et al., 2014) and reduce the mobility of potentially deleterious metals and metalloids. The application of select feedstocks investigated in this study can benefit crop production and, ultimately, food and soil security.

Of the feedstocks investigated in this study, olivine and wollastonite have received the most attention as potential rock-based agricultural fertilizers (Amann et al., 2020; Anda et al., 2015, 2013a; Dietzen et al., 2018; Haque et al., 2020c, 2019; L. L. Taylor et al., 2021). One factor limiting the appeal of these feedstocks is their associated costs. This includes the transport, milling, and application, which all incur financial and environmental costs (Andrews and Taylor, 2019). Moosdorf et al. (2014) suggest that the transportation of feedstocks could emit 4% of the total CO_2 sequestered while grinding and processing could offset up to 25%. Mine wastes often do not require additional

grinding, which would hinder their total CO_2 sequestration capacity, yet have garnered comparatively little attention as potential rock-based agricultural fertilizers. Barriers to the off-site application of mine residues like the kimberlite used in this study, the Mount Keith tailings, and others include regulations governing the management of mine wastes, concerns over selling unrecovered ore at a potential loss, the distribution of indicator minerals, and public perception (Krüger, 2007). Another consideration for extensive applications of rock powder includes altering the permeability of the soil as a result of accumulated slower weathering phases, which can lead to restriction of particle movement or particle loss via overland flow (Andrews and Taylor, 2019).

2.4.5 *Feedstock comparison and implications*

The leaching test employed in our study is most useful for comparing the (1) CO_2 sequestration potential and capacity, (2) release of deleterious elements, and (3) release of nutrients (Table 2.7; 2.8). For these categories, feedstocks were assigned relative grades of + (low), ++ (moderate), and +++ (highest rank) comparisons. No kimberlites received the highest rating for CO_2 sequestration potential, yet GK and DIV were given the highest grade possible for their capacity.

Despite high capacities observed in GK, DVK and DIV, the sequestration potentials remain low due to the lack of reactivity from these feedstocks (Table 2.7). The release of deleterious metals from kimberlites was considerably low in both VSD samples and DVK, thus earning them the highest rating for this category. In contrast, GK and DIV released comparatively high amounts of Ni and Cr, resulting in lower ratings for these two feedstocks. GK, VSD T3, and VSD T5 received the highest grade for the release of P

and K based mainly on their high release of P which was not observed in the lowest ranked DVK and DIV.

Consequently, recommendations can be made that encapsulate these results. For GK, it is recommended that alterations be made to storage practices to improve Mg release in addition to limiting or further investigating offsite applications due to Ni and Cr release. The poor results of DVK emphasized by the low P/K release suggest limited benefits for most applications, despite the low release of deleterious metals. Both VSD samples display exceptionally low releases of Ni and Cr, coupled with higher-than-average release of P and K. However, they are limited by a lack of CO_2 sequestration potential. Finally, DIV displayed adequate CO_2 sequestration capacity and potential, but due to its limited P/K release and very high release of Ni and Cr, cannot be recommended for any use outside of engineered environments.

Exceptional CO_2 sequestration capacity and potential was displayed in WOL, earning this feedstock the highest grade. Additionally, negligible amounts of Ni and Cr and P and K were released during the leaches. Consequently, WOL has a very high upside as an ERW feedstock, yet agricultural applications may be limited, requiring further investigation into the benefits of Si and Ca release. Despite its tremendous capacity for CO_2 sequestration, OLI falls short on potential. The release of Ni and Cr is not of concern in OLI, while negligible amounts of P and K are released. Recommendations for OLI based on these results require further processing of the material to reduce grain size and increase surface area, with the hopes of achieving the feedstock capacity. The MKM sample displayed exceptional CO_2 sequestration capacity and potential, resulting in the highest grade being awarded for both. However, the potential use of MKM mine waste as

a soil amendment is largely compromised by its high release of Ni. Recommendations for MKM include keeping this feedstock on-site in an environment engineered to retain potentially contaminated effluent and facilitate the dissolution of a highly reactive mineral phases. MBA exhibited a middling capacity for CO_2 sequestration yet had a potential that rivalled WOL, resulting in high grades for this feedstock. Minimal release of Ni and Cr was observed while releasing the highest amount of P and K. As a result, MBA is very well suited for deployment in agricultural settings. However, a high degree of monitoring is recommended to determine when the low capacity is met (Table 2.8).

Enhanced rock weathering of alkaline mineral feedstocks is a NET with a large capacity for CO_2 sequestration. Coupling rapid leach tests with standard characterization, including mineralogy, geochemistry, surface area, and TIC allows predictions about how this capacity will be met. Implementation of these methodologies can result in higher accuracy in the initial stages of ERW deployment and increased future success. The mineralogical composition of the feedstocks analyzed significantly impacted their leaching performance. As a result, the importance of highly reactive phases like brucite and wollastonite, which yielded the highest release of their major cations, is emphasized, thus, translating to comparatively high CO_2 sequestration potentials for MKM and WOL. Particle size and surface area also played a significant role, with coarser samples like OLI releasing very small proportions of Mg, which constitutes over half of the sample's geochemistry, leading to very low CO_2 sequestration potential compared to its capacity.

The release of deleterious metals like Ni and Cr from a given feedstock is an important consideration prior to large-scale deployment. We see small proportions of the total Ni and Cr contained in all feedstocks released during this leach, indicating an

insignificant potential for soil contamination at the dispersal sites. However, further investigation into the extent of Ni and Cr accumulation is required individually based on the soil in which these feedstocks are being applied and the effect it may have on the broader environment.

Feedstocks that contain relatively high concentrations of P and K and have the potential to provide these nutrients as a co-benefit to soils and vegetation when applied in an agricultural setting. The release of P from all feedstocks was low (<60 mg/kg), however, K was released at much higher proportions, with most values between 1–3 g/kg. Kimberlite residues typically displayed the highest release of both elements, but this co-benefit could be hindered by the barriers preventing its offsite application. MBA was the only other feedstock to have significant contributions. Nutrient release from olivine and wollastonite was ostensibly non-existent, despite studies detailing their positive effect on plant growth.

Table 2.7. Summary of the key results from the kimberlite leaching tests. Each feedstock has been given a relative grade on their use for CO_2 sequestration, release of elements of concern (EOC), and elements of interest (EOI). Three grade levels are employed, with "+" representing the worst, and "+ + +" representing the best.

	CO_2 sequestration (kg CO_2/t)				**Elements of concern (mg/kg)**			**Elements of interest**			**Recommendations**
Sample	**Capacity**	**Grade**	**Potential**	**Grade**	**Ni**	**Cr**	**Grade**	**P (mg/kg)**	**K (g/kg)**	**Grade**	
GK	318	+++	11	+ +	77	0.1	+ +	41	2	+ + +	On-site enhancements to improve Mg release and sequestration (seq.) potential. Ni and Cr may limit off-site applications, despite high P and K release.
DVK	244	++	4	+	45	0.1	+ + +	14	3	+	Low potential for seq. and insignificant P and K limits off-site applicability.
VSD T3	133	+	1	+	1	0	+ + +	57	1	+ + +	Exceptional P release with negligible Ni and Cr. Off-site deployment is recommended but is hindered by low seq. potential.
VSD T5	128	+	12	+ +	2	0	+ + +	60	1	+ + +	Exceptional P release with negligible Ni and Cr. Off-site deployment recommended but is hindered by low seq. potential.
DIV	360	+++	11	+ +	290	0.2	+	10	1	+	Adequate seq. potential, with promising Si weathering. Concerning Ni release and insignificant P and K require on-site applications

Table 2.8. Summary table of key results of kimberlites used in Chapter 2. Each feedstock has been given a grade based on their results for the parameters of CO_2 sequestration, elements of concern (EOC), and elements of interest (EOI). Three grade levels are employed, with "+" representing the worst, and "+ + +" representing the best.

	CO_2 sequestration (kg CO_2/t)				**Elements of concern (mg/kg)**			**Elements of interest**			**Recommendations**
Sample	**Capacity**	**Grade**	**Potential**	**Grade**	**Ni**	**Cr**	**Grade**	**P (mg/kg)**	**K (g/kg)**	**Grade**	
WOL	261	+++	25	+ + +	1	0.1	+ + +	10	0.2	+	Excellent sequestration (seq.) potential, with minimal release of EOC. Lack of P and K limit Ag. suitability. Alternative applications may apply.
OLI	545	+++	4	+	26	0.5	+ +	0	0.1	+	High seq. capacity is not reflected in seq. potential. Physical alterations required to make meaningful impact. Ag. benefit-non-existent. Highest Cr release observed, with little Ni.
QTZ	4	n/a	0	n/a	0.8	0	n/a	0	0.1	n/a	Control material.
MKM	420	+++	46	+ + +	682	0	+	0	1	+	Exceptional potential for CO_2 seq. High Ni and insignificant P and K release inhibit ag. suitability. On-site enhancements recommended to facilitate seq.
MBA	167	++	20	+ + +	5	0.3	+ +	42	2.5	+ + +	High seq. potential, high P and K release, low Ni but comparatively high Cr. Off-site/ag. deployment paired with a high degree of monitoring recommended.

2.5 Conclusion

In addition to characterizing ERW feedstocks' mineralogical, geochemical, and physical properties, batch dissolution analyses should be used to evaluate reactivity, mineral dissolution, cation release and sources. The reactivity tests in this study are an assessment tool designed to quantify the release of easily extractable cations from non-carbonate sources and provide a prediction of CO_2 sequestration potential for a mineralogically complex feedstock. Applying this tool to ERW development allows for a higher confidence level in decision-making for feedstock selection, based mainly on the differentiation between carbonate (undesirable) and non-carbonate (desirable) sources of cations. Furthermore, this tool allows for the determination of easily released contaminants (e.g., Ni, Cr) or nutrients (e.g., P, K), which sets this leach test apart, allowing for more considerations during the feedstock selection process for ERW.

While our reactivity tests are useful for evaluating ERW feedstocks, there are limitations to consider. One challenge is the heterogeneity of complex feedstocks, (e.g., kimberlite residues), which is exacerbated when using small sample masses, (e.g., 250 mg,) for tests in this study. Furthermore, the fate of weathering products in the environment, specifically the effects of Ni and Cr requires field trials. Moreover, the timeframe at which reactions outlined in this study will occur cannot be confirmed, leading to uncertainties regarding the pace at which the CO_2 sequestration potential will be met.

The results of this study provide insight into which feedstocks can be expected to sequester the most CO_2, while the release of Ni, Cr and P, K informs potential deployment sites. Off-site application of mine residues like DIV and MKM, which

released the most Ni per mass, may not be a best practice. However, DIV, MKM, and similar feedstocks may not require an off-site application. Most mine residues have already been processed and deposited in storage facilities, often designed to mitigate the release of potentially harmful elements into the broader environment, making this an ideal target location for ERW. In contrast, the release of P and K measured through the leaches provide insight into these feedstocks potential uses as rock-based agricultural amendments.

2.6. References

Amann, T., Hartmann, J., Hellmann, R., Trindade Pendrosa, E., Malik, A., 2022. Enhanced weathering potentials — the role of in situ CO_2 and grain size distribution. Front. Clim.

Amann, T., Hartmann, J., Struyf, E., De Oliveira Garcia, W., Fischer, E.K., Janssens, I., Meire, P., Schoelynck, J., 2020. Enhanced Weathering and related element fluxes - A cropland mesocosm approach. Biogeosciences 17, 103–119. https://doi.org/10.5194/bg-17-103-2020

Anda, M., Shamshuddin, J., Fauziah, C.I., 2015. Improving chemical properties of a highly weathered soil using finely ground basalt rocks. Catena 124, 147–161. https://doi.org/10.1016/j.catena.2014.09.012

Anda, M., Shamshuddin, J., Fauziah, C.I., 2013a. Increasing negative charge and nutrient contents of a highly weathered soil using basalt and rice husk to promote cocoa growth under field conditions. Soil Tillage Res. 132, 1–11. https://doi.org/10.1016/j.still.2013.04.005

Anda, M., Shamshuddin, J., Fauziah, C.I., 2013b. Increasing negative charge and nutrient contents of a highly weathered soil using basalt and rice husk to promote cocoa growth under field conditions. Soil Tillage Res. 132, 1–11. https://doi.org/10.1016/j.still.2013.04.005

Andrews, M.G., Taylor, L.L., 2019. Combating Climate Change Through Enhanced Weathering of Agricultural Soils. Elements 15, 253–258. https://doi.org/10.2138/gselements.15.4.253

Assima, G.P., Larachi, F., Molson, J., Beaudoin, G., 2014. New tools for stimulating

dissolution and carbonation of ultramafic mining residues. Can. J. Chem. Eng. https://doi.org/10.1002/cjce.22066

Beerling, D.J., Leake, J.R., Long, S.P., Scholes, J.D., Ton, J., Nelson, P.N., Bird, M., Kantzas, E., Taylor, L.L., Sarkar, B., Kelland, M., DeLucia, E., Kantola, I., Müller, C., Rau, G., Hansen, J., 2018. Farming with crops and rocks to address global climate, food and soil security /631/449 /706/1143 /704/47 /704/106 perspective. Nat. Plants 4, 138–147. https://doi.org/10.1038/s41477-018-0108-y

Beuttler, C., Charles, L., Wurzbacher, J., 2019. The Role of Direct Air Capture in Mitigation of Anthropogenic Greenhouse Gas Emissions. Front. Clim. 1, 1–7. https://doi.org/10.3389/fclim.2019.00010

Brooks, R., Lee, J., Jaffre, T., 1974. Some New Zealand and New Caledonian plant accumulators of nickel. JournalofEcology 62: 493–499.

Daval, D., Hellmann, R., Martinez, I., Gangloff, S., Guyot, F., 2013. Lizardite serpentine dissolution kinetics as a function of pH and temperature, including effects of elevated pCO_2. Chem. Geol. https://doi.org/10.1016/j.chemgeo.2013.05.020

Di Lorenzo, F., Ruiz-Agudo, C., Ibañez-Velasco, A., Gil-San Millán, R., Navarro, J.A.R., Ruiz-Agudo, E., Rodriguez-Navarro, C., 2018. The carbonation of wollastonite: A model reaction to test natural and biomimetic catalysts for enhanced CO_2 sequestration. Minerals. https://doi.org/10.3390/min8050209

Dietzen, C., Harrison, R., Michelsen-Correa, S., 2018. Effectiveness of enhanced mineral weathering as a carbon sequestration tool and alternative to agricultural lime: An incubation experiment. Int. J. Greenh. Gas Control 74, 251–258. https://doi.org/10.1016/j.ijggc.2018.05.007

Drever, J.I., 2005. Surface and Ground Water, Weathering, and Soils, 5th ed. Treatise on Geochemistry.

Edwards, D.P., Lim, F., James, R.H., Pearce, C.R., Scholes, J., Freckleton, R.P., Beerling, D.J., 2017. Climate change mitigation: Potential benefits and pitfalls of enhanced rock weathering in tropical agriculture. Biol. Lett. 13. https://doi.org/10.1098/rsbl.2016.0715

Entezari Zarandi, A., Larachi, F., Beaudoin, G., Plante, B., Sciortino, M., 2016. Multivariate study of the dynamics of CO_2 reaction with brucite-rich ultramafic mine tailings. Int. J. Greenh. Gas Control 52, 110–119. https://doi.org/10.1016/j.ijggc.2016.06.022

Hamilton, J.L., Wilson, S.A., Turvey, C.C., Morgan, B., Tait, A.W., McCutcheon, J., Fallon, S.J., Southam, G., 2021. Carbon accounting of mined landscapes, and deployment of a geochemical treatment system for enhanced weathering at Woodsreef Chrysotile Mine, NSW, Australia. J. Geochemical Explor. 220. https://doi.org/10.1016/j.gexplo.2020.106655

Hänchen, M., Prigiobbe, V., Baciocchi, R., Mazzotti, M., 2008. Precipitation in the Mg-carbonate system-effects of temperature and CO_2 pressure. Chem. Eng. Sci. 63, 1012–1028. https://doi.org/10.1016/j.ces.2007.09.052

Hangx, S.J.T., Spiers, C.J., 2009. Coastal spreading of olivine to control atmospheric CO_2 concentrations: A critical analysis of viability. Int. J. Greenh. Gas Control 3, 757–767. https://doi.org/10.1016/j.ijggc.2009.07.001

Haque, F., Chiang, Y.W., Santos, R.M., 2020a. Risk assessment of Ni, Cr, and Si release from alkaline minerals during enhanced weathering. Open Agric. 5, 166–175.

https://doi.org/10.1515/opag-2020-0016

Haque, F., Santos, R.M., Chiang, Y.W., 2020b. CO_2 sequestration by wollastonite-amended agricultural soils – An Ontario field study. Int. J. Greenh. Gas Control 97, 103017. https://doi.org/10.1016/j.ijggc.2020.103017

Haque, F., Santos, R.M., Chiang, Y.W., 2020c. CO_2 sequestration by wollastonite-amended agricultural soils – An Ontario field study. Int. J. Greenh. Gas Control. https://doi.org/10.1016/j.ijggc.2020.103017

Haque, F., Santos, R.M., Dutta, A., Thimmanagari, M., Chiang, Y.W., 2019. Co-Benefits of Wollastonite Weathering in Agriculture: CO_2 Sequestration and Promoted Plant Growth. ACS Omega 4, 1425–1433. https://doi.org/10.1021/acsomega.8b02477

Harrison, A.L., Dipple, G.M., Power, I.M., Mayer, K.U., 2015. Influence of surface passivation and water content on mineral reactions in unsaturated porous media: Implications for brucite carbonation and CO_2 sequestration. Geochim. Cosmochim. Acta 148, 477–495. https://doi.org/10.1016/j.gca.2014.10.020

Harrison, A.L., Power, I.M., Dipple, G.M., 2013. Accelerated carbonation of brucite in mine tailings for carbon sequestration. Environ. Sci. Technol. https://doi.org/10.1021/es3012854

Hartmann, J., West, A.J., Renforth, P., Köhler, P., De La Rocha, C.L., Wolf-Gladrow, D.A., Dürr, H.H., Scheffran, J., 2013. Enhanced chemical weathering as a geoengineering strategy to reduce atmospheric carbon dioxide, supply nutrients, and mitigate ocean acidification. Rev. Geophys. https://doi.org/10.1002/rog.20004

Hövelmann, J., Putnis, C. V., Ruiz-Agudo, E., Austrheim, H., 2012. Direct nanoscale observations of CO_2 sequestration during brucite [Mg(OH)2] dissolution. Environ.

Sci. Technol. 46, 5253–5260. https://doi.org/10.1021/es300403n

Huijgen, W.J.J., Witkamp, G.J., Comans, R.N.J., 2006. Mechanisms of aqueous wollastonite carbonation as a possible CO_2 sequestration process. Chem. Eng. Sci. 61, 4242–4251. https://doi.org/10.1016/j.ces.2006.01.048

Islam, A., White, R.E., Chen, D., 2006. Nitrification activity in acid soils of north-eastern Victoria, Australia, as affected by liming and phosphorus fertilisation. Aust. J. Soil Res. 44, 739–744. https://doi.org/10.1071/SR06058

Kabata-Pendias, A., 2010. Trace elements in soils and plants: Fourth edition, Trace Elements in Soils and Plants, Fourth Edition. https://doi.org/10.1201/b10158

Kabata-Pendias, A., 2000. Trace Elements in Soils and Plants, 3rd ed. CRC Press. https://doi.org/10.1136/bmj.2.4640.1355-a

Kantola, I.B., Masters, M.D., Beerling, D.J., Long, S.P., DeLucia, E.H., 2017. Potential of global croplands and bioenergy crops for climate change mitigation through deployment for enhanced weathering. Biol. Lett. 13. https://doi.org/10.1098/rsbl.2016.0714

Keeping, M.G., Miles, N., Sewpersad, C., 2014. Silicon reduces impact of plant nitrogen in promoting stalk borer (Eldana saccharina) but not sugarcane thrips (fulmekiola serrata) infestations in sugarcane. Front. Plant Sci. 5, 1–12. https://doi.org/10.3389/fpls.2014.00289

Kidd, P.S., Bani, A., Benizri, E., Gonnelli, C., Hazotte, C., Kisser, J., Konstantinou, M., Kuppens, T., Kyrkas, D., Laubie, B., Malina, R., Morel, J.L., Olcay, H., Pardo, T., Pons, M.N., Prieto-Fernández, Á., Puschenreiter, M., Quintela-Sabarís, C., Ridard, C., Rodríguez-Garrido, B., Rosenkranz, T., Rozpadek, P., Saad, R., Selvi, F.,

Simonnot, M.O., Tognacchini, A., Turnau, K., Wazny, R., Witters, N., Echevarria, G., 2018. Developing sustainable agromining systems in agricultural ultramafic soils for nickel recovery. Front. Environ. Sci. 6, 1–20. https://doi.org/10.3389/fenvs.2018.00044

Knauss, K.G., Nguyen, S.N., Weed, H.C., 1993. Diopside dissolution kinetics as a function of pH, CO2, temperature, and time. Geochim. Cosmochim. Acta 57, 285–294. https://doi.org/10.1016/0016-7037(93)90431-U

Komadel, P., 2003. Chemically modified smectites. Clay Miner. 38, 127–138. https://doi.org/10.1180/0009855033810083

Krüger, L., 2007. Technical Note TN 2007-07-01 KIMBERLITE AS LOW GRADE FERTILIZER - A REVIEW 1–20.

Langmuir, D., 1997. Aqueous Environmental Geochemistry. Geochemistry Prentice Hall: Upper Saddle River.

Lechat, K., Lemieux, J.M., Molson, J., Beaudoin, G., Hébert, R., 2016. Field evidence of CO2 sequestration by mineral carbonation in ultramafic milling wastes, Thetford Mines, Canada. Int. J. Greenh. Gas Control 47, 110–121. https://doi.org/10.1016/j.ijggc.2016.01.036

Lefebvre, D., Goglio, P., Williams, A., Manning, D.A.C., de Azevedo, A.C., Bergmann, M., Meersmans, J., Smith, P., 2019. Assessing the potential of soil carbonation and enhanced weathering through Life Cycle Assessment: A case study for Sao Paulo State, Brazil. J. Clean. Prod. 233, 468–481. https://doi.org/10.1016/j.jclepro.2019.06.099

Li, J., Hitch, M., Power, I.M., Pan, Y., 2018. Integrated mineral carbonation of ultramafic

mine deposits—A review. Minerals 8. https://doi.org/10.3390/min8040147

McClain, C.N., Maher, K., 2016. Chromium fluxes and speciation in ultramafic catchments and global rivers. Chem. Geol. 426, 135–157. https://doi.org/10.1016/j.chemgeo.2016.01.021

Mehta, N., Cocerva, T., Cipullo, S., Padoan, E., Dino, G.A., Ajmone-Marsan, F., Cox, S.F., Coulon, F., De Luca, D.A., 2019. Linking oral bioaccessibility and solid phase distribution of potentially toxic elements in extractive waste and soil from an abandoned mine site: Case study in Campello Monti, NW Italy. Sci. Total Environ. 651, 2799–2810. https://doi.org/10.1016/j.scitotenv.2018.10.115

Mervine, E.M., Wilson, S.A., Power, I.M., Dipple, G.M., Turvey, C.C., Hamilton, J.L., Vanderzee, S., Raudsepp, M., Southam, C., Matter, J.M., Kelemen, P.B., Stiefenhofer, J., Miya, Z., Southam, G., 2018. Potential for offsetting diamond mine carbon emissions through mineral carbonation of processed kimberlite: an assessment of De Beers mine sites in South Africa and Canada. Mineral. Petrol. 112, 755–765. https://doi.org/10.1007/s00710-018-0589-4

Meysman, F.J.R., Montserrat, F., 2017. Negative CO_2 emissions via enhanced silicate weathering in coastal environments. Biol. Lett. 13. https://doi.org/10.1098/rsbl.2016.0905

Mills, S.J., Whitfield, P.S., Wilson, S.A., Woodhouse, J.N., Dipple, G.M., Raudsepp, M., Francis, C.A., 2011. The crystal structure of stichtite, re-examination of barbertonite, and the nature of polytypism in MgCr hydrotalcites. Am. Mineral. 96, 179–187. https://doi.org/10.2138/am.2011.3531

Minx, J.C., Lamb, W.F., Callaghan, M.W., Fuss, S., Hilaire, J., Creutzig, F., Amann, T.,

Beringer, T., De Oliveira Garcia, W., Hartmann, J., Khanna, T., Lenzi, D., Luderer, G., Nemet, G.F., Rogelj, J., Smith, P., Vicente Vicente, J.L., Wilcox, J., Del Mar Zamora Dominguez, M., 2018. Negative emissions - Part 1: Research landscape and synthesis. Environ. Res. Lett. 13. https://doi.org/10.1088/1748-9326/aabf9b

Montserrat, F., Renforth, P., Hartmann, J., Leermakers, M., Knops, P., Meysman, F.J.R., 2017. Olivine Dissolution in Seawater: Implications for CO_2 Sequestration through Enhanced Weathering in Coastal Environments. Environ. Sci. Technol. 51, 3960–3972. https://doi.org/10.1021/acs.est.6b05942

Moosdorf, N., Renforth, P., Hartmann, J., 2014. Carbon dioxide efficiency of terrestrial enhanced weathering. Environ. Sci. Technol. 48, 4809–4816. https://doi.org/10.1021/es4052022

Najihah, N.I., Hanafi, M.M., Idris, A.S., Hakim, M.A., 2015. Silicon treatment in oil palms confers resistance to basal stem rot disease caused by Ganoderma boninense. Crop Prot. 67, 151–159. https://doi.org/10.1016/j.cropro.2014.10.004

Nunes, J.M.G., Kautzmann, R.M., Oliveira, C., 2014. Evaluation of the natural fertilizing potential of basalt dust wastes from the mining district of Nova Prata (Brazil). J. Clean. Prod. https://doi.org/10.1016/j.jclepro.2014.04.032

Oelkers, E.H., Declercq, J., Saldi, G.D., Gislason, S.R., Schott, J., 2018. Olivine dissolution rates: A critical review. Chem. Geol. https://doi.org/10.1016/j.chemgeo.2018.10.008

Oelkers, E.H., Gislason, S.R., Matter, J., 2008. Mineral carbonation of CO_2. Elements. https://doi.org/10.2113/gselements.4.5.333

Paulo, C., Power, I.M., Stubbs, A.R., Wang, B., Zeyen, N., Wilson, S.A., 2021.

Evaluating feedstocks for carbon dioxide removal by enhanced rock weathering and CO_2 mineralization. Appl. Geochemistry 129, 104955. https://doi.org/10.1016/j.apgeochem.2021.104955

Pokrovsky, O.S., Schott, J., 2004. Experimental study of brucite dissolution and precipitation in aqueous solutions: Surface speciation and chemical affinity control. Geochim. Cosmochim. Acta 68, 31–45. https://doi.org/10.1016/S0016-7037(03)00238-2

Power, I.M., Dipple, G.M., Bradshaw, P.M.D., Harrison, A.L., 2020. Prospects for CO_2 mineralization and enhanced weathering of ultramafic mine tailings from the Baptiste nickel deposit in British Columbia, Canada. Int. J. Greenh. Gas Control 94, 102895. https://doi.org/10.1016/j.ijggc.2019.102895

Power, I.M., Dipple, G.M., Southam, G., 2010. Bioleaching of ultramafic tailings by Acidithiobacillus spp. for CO_2 sequestration. Environ. Sci. Technol. https://doi.org/10.1021/es900986n

Power, I.M., Harrison, A.L., Dipple, G.M., Wilson, S.A., Kelemen, P.B., Hitch, M., Southam, G., 2013. Carbon mineralization: From natural analogues to engineered systems. Rev. Mineral. Geochemistry 77, 305–360. https://doi.org/10.2138/rmg.2013.77.9

Power, I.M., McCutcheon, J., Harrison, A.L., Wilson, S.A., Dipple, G.M., Kelly, S., Southam, C., Southam, G., 2014. Strategizing carbon-neutral mines: A case for pilot projects, Minerals. https://doi.org/10.3390/min4020399

Power, I.M., Wilson, S.A., Thom, J.M., Dipple, G.M., Gabites, J.E., Southam, G., 2009. The hydromagnesite playas of Atlin, British Columbia, Canada: A biogeochemical

model for CO_2 sequestration. Chem. Geol. 260, 286–300. https://doi.org/10.1016/j.chemgeo.2009.01.012

Renforth, P., 2012. The potential of enhanced weathering in the UK. Int. J. Greenh. Gas Control 10, 229–243. https://doi.org/10.1016/j.ijggc.2012.06.011

Renforth, P., Pogge von Strandmann, P.A.E., Henderson, G.M., 2015. The dissolution of olivine added to soil: Implications for enhanced weathering. Appl. Geochemistry. https://doi.org/10.1016/j.apgeochem.2015.05.016

Rinder, T., von Hagke, C., 2021. The influence of particle size on the potential of enhanced basalt weathering for carbon dioxide removal - Insights from a regional assessment. J. Clean. Prod. 315. https://doi.org/10.1016/j.jclepro.2021.128178

Sanderson, B.M., O'Neill, B.C., Tebaldi, C., 2016. What would it take to achieve the Paris temperature targets? Geophys. Res. Lett. 43, 7133–7142. https://doi.org/10.1002/2016GL069563

Schott, J., Pokrovsky, O.S., Oelkers, E.H., 2009. The link between mineral dissolution/precipitation kinetics and solution chemistry. Rev. Mineral. Geochemistry 70, 207–258. https://doi.org/10.2138/rmg.2009.70.6

Schott, J., Pokrovsky, O.S., Spalla, O., Devreux, F., Gloter, A., Mielczarski, J.A., 2012. Formation, growth and transformation of leached layers during silicate minerals dissolution: The example of wollastonite. Geochim. Cosmochim. Acta 98, 259–281. https://doi.org/10.1016/j.gca.2012.09.030

Senior, G.D., Thomas, S.A., 2005. Development and implementation of a new flowsheet for the flotation of a low grade nickel ore. Int. J. Miner. Process. 78, 49–61. https://doi.org/10.1016/j.minpro.2005.08.001

Shaaban, M., Peng, Q., Lin, S., Wu, Y., Zhao, J., Hu, R., 2014. Nitrous Oxide emission from two acidic soils as affected by dolomite application. Soil Res. 52, 841–848. https://doi.org/10.1071/SR14129

Smolders, E., Oorts, K., Van Sprang, P., Schoeters, I., Janssen, C.R., McGrath, S.P., McLaughlin, M.J., 2009. Toxicity of trace metals in soil as affected by soil type and aging after contamination: Using calibrated bioavailability models to set ecological soil standards. Environ. Toxicol. Chem. 28, 1633–1642. https://doi.org/10.1897/08-592.1

Soubrand-Colin, M., Neel, C., Bril, H., Grosbois, C., Caner, L., 2007. Geochemical behaviour of Ni, Cr, Cu, Zn and Pb in an Andosol-Cambisol climosequence on basaltic rocks in the French Massif Central. Geoderma 137, 340–351. https://doi.org/10.1016/j.geoderma.2006.08.017

Strefler, J., Amann, T., Bauer, N., Kriegler, E., Hartmann, J., 2018. Potential and costs of carbon dioxide removal by enhanced weathering of rocks. Environ. Res. Lett. 13. https://doi.org/10.1088/1748-9326/aaa9c4

Stubbs, A.R., Paulo, C., Power, I.M., Wang, B., Zeyen, N., Wilson, S.A., 2022. Direct measurement of CO_2 drawdown in mine wastes and rock powders: Implications for enhanced rock weathering. Int. J. Greenh. Gas Control 113. https://doi.org/10.1016/j.ijggc.2021.103554

Szramek, K., Walter, L.M., Kanduč, T., Ogrinc, N., 2011. Dolomite Versus Calcite Weathering in Hydrogeochemically Diverse Watersheds Established on Bedded Carbonates (Sava and Soča Rivers, Slovenia). Aquat. Geochemistry 17, 357–396. https://doi.org/10.1007/s10498-011-9125-4

Taylor, L.L., Driscoll, C.T., Groffman, P.M., Rau, G.H., Blum, J.D., Beerling, D.J., 2021. Increased carbon capture by a silicate-treated forested watershed affected by acid deposition. Biogeosciences 18, 169–188. https://doi.org/10.5194/bg-18-169-2021

ten Berge, H.F.M., van der Meer, H.G., Steenhuizen, J.W., Goedhart, P.W., Knops, P., Verhagen, J., 2012. Olivine weathering in soil, and its effects on growth and nutrient uptake in ryegrass (Lolium perenne L.): A pot experiment. PLoS One. https://doi.org/10.1371/journal.pone.0042098

Thom, J.G.M., Dipple, G.M., Power, I.M., Harrison, A.L., 2013a. Chrysotile dissolution rates: Implications for carbon sequestration. Appl. Geochemistry 35, 244–254. https://doi.org/10.1016/j.apgeochem.2013.04.016

Thom, J.G.M., Dipple, G.M., Power, I.M., Harrison, A.L., 2013b. Chrysotile dissolution rates: Implications for carbon sequestration. Appl. Geochemistry. https://doi.org/10.1016/j.apgeochem.2013.04.016

Turvey, C.C., Wilson, S.A., Hamilton, J.L., Tait, A.W., McCutcheon, J., Beinlich, A., Fallon, S.J., Dipple, G.M., Southam, G., 2018. Hydrotalcites and hydrated Mg-carbonates as carbon sinks in serpentinite mineral wastes from the Woodsreef chrysotile mine, New South Wales, Australia: Controls on carbonate mineralogy and efficiency of CO_2 air capture in mine tailings. Int. J. Greenh. Gas Control 79, 38–60. https://doi.org/10.1016/j.ijggc.2018.09.015

Van Straaten, P., 2006. Farming with rocks and minerals: Challenges and opportunities. An. Acad. Bras. Cienc. 78, 731–747. https://doi.org/10.1590/S0001-37652006000400009

Vanderzee, S.S.S., Dipple, G.M., Bradshaw, P.M.D., 2019. Targeting Highly Reactive

Labile Magnesium in Ultramafic Tailings for Greenhouse-Gas Offsets and Potential Tailings Stabilization at the Baptiste Deposit, Central British Columbia (NTS 093K/13, 14). GeoscienceBC 109–118.

Vasiluk, L., Sowa, J., Sanborn, P., Ford, F., Dutton, M.D., Hale, B., 2019. Bioaccessibility estimates by gastric SBRC method to determine relationships to bioavailability of nickel in ultramafic soils. Sci. Total Environ. 673, 685–693. https://doi.org/10.1016/j.scitotenv.2019.04.059

Veetil, S.P., Hitch, M., 2020. Recent developments and challenges of aqueous mineral carbonation: a review. Int. J. Environ. Sci. Technol. 17, 4359–4380. https://doi.org/10.1007/s13762-020-02776-z

Wilson, S.A., Dipple, G.M., Power, I.M., Barker, S.L.L., Fallon, S.J., Southam, G., 2011. Subarctic weathering of mineral wastes provides a sink for atmospheric CO_2. Environ. Sci. Technol. https://doi.org/10.1021/es202112y

Wilson, S.A., Harrison, A.L., Dipple, G.M., Power, I.M., Barker, S.L.L., Ulrich Mayer, K., Fallon, S.J., Raudsepp, M., Southam, G., 2014. Offsetting of CO_2 emissions by air capture in mine tailings at the Mount Keith Nickel Mine, Western Australia: Rates, controls and prospects for carbon neutral mining. Int. J. Greenh. Gas Control 25, 121–140. https://doi.org/10.1016/j.ijggc.2014.04.002

Zeyen, N., Wang, B., Wilson, S.A., Paulo, C., Stubbs, A.R., Power, I.M., Steele-Maclnnis, M., Lanzirotti, A., Newville, M., Paterson, D.J., Hamilton, J.L., Jones, T.R., Turvey, C.C., Dipple, G.M., Southam, G., 2022. Cation Exchange in Smectites as a New Approach to Mineral Carbonation. Front. Clim. 4. https://doi.org/10.3389/fclim.2022.913632

Zhao, L., Sang, L., Jun, C., Ji, J., Teng, H.H., 2010. Aqueous carbonation of natural brucite: Relevance to CO_2 sequestration. Environ. Sci. Technol. 44, 406–411. https://doi.org/10.1021/es9017656

Chapter 3

Field-deployable drainage columns for monitoring enhanced weathering of kimberlite, olivine, and wollastonite

3.1 Introduction

The concentration of CO_2 in Earth's atmosphere has increased to the point that carbon dioxide removal through negative emissions technologies (NETs) is needed to avoid the most damaging effects of global climate change (Minx et al., 2018). Enhanced rock weathering (ERW) is a NET that aims to accelerate CO_2 removal via natural weathering by dispersing rock powders on land and in the oceans. ERW results in the storage of carbon as a dissolved phase (e.g., HCO_3^-), potentially precipitating carbonate (e.g., $CaCO_3$) minerals, a solid and stable sink for CO_2 (Hartmann et al., 2013; Meysman and Montserrat, 2017; Renforth, 2012). Natural silicate weathering currently sequesters CO_2 at an approximate rate of 1.1 Gt/yr (Amann et al., 2020; Strefler et al., 2018b), and has the potential to be greatly accelerated to meet CDR needs. Acceleration can be achieved by addressing variables that may be inhibiting release of cations to solution, often through pre-treatment of feedstocks, which includes physical alterations to grain size and/or chemical amendments like chelate ligands, ionic liquids, and enzymes (Assima et al., 2014; Power et al., 2014; Renforth et al., 2015). Common feedstocks for ERW include Ca- or Mg-rich silicate and hydroxide minerals with relatively fast dissolution rates. Dissolution rates are a function of the solution chemistry, temperature, crystal chemistry, and surface area (Power et al., 2013; Renforth, 2012), with the former two emphasizing the importance of dispersal site, and the latter two relating to the rock powder itself.

As a promising approach for combating greenhouse gas emissions, ERW has garnered significant research aimed at assessing costs, potential co-benefits, and most importantly the capacity and rates of CO_2 sequestration (Amann et al., 2022; Andrews and Taylor, 2019; Beerling et al., 2020; Haque et al., 2019; Paulo et al., 2021; Renforth, 2012; Strefler et al., 2018a). Carbon verification is a critical aspect of CO_2 sequestrations, which is necessary for assigning carbon credits, leading to widescale adoption (Wang et al., 2016). Approaches for verifying carbon removal through ERW include monitoring the increases in dissolved inorganic carbon (DIC) and alkalinity (predominantly as HCO_3) in waters, carbonate mineral abundances through changes in total inorganic carbon (TIC), monitoring elemental fluxes, direct measurements of CO_2 ingress, and emerging approaches like using EC as an indicator of alkalinity (Amann and Hartmann, 2022). These approaches are common in notable micro- and mesocosm studies, and field trials (Buckingham et al., 2022; Hamilton et al., 2021; Kandji et al., 2017; Stubbs et al., 2022; Wood et al., 2022).

Columns have been used in ERW experiments for determining the efficacy of minerals to sequester CO_2. Columns can utilize diverse instrumentation that allow users to calculate rates of CO_2 sequestration based on the release of divalent metal cations, additions of solid carbon, and export of dissolved carbon. For example, extracted soil cores have been leached for quantifying olivine weathering to provide insight into the effects of surface area and energy requirements (Renforth et al., 2015). Flow-through pot experiments have been used to derive CO_2 sequestration rates of olivine by measuring Mg release in agricultural soils (ten Berge et al., 2012). In addition, cropland mesocosms (0.5 m scale) have been used for evaluating cation release and DIC increases, directly

correlated to CDR (Amann et al., 2020). Thus, columns or similar apparatuses are a valuable tool for verifying carbon storage.

Field studies to assess ERW have been conducted and are underway to address carbon verification issues in larger, more complex systems. These studies expose rock powders to real world conditions to understand natural processes while maintaining the ability to enhance weathering and assess rates of sequestration. Methodologies used to determine rates of sequestration in field studies include quantification of secondary carbonates that store CO_2 (Hamilton et al., 2021), elemental fluxes in drainage waters (Amann et al., 2020; Buckingham et al., 2022), total inorganic carbon that may not be detectable using X-ray diffraction (XRD; Haque et al., 2020), and stable carbon isotopes to determine the source of CO_2 (Wilson et al., 2014). Large-scale field deployment of ERW technologies is currently underway, including OceanNETs (2021), Project Carbdown (2021), and Project Vesta (2021), with more being developed.

While progress has been made towards developing ERW as an NET, one component that remains problematic is the monitoring and carbon accounting in complex open systems with large spatial and temporal variabilities. Issues involving carbon accounting include extrapolating rates to large scales, potential non-permeance of carbon sinks, and misrepresenting rates based on incentives (Brander et al., 2021). Reliable carbon accounting is needed to verify CDR and to optimize the rate at which this occurs. Current issues can result in discrepancies between what is theoretically calculated and what is observed in field studies, leading to gross overestimations of a given feedstocks ability to sequester CO_2 (Lu et al., 2022; Rinder and von Hagke, 2021). There has been a lack of methodology and apparatus designed to address this challenge (Brander et al., 2021),

which is an integral part of widescale adoption of ERW technologies. Without advances made in this space, verifying carbon offsets through ERW becomes challenging.

This study explores the use of field-deployable leaching columns to monitor and assess the rates of ERW in a real-world scenario. The objectives of this study are to (1) develop field-deployable columns for monitoring parameters of ERW in field trials, (2) test various methodologies for verifying carbon storage, including tracking carbon as a solid, dissolved, and gas phase, and (3) evaluate kimberlite, olivine, and wollastonite for their use in ERW. The trial consisted of two phases, first indoors for 6 months in a controllable laboratory environment and then outside to expose them to complex climatic conditions. The high-resolution monitoring provided by these columns can aid in the effectiveness of future ERW studies. Allowing for accurate tracking of changes in drainage chemistry and verification of carbon additions, can make these an important tool for determining carbon offsetting and budgeting. Success of this objective would lead to determining the effectiveness of different parameters for assessing CDR rates in varying materials.

3.2 Methods

3.2.1 *Weathering column design*

The design of these columns was based on the Drain Gauge D3 Lysimeter (METER, USA). Plastic 22.7 L (6 gal) rectangular reservoirs were fitted with a clear polycarbonate tube, 61 cm (2 ft) long, with an inner diameter of 19.7 cm (7.75 in). A polyvinyl chloride (PVC) disc was machined to fit within the bottom of the tube acted as an adapter that funnelled drainage waters to the centre. A hollow polypropylene ball with a diameter of 5 cm (2 in) was used at the lower opening of the funnel to limit evaporation from the reservoir while still allowing water to pass by. To prevent material from being flushed into the reservoir, a 6.4 mm (0.25 in) thick PVC disc was cut to fit above the funnel, with eight holes to accommodate 25 cm long fibreglass wicks. A plastic sampling cup with holes at the top was fitted to the bottom of the funnel, which allowed 45 mL of drainage water to be collected before overflowing into the reservoir. Two 6.35 mm inner diameter (0.25 in) Tygon tubes were passed through the reservoir for sampling, with one inserted into the sampling cup for discrete samples and the other fitted with a PTFE flow through tubing weight, allowing the tube to rest at the bottom of the reservoirs for bulk water samples. Holes were drilled through the side of each column for instrumentation to monitor moisture and pore gas CO_2 concentration. Soil moisture sensors (TEROS 12, Meter, USA) were installed at depths of approximately 6 cm to record volumetric water content (VWC% or m^3/m^3), temperature (°C), and electrical conductivity (mS/cm) using ZL6 Advanced Cloud Data Loggers by METER. Soil gas samplers (Meter, USA) were paired with a VAISALA CARBOCAP® Carbon Dioxide Probe GMP343 and a VAISALA M170 Handheld Measurement Indicator.

3.2.2 Experimental methods

Eight columns were assembled using 6±0.1 kg of material (Table 3.1). Materials used were fine-processed kimberlite residues from the Gahcho Kué Diamond Mine, Northwest Territories, Canada, dark volcanoclastic kimberlite (DVK) from the Venetia Diamond Mine, Limpopo Province, South Africa, Wollastonite skarn from the Canadian Wollastonite quarry near Kingston, Ontario, Canada, and forsterite sand purchased from Bell & MacKenzie, Ontario, Canada. Each of the four materials had a duplicate column. Material was added in 3 layers of 2 ±0.1 kg to accommodate sampling devices, resulting in total thicknesses of 12–16 cm. In November 2020, columns excluding DVK were wetted with 1.5 L of deionized water (18.2 MΩ·cm) to achieve 60% saturation. Following this initial wetting, columns received 500 mL of deionized water per week for the first eight weeks, followed by bi-weekly wettings of 1000 mL for another ten weeks, resulting in 10.5 L of total water additions for the laboratory phase of this experiment. Discrete water samples were collected weekly when available, and bulk samples from the reservoirs were collected after the end of the laboratory phase. CO_2 fluxes and pore concentrations were measured daily for the first 4 weeks before the measurement interval was reduced to coincide with water availability. Upon completion of the laboratory phase at 6 months the water reservoirs were emptied and sampled.

In April 2021, columns were moved outdoors to an experimental plot on the campus of Trent University, Peterborough, Ontario, Canada. The two columns containing DVK from Venetia were added at this time. These duplicate columns are henceforth referred to as DVK 1 and DVK 2. Weather data was downloaded from the Trent Weather

Monitoring Station, including temperature, precipitation, and relative humidity at half-hour intervals. Discrete water samples were collected when available. CO_2 fluxes were measured at least weekly at the beginning of the experiment and around rainfall events. The concentration of CO_2 in the pore space was measured at the same frequency as the fluxes.

In November 2021, the contents of the columns were sampled. The upper 0.5 cm of the material was sampled, and the remaining contents were separated into four equal layers by depth. The moisture content of these layers was measured using an HE53 Moisture Analyzer (Mettler Toledo). Each layer were homogenized and allowed to dry at laboratory conditions. The reservoir was emptied, and the water was sampled and prepared for analysis as previously described.

Table 3.1. The physical properties of the columns, and the geochemical composition and mineralogy of the materials used. Precipitation includes the total water additions during the lab phase and rainfall during the outdoor phase. Drainage is the total amount of water that passed through each column during both phases, including sample and reservoir waters. Target minerals identified include potential sources of Ca and Mg and the wt.% they constitute in the solids.

ID	Contents	Porosity (%)	BET (m^2/g)	D50 (μm)	Ca (%)	Mg (%)	Si (%)	Target minerals (wt.%)	Initial TIC (n=3+) (%)	Precipitation (L)	Drainage (L)
GK1	Gahcho Kué kimberlite	56	20.6	70.6	2.9	16.3	20.1	Lz (29), Fo (9)	0.24 ± 0.01	25.8	4.8
GK2		54								25.8	5.1
DVK1	Venetia kimberlite	44	13.6	249.1	4.9	12.3	19.5	Dio (7), Lz (26), Smc (13), Trm (5)	0.86 ± 0.02	25.8	1.7
DVK2		44								25.8	2.2
WOL1	Wollastonite skarn	52	0.75	242.2	18.8	3.5	26.5	Dio (38), Wol (20)	0.29 ± 0.06	25.8	6.9
WOL2		50								25.8	8.2
OLI1	Olivine sand	49	0.24	423.2	0.1	30.1	19.6	Fo (81)	0.01 ± 0.006	25.8	8.9
OLI2		50								25.8	8.7

Minerals identified include Lz– lizardite, Fo– forsterite, Dio– diopside, Wol– wollastonite, Smc– smectite, Trm– tremolite

3.2.3 Column characterization

The two Gahcho Kué kimberlite columns (GK1, GK2) had porosities of 56% and 54%, respectively. The BET surface area of the material that filled the columns was 20.6 m^2/g, while the average particle size was found to be 70.6 µm. The geochemical analysis of the kimberlite revealed that Ca, Mg, and Si made up 2.9 wt.%, 16.3 wt.%, and 20.1 wt.% of the sample, respectively. Initial TIC content was 0.24 ± 0.01%. GK1 and GK2 were exposed to 25.8 L of water additions, and drained 4.8 and 5.1 L, respectively (Table 3.1).

Both Venetia DVK columns (DVK1 and DVK2) had the same porosity of 44%. This kimberlite had a specific surface area of 13.6 m^2/g, and an average particle size of 249 µm. Ca, Mg, and Si comprised 4.9 wt.%, 12.3 wt.%, and 19.5 wt.%, respectively. The initial material showed TIC present at 0.86 ±0.02%. Both columns experienced 25.8 L of water additions, with 1.7 and 2.2 L draining through DVK1 and DVK2, respectively (Table 3.1).

The columns containing wollastonite skarn (WOL1 and WOL2) had porosities of 52% and 50%, respectively. Material had a specific surface area of 0.75 m^2/g, and an average particle size of 242.2 µm. This feedstock was comprised of 18.8 wt.% Ca, 3.5 wt.% Mg, and 26.5 wt.% Si, with 0.29 ±0.06 % TIC. WOL1 and WOL2 were exposed to 25.8 L of precipitation while draining 6.9 and 8.2 L, respectively (Table 3.1).

Olivine sand columns (OLI1 and OLI2) had a porosity of 49% and 50%, respectively. The material that filled these columns has a specific surface area of 0.24 m^2/g, with an average particle size of 423.2 µm. This samples geochemical composition consisted of 0.1 wt.% Ca, 30.1 wt.% Mg, and 19.6 wt.% Si. The initial material had TIC

present at 0.01 ±0.006%. OLI1 and OLI2 received a total precipitation of 25.8 L, with 8.9 and 8.7 L draining through (Table 3.1).

Additional characterization data for all feedstocks can be found in chapter 2, including mineral identification and quantification via XRD, the full suite of major oxides comprising the samples geochemistry, and trace elements in the solid samples.

During the lab phase, columns were exposed to daily temperatures ranging from 18.3–22.5 ºC, while the outdoor phase ranged between -1.6–25.7 ºC (Fig. 3.1). Temperatures below 0 ºC were only experienced during three days in April when the columns were initially transitioned outdoors. Natural precipitation experienced during the outdoor phase totaled 15,340 mL, with significant contributions to this coming during July and September (Fig. 3.1).

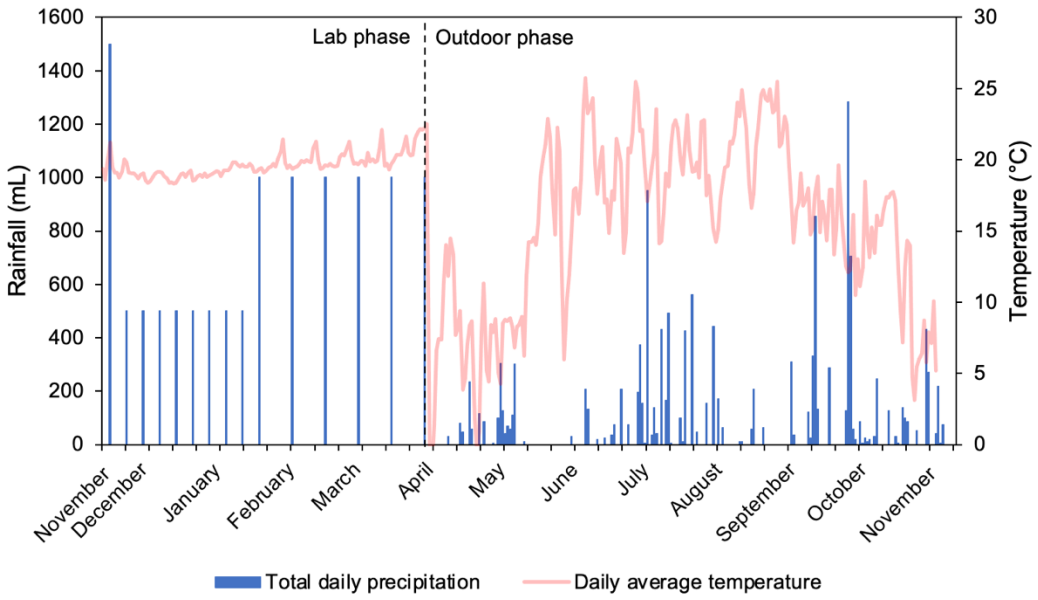

Figure 3.1. Precipitation and temperature data for the lab and outdoor phases. The outdoor phase data was obtained from the Trent Weather Monitoring Station.

3.2.4 Water analysis

The pH of the water samples was measured using an Orion Star A321 pH meter. Waters were filtered (0.22 μm) prior to Cation, anion, and trace metal analysis, which was conducted at Trent University by the Water Quality Centre. Cation analyses was performed on acidified samples (2% v/v ultrapure HNO_3, Aristar ®, UK) by inductively coupled plasma - optical emission spectrometry (ICP-OES) with an Optima 7000 DV (Perkin Elmer, USA) with detection limits (MDL) for Ca, Mg, Na, and Si at 0.13, 0.01, 0.05, and 0.06 mg/L, respectively. Anion analyses was performed by ion chromatography (IC) using a Dionex/ Thermo Scientific ICS-1100 with detection limits for Fl, Cl, NO_2, and PO_4 at 0.035, 0.048, 0.014, and 0.046 mg/L, respectively. Trace element analyses was performed on acidified samples using inductively coupled plasma-mass spectroscopy (ICP-QQQ-MS) using an Aligent 8000 Triple Quadrupole ICP-MS with detection. Limits for Al, Cr, Co, Ni, and Cu at 0.633, 0.097, 0.0024, 0.095, and 0.024 μg/L, respectively. Blanks and standards (10 ppm Ca standard for ICP-OES, Ricca Chemical, USA, and VeriSpec© Mixed Anion Standard 7, Ricca Chemical, USA) were used to verify the accuracy of these methods.

Dissolved inorganic carbon (DIC) was determined using a Model CM5017 coulometer from UIC Inc. at Trent University. Calibration of the instrument was conducted daily using blanks and bicarbonate standards of 125, 250, and 500 ppm. Detection limits of this instrument are between 0.0001–100% C with a precision of 0.01 mg C/L. Samples (1.0 mL) were reacted with 2 N H_2SO_4 (10 mL) at 50 °C, with a carrier gas rate of 100 mL/min through the acidification module. The pre-scrubber removed any CO_2 present in the carrier gas using potassium hydroxide (45%), while the post-scrubber

removed H_2S, SO_x, and/or halogens using silver nitrate (3 v/v%). The colorimetric cell contained monoethanolamine mixed with a colour indicator and two electrodes (platinum and silver), creating a titratable acid, changing the colour of the solution and its transmittance (%), which is proportional to the concentration of inorganic carbon injected into the cell.

Alkalinity analyses were conducted on the final reservoir waters using a Xylem TitroLine® 7000-M2/20 titrator. Samples were transferred into 30 mL beakers with a 2 cm magnetic stir bar. Initial pH was measured using an SI analytics® Blueline pH electrode which recorded pH continuously for the analysis duration. After a 25-second hold, the titration began using 0.01 N HCl at a step size of 0.025 mL until an endpoint of pH 3.1 was reached. The instrument was calibrated daily using blanks (ASTM Type II Deionized, Distilled water, Sigma-Aldrich Canada) and $NaHCO_3$ standards ranging from 25–500 ppm. The equivalence volume was calculated using the Gran method (Eq. 3.1). The result of this function was plotted against the volume of acid added (V_t) to determine the intercept where all HCO_3^- has been converted to H_2CO_3, which was used to calculate the alkalinity of the sample using Eq. 3.1:

$$F = (V_0 + V_t) \cdot 10^{-pH} \quad (3.1)$$

where V_0 represents the initial volume of the sample, V_t represents the volume of acid added, and pH is the value recorded at that volume.

3.2.5 CO_2 fluxes and pore gas measurements

CO_2 flux measurements were conducted using an LI-8100 soil CO_2 flux system with survey chamber. The CO_2 diffusion rate ($\mu mol/m^2/s$) was measured within the

chamber that seals around the opening of the column, providing insight onto the uptake of CO_2 into the material (ingress, represented by negative values), or the release of CO_2 (efflux, represented by positive values). The instrument was programmed to measure the flux for 2 min, followed by a 1-min post-purge, which was repeated three times before the chamber was moved to the next column for analysis. Data from the flux analyzer was processed using SoilFluxPro 4.0.1. All datasets were fitted to an exponential curve, and all measurements with an R^2 value <0.5 were removed. The remaining data points were exported for further data analysis and interpretation.

The concentration of CO_2 in the pore space was measured using a BLDG-100 soil gas sampler (METER, U.S.A.) connected to a Vaisala GMP343 carbon dioxide probe and an MI70 measurement indicator. A 60 mL syringe was used to draw pore gas through the probe for measurement. Values were recorded by the indicator and processed using the Vaisala M170 Link application (v1.16.), which provided the minimum, maximum, and mean concentrations of CO_2 for each measurement.

3.2.6 Solid analysis

All dry and homogenized solids from the columns were subsampled and pulverized (FLSmidth Essa® LM2 Pulverizing Mill) for 1 min to a fine particle size. TIC was analyzed using the methodology described in chapter 2. Blanks and $CaCO_3$ standards (Alfa Aesar; 99.95–100.05% purity) were used to verify the accuracy of the method. Triplicate samples were analyzed for all five layers removed from each column.

3.2.7 PHREEQC modelling

PHREEQC (Parkhurst and Appelo, 2013), with the carbfix.dat database (Marieni et al., 2018), was used for all geochemical models. Water chemistry and mineralogical data were imported to PHREEQC to assess the charge balance and determine saturation indices. Thermodynamic data for hydromagnesite (Gautier et al., 2014), magnesite (Bénézeth et al., 2011), brucite (Brown et al., 1996), nesquehonite and dypingite (Harrison et al., 2019) were added to the model input.

3.3 Results

3.3.1 Water chemistry

GK1 and GK2 released their highest Ca concentrations of 196 and 265 mg/L at 64 days, respectively, when discrete samples were first collected (Fig 3.2A). Ca concentrations in GK1 and GK2 declined in the leachate for the remaining lab phase, reaching values of 118 and 155 mg/L, respectively, in the final discrete samples, while reservoir samples had Ca concentrations of 212 and 251 mg/L, respectively. An increase in Ca was seen in the final initial discrete samples of the outdoor phase, with values of 203 and 196 mg/L for GK1 and GK2, respectively. The discrete samples from the outdoor phase followed a similar trend of decreasing Ca concentrations, albeit with lower concentrations than in the lab phase, with Ca concentrations in GK columns declining steadily to 16 and 25 mg/L. Final reservoir samples had Ca concentrations of 109 and 95 mg/L for GK1 and GK2, respectively. Mg in the discrete leachate of GK1 and GK2 during the lab phase ranged from 52–76 mg/L and 29–43 mg/L, respectively, with reservoir values of 87 and 43 mg/L, respectively. During the outdoor phase, Mg concentrations ranged from 7–64 mg/L and 8–31 mg/L with reservoir concentrations of 43 and 15 mg/L in GK1 and GK2, respectively (Fig 3.2A). Si concentrations exhibited little variation between discrete and reservoir samples, ranging from 40–49 mg/L in GK1, and 48–34 mg/L in GK2 (Fig 3.2A). DIC of the first drainage samples produced by GK1 and GK2 was 9 and 10 mg C/L, respectively, with values declining to 2–5 mg C/L for the remainder of the lab phase. The reservoir waters sampled between phases contained 13 and 7 mg C/L for GK1 and GK2, respectively. The DIC in the discrete samples of the outdoor phase decreased from 7 to 3 mg C/L in both columns, with final reservoir

concentrations of 8 and 5 mg C/L for GK1 and 2, respectively (Fig. 3.2 B). Alkalinities of the reservoir waters were in good agreement with DIC concentrations, differing by <15%. pH of discrete samples in the lab ranged from 6.6–7.7 in GK1 and 6.1–7.4 in GK2. Similarly, pH values ranged from 6.4–7.6 in GK1 and 6.9–7.7 in GK2 during the outdoor phase, with a trend of increasing values observed throughout the experiment (Fig 3.2C). Aragonite ($CaCO_3$) was near saturation at the end of each phase for GK columns (saturation indices = -0.07 and -0.04), while calcite ($CaCO_3$) was slightly supersaturated (0.08 and 0.11). Both hydromagnesite [$Mg_5(CO_3)_4(OH)_2{\cdot}H_2O$; -14.04 and -14.57] and amorphous silica (SiO_2; -0.38 and -1.89) were undersaturated. (Table 3.2). All columns (except DVK) experienced a total water addition of 25.8 L, with GK 1 and 2 draining 4.8 and 5.1 L, respectively, while retaining an average of 1.2 L (Table 3.1)

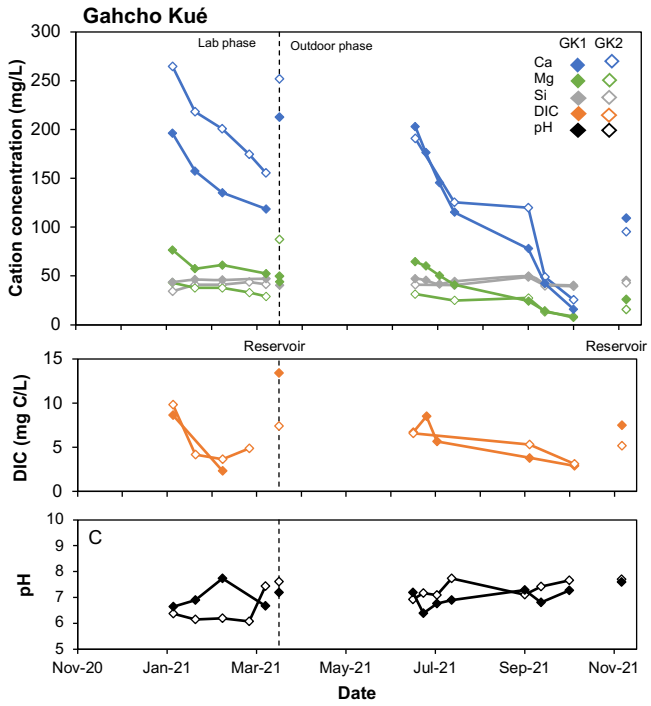

Figure 3.2. Ca, Mg, and Si concentrations (A), DIC (B), and pH values (C) of the discrete leachate samples for GK columns. Gaps in the data occur when there was no drainage to collect. Reservoir water samples of the lab and outdoor phases are represented by symbols that do not connect to the lines.

DVK columns were deployed at the start of the outdoor phase and first drained after 128 days (Fig. 3.3A). DVK1 initially showed higher concentrations of Ca and Mg (65 and 45 mg/L, respectively) compared to DVK2 (22 and 8 mg/L, respectively). The second discrete sample from DVK1 showed a significant decrease in Ca and Mg concentrations, while DVK2 showed a slight increase in Ca and Mg. The remaining discrete samples for both columns were within the range of 5–20 mg/L and 3–15 mg/L for Ca and Mg, respectively (Fig. 3.3A). The Si concentration in the discrete drainage samples of DVK 1 and 2 ranged from 51–82 mg/L (Fig. 3.3A). DVK 1 and 2 reservoir samples had Ca concentrations of 27 and 36 mg/L, respectively, Mg concentrations of 21 and 25 mg/L, respectively, and Si concentrations of 71 and 82 mg/L, respectively (Fig. 3.3A). DVK columns had DIC concentrations that ranged from 92–153 mg C/L, with the lowest values observed in the final reservoir samples (Fig. 3.3B). The lowest pH values were observed in the initial samples, with values of 7.2, which rose to a range of 8.6–8.8 for the remaining samples (Fig. 3.3C). Aragonite (saturation index = 0.83) and calcite (0.97) were supersaturated in the final reservoir waters, while hydromagnesite (-7.53) and amorphous silica (-0.19) were undersaturated (Table 3.2). During the outdoor phase when exposed to 15.3 L of precipitation, DVK 1 and 2 drained 1.7 and 2.2 L, respectively, while storing 3.8 and 4.3 L, predominantly as surface pooling (Table 3.1).

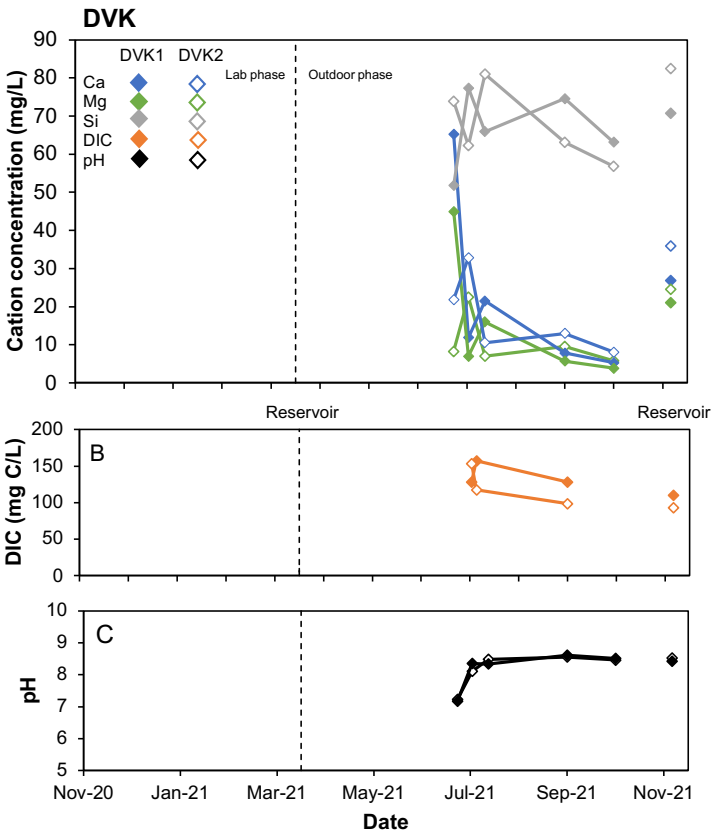

Figure 3.3. Ca, Mg, and Si concentrations (A), DIC (B), and pH values (C) of the discrete leachate samples for DVK columns. Gaps in the data occur when there was no drainage to collect. There was not a lab phase for the DVK columns. Reservoir water samples of the outdoor phase is represented by symbols that do not connect to the lines.

The Ca concentrations during the lab phase of WOL 1 and 2 columns progressively declined from 665 and 748 mg/L, respectively, to 44 mg/L for both columns. (Fig. 3.4A). Reservoir Ca concentrations measured between the lab and outdoor phases were 744 and 687 mg/L compared to the final reservoir concentrations of 239 and 220 mg/L for WOL 1 and 2, respectively (Fig. 3.4A). The Mg and Si concentrations in the discrete and reservoir waters exhibited minimal change throughout the experiment, with values of ~10 and ~50 mg/L, respectively (Fig. 3.4A). The concentration of DIC in the discrete leachate of the lab phase ranged from 4–10 mg C/L, while concentrations of

3 mg C/L were observed in the bulk leachate at the end of this phase. During the outdoor phase, the concentration of DIC increased from 3–8 mg C/L, with values of 9 mg C/L observed in the final reservoir leachate (Fig. 2.4B). The pH values observed in the WOL leachates experienced minimal change, with a range of 6.7–7.8 (Fig. 3.4C). Aragonite (0.06 and -0.04) and calcite (0.21 and 0.12) were near saturation at the conclusion of each phase, while hydromagnesite (-20.66 and -21.41) and amorphous silica (-0.22 and -0.39) were both undersaturated (Table 3.2). WOL 1 drained 6.9 L while WOL 2 drained 8.2 L. Both columns retained 0.8 L (Table 3.1).

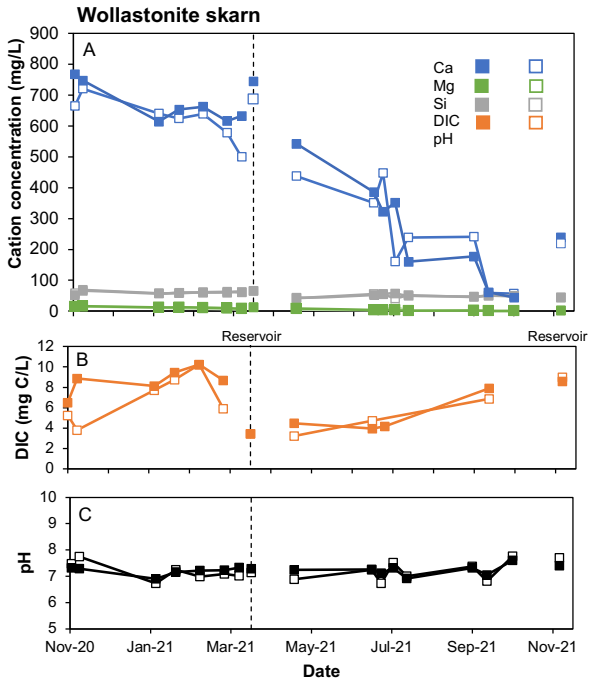

Figure 3.4. Ca, Mg, and Si concentrations (A), DIC (B), and pH values (C) of the discrete leachate samples for WOL columns. Gaps in the data occur when there was no drainage to collect. Reservoir water samples of the lab and outdoor phases are represented by symbols that do not connect to the lines.

The Mg measured in the discrete drainage of both OLI columns during the lab phase ranged from 25–60 mg/L, with a potential outlier of 83 mg/L observed in the last discrete measurement of the lab phase (Fig. 3.5A). Bulk Mg concentrations were

measured at 42 and 38 mg/L for OLI1 and 49 and 39 mg/L for OLI2 (Fig. 3.5A). The concentration of Mg observed during the outdoor phase was highest in the first two samples of OLI1, with values of 88 and 91 mg/L, which then declined to a minimum value of 15 mg/L. OLI2 did not produce discrete samples at the same rate as OLI1 and had a range of 21–45 mg/L (Fig. 3.5A). The OLI columns released minimal Ca and Si with concentrations ranging from 2–12 mg/L and 2–9 mg/L, respectively (Fig. 3.5A). Reservoir Ca concentrations were 21 and 11 mg/L for OLI1 and OLI2, respectively. The DIC in the discrete samples ranged from 11–108 mg C/L, with values of 82 and 64 mg C/L observed in the reservoir leachate at the end of the lab phase. During the outdoor phase, the discrete leachate samples had DIC concentrations between 5 and 91 mg C/L, with final reservoir concentrations of 57 mg C/L for both columns (Fig. 3.5B). The pH values of the drainage waters ranged from 7.1–8.9 and showed no trend during the experiment (Fig. 3.5C). Aragonite and calcite were slightly supersaturated after each phase, while hydromagnesite and amorphous silica were consistently undersaturated (Table 3.2). OLI 1 and 2 drained 8.9 and 8.7 L, respectively, whole storing 0.5 L (Table 3.1).

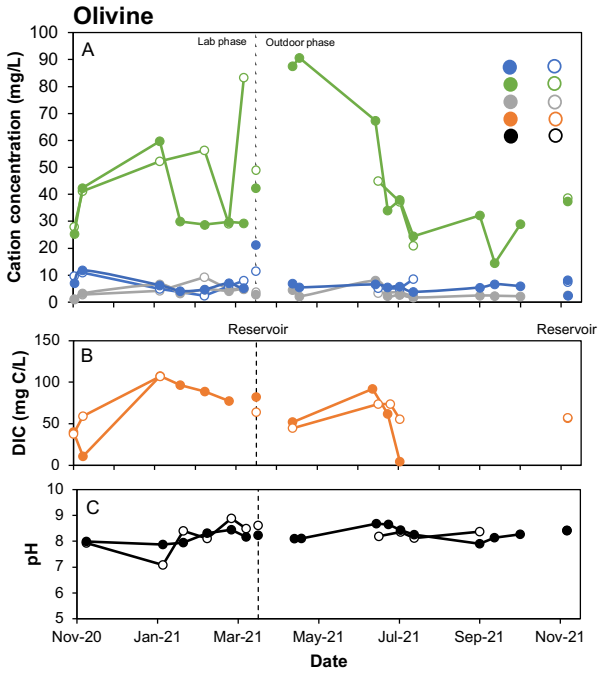

Figure 3.5. Ca, Mg, and Si concentrations (A), DIC (B), and pH values (C) of the discrete leachate samples for OLI columns. Gaps in the data occur when there was no drainage to collect. Reservoir water samples of the lab and outdoor phases are represented by symbols that do not connect to the lines.

Table 3.2. Saturation indices of aragonite, calcite, hydromagnesite, and amorphous silica in the reservoir waters sampled at the conclusion of the lab phase (LP) and outdoor phase (OP). Values are an average of the two columns of each type.

	Aragonite		Calcite		Hydromagnesite		SiO_2 (am)	
	LP	LP	LP	OP	LP	OP	LP	OP
GK	-0.07	-0.04	0.08	0.11	-14.04	-14.57	-0.38	-1.89
DVK	n/a	0.83	n/a	0.97	n/a	-7.53	n/a	-0.19
WOL	0.06	-0.04	0.21	0.12	-20.66	-21.41	-0.22	-0.39
OLI	0.31	0.21	0.46	0.36	-7.14	-5.92	-1.54	-1.65

Nutrient (K and P) releases were calculated and reported on a per mass basis and the concentrations provided are of the reservoir waters. The duplicate columns showed consistent values and are reported as averages. K release from GK columns amounted to 26 and 96 mg/kg in the lab and outdoor phase, respectively, while the concentrations in the reservoirs were 420 and 141 mg/L, respectively (Fig. 3.6A). DVK columns released 28 mg K/kg, respectively during the outdoor phase, with concentrations of 163 mg/L observed. (Fig. 3.6A). WOL columns released the least K, averaging 2 mg/kg during each phase, equating to concentrations of 10 and 2 mg/L for the lab and outdoor phases, respectively (Fig. 3.6A). K release from OLI columns during the lab and outdoor phases equalled 11 and 65 mg/kg, respectively, the concentration of K observed were 81 and 43 mg/L, respectively for each phase (Fig. 3.6A).

GK columns released an average of 0.005 mg P/kg during the lab phase and 0.009 mg P/kg during the outdoor phase. The concentrations of P observed in GK columns were 79 and 13 µg/L for the lab and outdoor phase, respectively (Fig. 3.6B). P released from DVK columns equated to 0.005 mg/kg, representing a concentration of 26 µg/L. WOL released 0.035 mg/kg during the lab phase and 0.022 mg/kg during the outdoor phase (Fig. 3.6B). P was observed at 2213.3 and 17 µg/L during the lab and outdoor phases, respectively (Fig. 3.6B). OLI columns release 0.01 mg P/kg during each phase, equating to concentrations of 69 and 6 µg/L for the lab and outdoor phase, respectively (Fig. 3.6B).

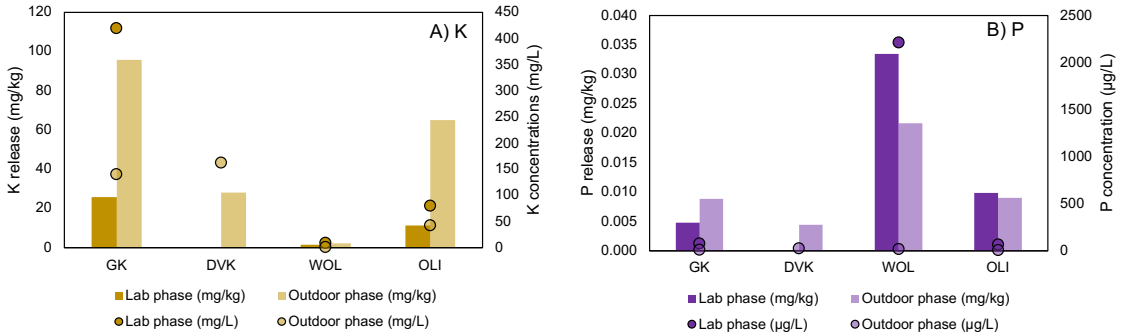

Figure 3.6. The average (n=2) amount of K (A) and P (B) released each column type (mg/kg) during the lab and outdoor phases, represented by bars (Y-axis). The average concentration of each element in reservoir leachates (mg/L for K and µg/L for P) are represented by circles on the secondary Y-axis.

The release of deleterious metals (Ni and Cr) was calculated and reported on a per mass basis and the concentrations provided are of the reservoir waters. Duplicate columns showed consistent values and are reported as averages. GK columns released 1.4 µg Ni/kg during the lab phase, while 3.7 µg Ni/kg was released during the outdoor phase (Fig. 3.7A). Ni concentrations in GK reservoirs averaged 23 and 6 µg/L during the lab and outdoor phase, respectively (Fig. 3.7A). The Ni released from DVK columns during the outdoor phase averaged 4.3 µg/kg, while the concentrations observed in the reservoirs averaged 25 µg/L (Fig. 3.7A). The average Ni release from WOL equalled 1.3 and 1.1 µg/kg during the lab and outdoor phase, respectively. Concentrations of Ni observed in WOL columns averaged 9 and 1 µg/L in the lab and outdoor phases, respectively (Fig. 3.7A). Olivine columns released an average of 2.2 µg Ni/kg during the lab phase and 5.1 µg Ni/kg during the outdoor phase. The concentrations Ni released from OLI averaged 11 and 3 µg/L during the lab and outdoor phase, respectively (Fig. 3.7A).

All columns released <0.25 µg Cr/kg during the lab phase, with corresponding concentrations of <1.5 µg Cr/L (Fig. 3.7B). Apart from DVK, which released an average

of 1.1 µg Cr/kg and 6 µg Cr/L during the outdoor phase, all other columns released <0.8 µg Cr/kg and <0.5 µg/L (Fig. 3.7B).

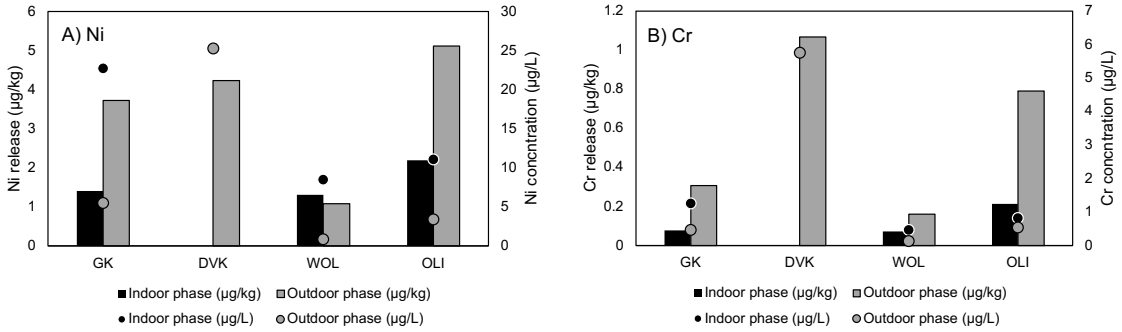

Figure 3.7. The average (n=2) amount of Ni (A) and Cr (B) released from each column type (µg/kg) during the lab and outdoor phases, represented by bars (Y-axis). The average concentrations of each element in the reservoir leachate (µg/L) are represented by circles on the secondary Y-axis.

3.3.2 CO_2 fluxes and pore gas concentrations

GK1 encountered instrument issues during the first 12 measurements and therefore did not show the negative fluxes that GK2 exhibited at the beginning of the experiment. These negative fluxes indicate an initial period of reactivity where GK2 was drawing down -2750 to -500 g $CO_2/m^2/yr$ before reaching near-zero fluxes for the remainder of the lab phase, a trend shared with GK2 (Fig. 3.8A, B). During the outdoor phase, the fluxes of GK2 ranged from -750 to 750 g $CO_2/m^2/yr$, which both occurred when the material was at 18% saturation (Fig. 3.8B). GK1 experienced more positive fluxes than GK2 in frequency and count, with a range of -340 to 1360 g $CO_2/m^2/yr$, which also occurred at similar saturations (Fig. 3.8A, B). Both GK columns show an increase in pore CO_2 concentrations during the lab phase, which is reduced once columns are transitioned outdoors, where they fluctuate between 100 and 250 ppm (Fig. 3.8A, B)

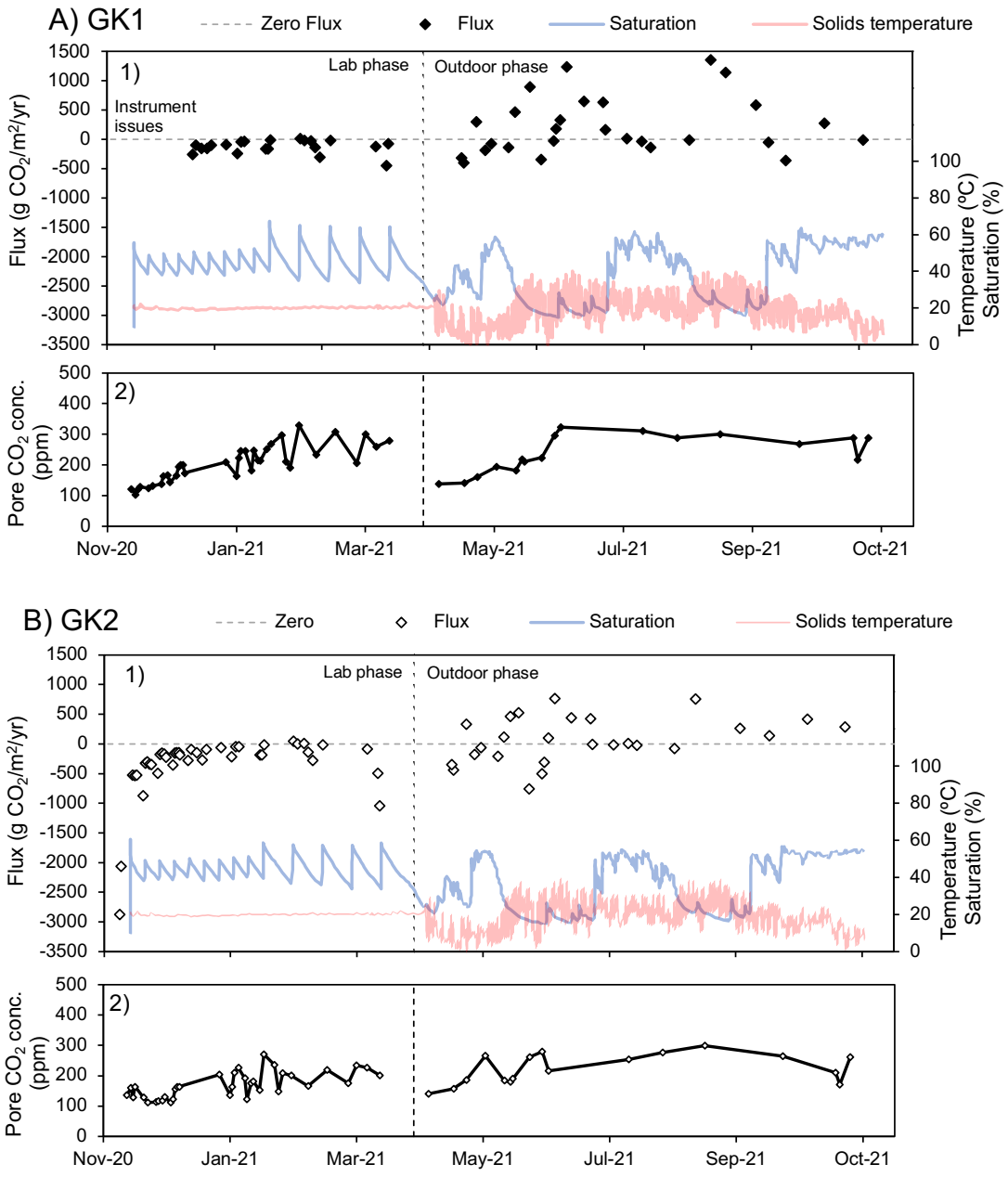

Figure 3.8. 1) CO_2 flux (g $CO_2/m^2/yr.$), water saturation (%), and temperature (ºC) data for GK1 (A) and GK2 (B) columns. Positive and negative values represent effluxes and influxes of CO_2, respectively. Blue and red lines represent the water saturation and temperature of the solids, respectively. 2) Pore CO_2 concentrations (ppm) as measured using a soil gas lance and Vaisala CO_2 meter.

DVK columns experienced significant pooling at the top of the column, as represented by their high saturation percentages (up to 75%), which resulted in the inability to measure fluxes at these times. When flux measurements were possible, nearly all measurements were positive for both columns reaching up to ~850 g $CO_2/m^2/yr$ for DVK1 and 2, respectively (Fig. 3.9A, B). Two measurements for each column indicated influx of CO_2, which were -166 and -92 g $CO_2/m^2/yr$ for DVK1, and -160 and -650 g $CO_2/m^2/yr$, occurring at 40% and 60% saturation, respectively, for each column (Fig. 3.9A, B). The pore CO_2 concentrations of DVK1 ranged between 250 and 450 ppm, while DVK2 remained consistently between 200 and 300 ppm (Fig. 3.9A, B).

Both WOL columns experienced an initial period of reactivity similar to that observed for GK columns, with the first two fluxes from WOL 1 and 2 showing drawdowns of -1100 and -900 g $CO_2/m^2/yr$, respectively (Fig. 3.10A, B). Fluxes correlated with the controlled wetting and drying cycles during the lab phase and were typically lowest when the material was least saturated. The low fluxes observed at the start (-300 g $CO_2/m^2/yr$) became progressively more negative as the phase progressed, reaching -1000 g $CO_2/m^2/yr$. During the outdoor phases, fluxes were less predictable, yet remained negative for the duration of this phase and appear to still be correlated with saturation. Apart from the initial reactive period, the lowest fluxes in WOL 1 and 2 were observed during the outdoor phase with values of -1026 and -1145 g $CO_2/m^2/yr$, respectively, when each column was ~30% saturated (Fig. 3.10A, B). The concentrations of CO_2 in their pore space of both columns ranged from 175 to 300 ppm (Fig. 3.10A, B).

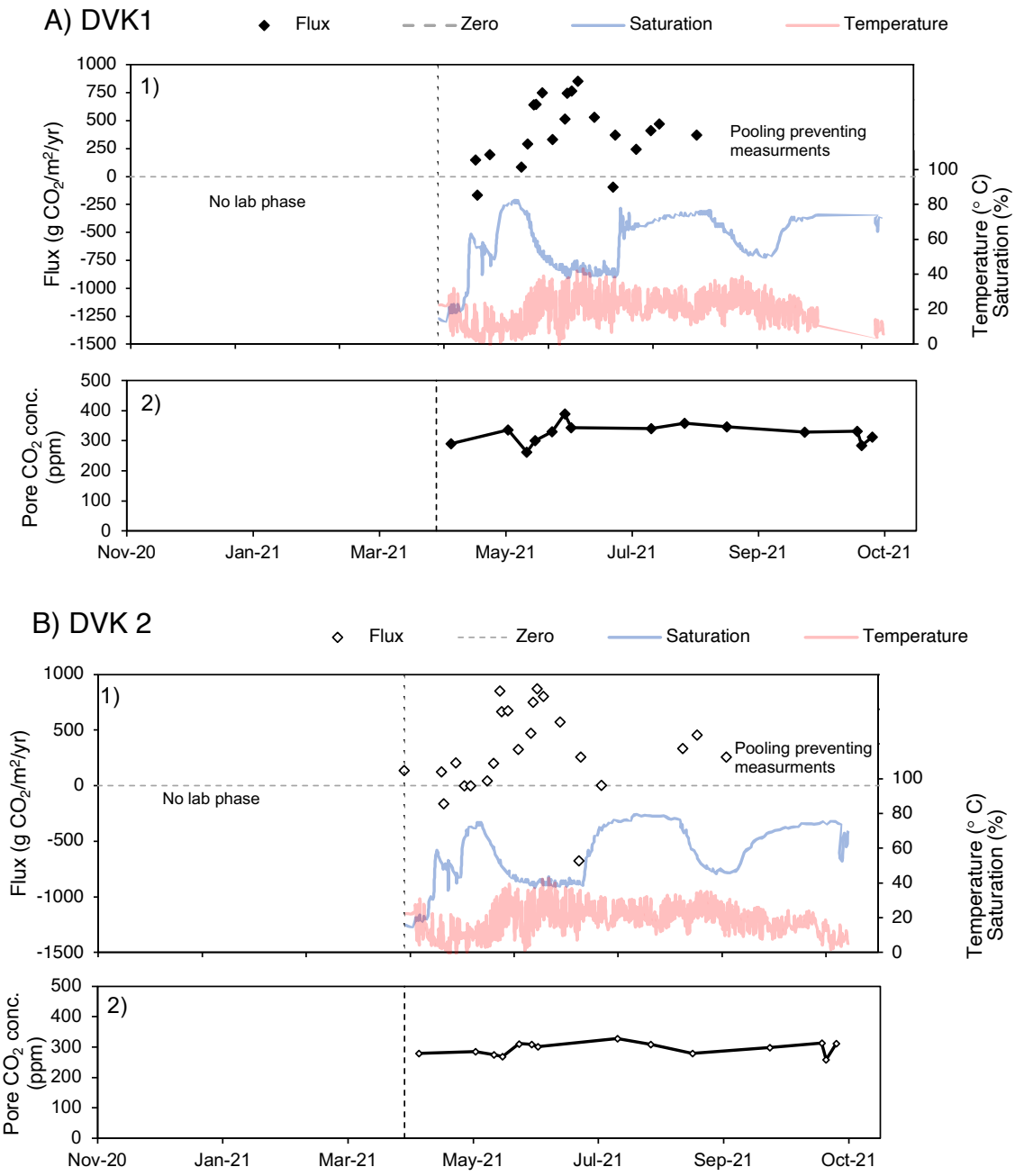

Figure 3.9 1) CO_2 flux (g $CO_2/m^2/yr$.), water saturation (%), and temperature (ºC) data for DVK1 (A) and DVK2 (B) columns. Positive and negative values represent effluxes and influxes of CO_2, respectively. Blue and red lines represent the water saturation and temperature of the solids, respectively. 2) Pore CO_2 concentrations (ppm) as measured using a soil gas lance and Vaisala CO_2 meter.

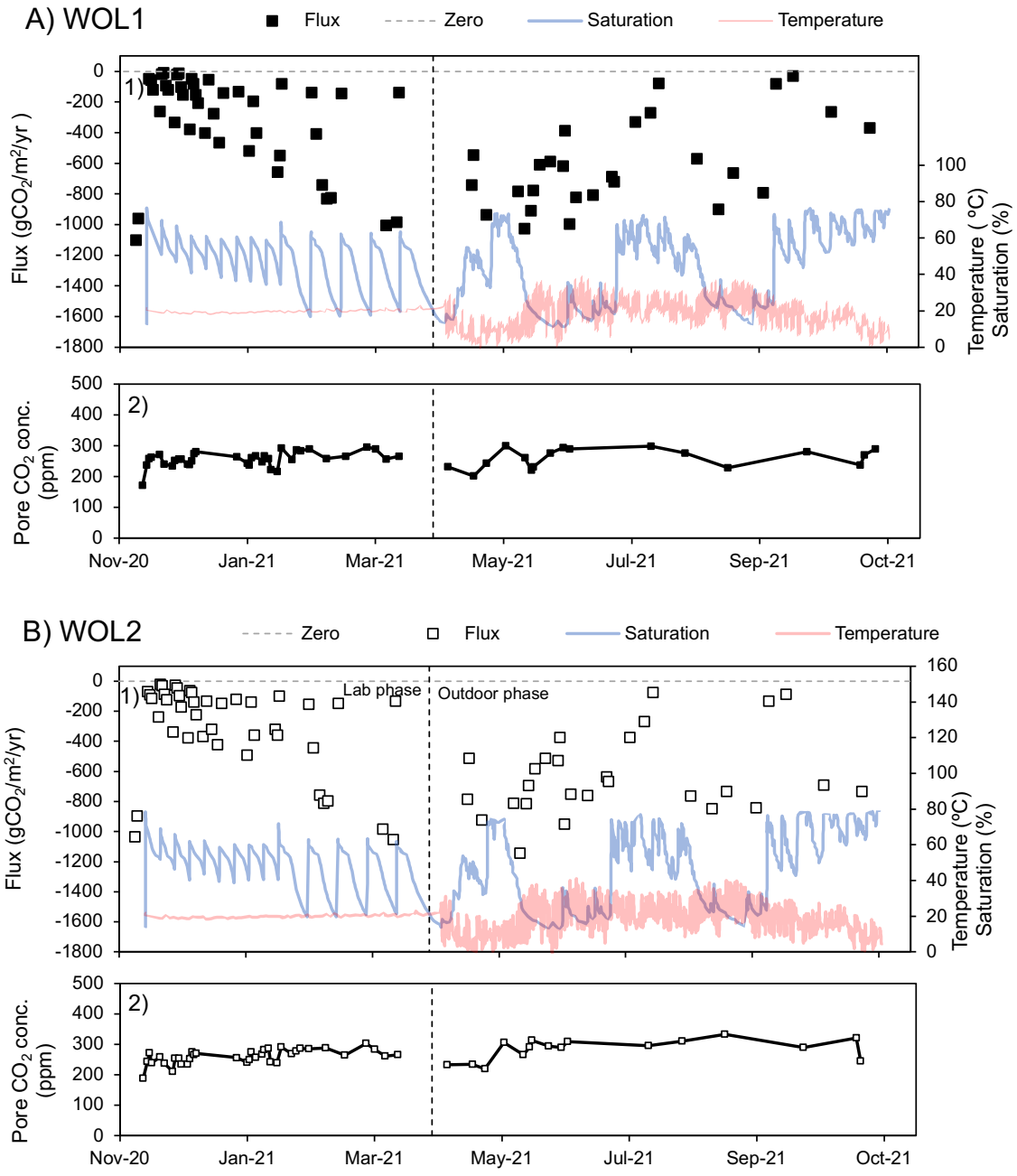

Figure 3.10. 1) CO_2 flux (g CO_2/m^2/yr.), water saturation (%), and temperature (ºC) data for WOL1 (A) and WOL2 (B) columns. Positive and negative values represent effluxes and influxes of CO_2, respectively. Blue and red lines represent the water saturation and temperature of the solids, respectively. 2) Pore CO_2 concentrations (ppm) as measured using a soil gas lance and Vaisala CO_2 meter.

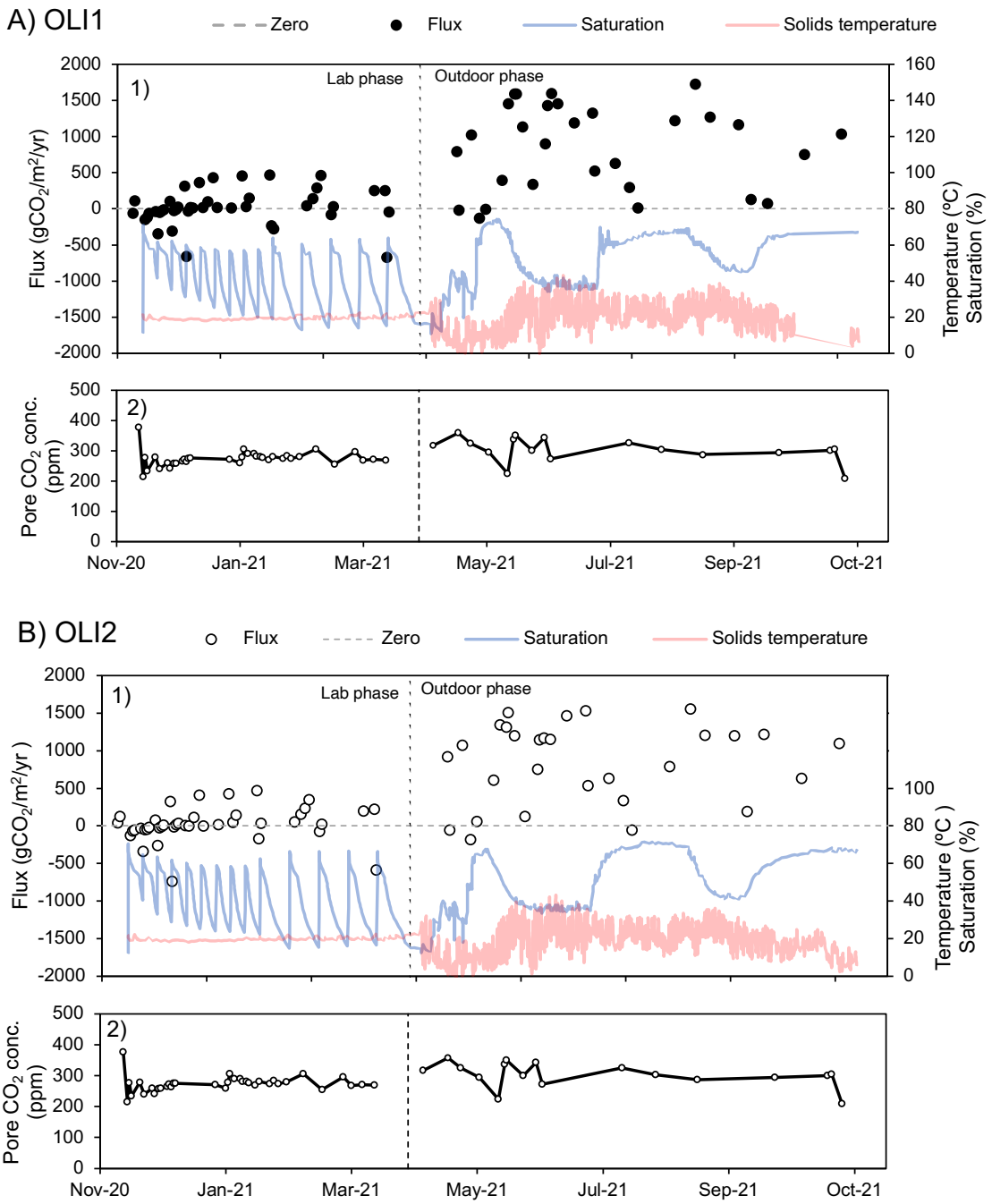

Figure 3.11. 1) CO_2 flux (g $CO_2/m^2/yr.$), water saturation (%), and temperature (ºC) data for OLI1 (A) and OLI2 (B) columns. Positive and negative values represent effluxes and influxes of CO_2, respectively. Blue and red lines represent the water saturation and temperature of the solids, respectively. 2) Pore CO_2 concentrations (ppm) as measured using a soil gas lance and Vaisala CO_2 meter.

CO_2 fluxes for OLI 1 and 2 ranged from -631to 1721 g $CO_2/m^2/yr$ and -742 to 1554 g $CO_2/m^2/yr$, respectively. All but <20 fluxes were positive, with the only significant negative fluxes experienced during the lab phase. The two most negative fluxes observed for OLI 1 and 2 were observed at 50%–60% saturation (Fig. 3.11 A, B). Initial concentrations of CO_2 in the pore space of OLI columns measured at ~400 ppm, while remaining measurements ranged between 200 and 300 ppm (Fig. 3.11A, B).

3.3.3 Total inorganic carbon of final solids

The GK columns (Fig. 3.12A) experienced TIC increases between 0–6 cm (+0.03% and +0.017%), minimal change from the initial at 6–14 cm (+0.007% and +0.005%), and their most significant increase at the lowest horizon of 14–18 cm (+0.03% and +0.03%). DVK 1 and DVK2 lost TIC in all layers, with decreases ranging from -0.002% to -0.092% and -0.04% to -0.1%, respectively (Fig. 3.12B). WOL columns increased from the average initial TIC in all layers, with the most significant increase observed at the surface (+0.32% and +0.23%). Both WOL columns exhibited a similar trend of increasing TIC with increasing depth (Fig. 3.12C). OLI columns lost TIC throughout the profile of each column, with all depths seeing small changes of -0.015% from the initial value (Fig. 3.12D).

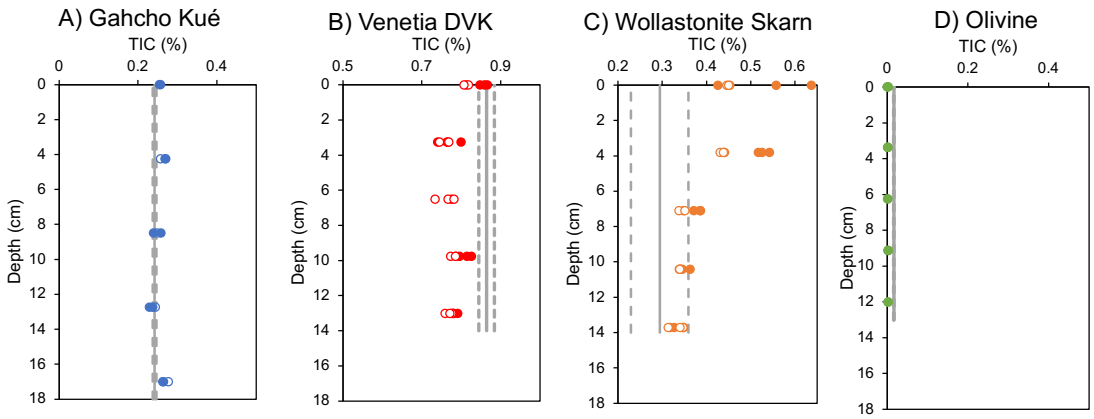

Figure 3.12. The total inorganic carbon (%C) measured at each layer of the column after the conclusion of the experiment for GK (A), DVK (B), WOL (C), and OLI (D). Open symbols represent column 1 of that type, and closed symbols represent column 2. Triplicate measurements were performed at each horizon, with each symbol representing one value. Average initial TIC values (n=3+) are represented by a solid grey line, with those values standard deviation represented by dotted grey lines

3.4 Discussion

3.4.1 Weathering processes

The Mg released from the GK residues can be attributed to silicate dissolution as Mg-carbonates were absent from this kimberlite. Probable silicate sources of Mg found in GK residues include lizardite [$Mg_3(Si_2O_5)(OH)_4$] and forsterite (Mg_2SiO_4), present at 29 wt.% and 9 wt.%, respectively (Table 3.1). These minerals have good potential for enhanced weathering (Bullock et al., 2021), given their favourable dissolution rates of 10^{-16} and 10^{-14} mol/cm^2/s, respectively, at the pH observed in this study (Daval et al., 2013; Pokrovsky and Schott, 2000). Reactive minerals within feedstocks is critical to sequester CO_2 via their the readily released divalent metal cations, mainly Ca^{2+} and Mg^{2+} (Table 3.3; Paulo et al., 2021). The concentration of Mg in the discrete leachate of GK was initially high yet continuously declined (Fig. 3.2), indicating the release of labile Mg ions in the initial stages before recalcitrant bulk silicate becomes the primary source of Mg. Labile Mg, defined as loosely bound Mg ions on the surfaces of minerals, is easily extractable compared to the bulk Mg-silicate which is recalcitrant (Thom et al., 2013c). A similar trend was observed in the leachate chemistry of DVK (Fig. 3.3), although the presence of the Mg-carbonate dolomite [$CaMg(CO_3)_2$] complicate its interpretation. Additionally, acid activation in the interchangeable layers of smectite in DVK may be contributing Ca and Mg via the replacement of these ions with protons (H^+), and is a source of labile cations in kimberlites (Komadel, 2003; Zeyen et al., 2022). The average grain sizes of GK and DVK are 70.6 and 249.1 μm, with resulting surface areas of 20.6 and 13.6 m^2/g, respectively (Table 3.1), with grain size and surface areas showing a significant effect on dissolution rates (Power et al., 2013; Rinder and von Hagke, 2021).

However, GK and DVK are complex feedstocks, comprised of 12 and 6 different minerals, respectively, each with its own surface area, dissolution kinetics, and corresponding reactivity. Additionally, the accessibility of mineral surfaces is not considered in the reported surface areas, which can be hindered by surface passivation via carbonate precipitation that may occur throughout the experiment (Harrison et al., 2015; Hövelmann et al., 2012). Furthermore, these kimberlites contain clay minerals at 38 wt.% and 44 wt.% for GK and DVK, respectively. High clay fractions inflate BET specific surfaces, which are not representative of the target minerals, e.g., lizardite and olivine. These clays can undergo chemical and structural changes during weathering that can increase absorption and retention of CO_2 in the pore space via acid activation and ion replacement (Horri et al., 2020; Loring et al., 2012; Michels et al., 2015), thus providing a temporary influx of CO_2 potentially without a pathway for long-term storage.

The CO_2 flux measurements of GK2 showed an initial period of very high reactivity, which quickly faded to near zero by the second month of the lab phase (Fig. 3.8A). Due to instrumentation issues in the initial stages of the lab phase, no useable fluxes for GK1 were recorded; however, all other data were consistent between the two columns. The extent of pore water saturation and the mineralogy of the feedstock has shown to have the most control over CO_2 fluxes (Stubbs et al., 2022). The trends observed in GK2 are likely a combination of labile cation release from silicate sources, and carbonate dissolution driving the solubility trapping of CO_2 (Eq. 3.2). Although the intermittent measuring of fluxes may have led to parts of this reactivity being missed.

$$CaCO_3 + CO_2 + H_2O \leftrightarrow Ca^2 + +2HCO_3^- \quad (3.2)$$

This process provides short-term solubility trapping as long as the CO_2 sequestered is not allowed to precipitate and has been shown to dominate weathering systems where carbonates provide the fastest dissolution kinetics (Liu et al., 2011). Coupled with the liberation of the most labile cations, this creates the highly reactive initial fluxes observed in GK. This is supported by the buffering observed in the pH and findings of elevated DIC concentrations in the leachate of GK (Fig. 3.2). A similar result was reported by Stubbs et al. (2022), where the most negative fluxes in their kimberlite was experienced immediately after the first wetting, attributed to the loss of labile cations. The fluxes observed in WOL columns share this trend yet remain negative for the sampling duration. Again, this can be attributed to the dissolution of calcite ($CaCO_3$), which makes up 2.6% of the wollastonite skarn, as well as the liberation of labile cations. In this case however, near-zero fluxes follow the initial reactivity and become increasingly negative, eventually reaching the range of the initial fluxes. This trend may indicate the weathering of the relatively highly reactive bulk silicate after the carbonates and labile components are depleted.

Table 3.3. Weathering and carbonation reactions of target minerals found in GK, DVK, WOL, and OLI

Target mineral	Weathering reaction	Weathering products	Carbonation reaction	Carbonation products
Lizardite: $Mg_3Si_2O_5(OH)_4$	$+ H_2O$	$3Mg^{2+} + 6OH^- + 2SiO_2$	$+ 3CO_3^{2-} + 6H^+ + 9H_2O$	$3MgCO_3 \cdot 5H_2O + 2SiO_2$
Wollastonite: $CaSiO_3$	$+ H_2O$	$Ca^{2+} + 2OH^- + SiO_2$	$+ CO_3^{2-} + 2H^+$	$CaCO_3 + SiO_2 + 2H_2O$
Forsterite: Mg_2SiO_4	$+ 2H_2O$	$2Mg^{2+} + 3OH^- + SiO_2$	$+ 2CO_3^{2-} + 2H^+$	$2MgCO_3 + SiO_2 + 3H_2O$

The trends observed in the leachate chemistry of WOL are also similar to GK (Fig 3.4), yet do not clearly indicate the same silicate weathering due to the presence of Ca-carbonates. High concentrations of Ca in the initial stages that consistently decrease suggest three factors are likely contributing to this trend. Firstly, the dissolution of the highly soluble calcite is certainly contributing to the Ca concentrations observed. Secondly, labile Ca and the high reactivity of wollastonite skarn (Paulo et al., 2021) will lead to higher concentrations in initial samples. Thirdly, the fast dissolution rates of wollastonite (10^{-12} mol/cm^2/s; Pokrovsky et al., 2009) at our observed pH, which is expected to contribute more silicate weathering than other feedstocks tested. While the extent of silicate dissolution cannot be quantified through the concentrations of Ca observed in the leachate, trends in the data still show its prevalence.

Stoichiometric dissolution of wollastonite results in a 1:1 ratio of Ca and Si release (Table 3.3), allowing the moles of Si in solution to be used as a proxy for the release of Ca that may be removed from solution through $CaCO_3$ precipitation (Wood et al., 2022). While the stoichiometric dissolution of wollastonite may be expected given the pH observed and the duration of this study (Schott et al., 2012), the Si:Ca was <1 in reservoir waters, meaning more Ca is being released than Si. Explanations for this result include Ca contributions from minerals other than wollastonite, like calcite and diopside, although diopside has a dissolution rate three orders of magnitude slower than wollastonite (10^{-15} mol/cm^2/s; Declerq and Oelkers, 2014). Additionally, Si is likely being retained in the column as amorphous precipitates on mineral surfaces, as a consequence of its saturation index (Table 3.2). The ratio of Si to Ca in the reservoir after the outdoor phase, while still far less than 1, is significantly closer than after the lab

phase, which could be due to a combination of the loss of carbonates, and Ca being precipitated within the column. Evidence to support this can be seen in calcite and aragonite saturation in the reservoir waters (Table 3.2) and the increase in the columns TIC (Fig. 3.12), leading to the assumption that we are not moving towards stoichiometric dissolution rather the Ca is being retained in the column via secondary carbonate precipitation. Wood et al. (2022) shares the findings of Ca retention in their columns, but to an extent where the ratio of Si to Ca is >1. This is explained by the low initial TIC values and the purity of the wollastonite used by Wood et al. (2022). Thus, further exemplifying the complications of monitoring and assessing impure yet more realistic feedstocks.

The OLI material, containing 92 wt.% forsterite, lacked carbonates, and therefore was dominated by silicate dissolution. The ratio of Si to Mg released favours Mg in both reservoir leachates, indicating non-stoichiometric dissolution. This result can be explained by the release of labile cations, similar to what was observed in WOL, yet this trend is not as clearly defined in the discrete samples (Fig. 3.5). Labile Mg release has been well documented in olivine, with Lu et al. (2022) reporting 1–6% of total Mg^{2+} being considered labile, dependent on chemical conditions and reaction time. Despite comprising a minimal fraction compared to the total Mg^{2+}, labile components may still significantly impact olivine dissolution (Lu et al., 2022). Nevertheless, there was comparatively low Mg release in the discrete and bulk leachate (Fig. 3.5) despite the presence of labile Mg^{2+} and the fast dissolution rates as a result of being an unpolymerized silicate (De Baere et al., 2015). This can likely be attributed to the coarse grain size (D50; 423 μm) and resulting low surface area (0.24 m^2/g) of the olivine sand

used, which has been shown to significantly impair the dissolution rates of olivine (Oelkers et al., 2018). An estimated grain size of <10 μm is required for olivine to completely dissolve in seawater over one hundred years (Hangx and Spiers, 2009), while a particle size of 0.1–0.01 μm reaches the same result in five years when applied to soil (Renforth et al., 2015a). A symptom of the coarse grain size used in OLI columns is the lack of water residence time which results in limited fluid-rock interactions. Thus, the grain size used in our study is significantly larger than what has been proposed for requisite dissolution.

A loss of TIC was observed across the entire OLI columns. However, the change occurred at such a small scale, that it may be within error. Although, it is likely that no secondary carbonates formed as a result of poor precipitation kinetics, resulting in a net-zero change in TIC. The smaller size of the Mg^{2+} ions in relation to Ca^{2+} inhibits their precipitation, with rates of anhydrous Mg-carbonate precipitation being 4–6 times slower than most Ca-carbonates (Saldi et al., 2009). As a result of this, hydrated Mg-carbonates like hydromagnesite are kinetically favoured (Hänchen et al., 2008), with its precipitation being documented in the ambient temperatures and pressures observed in this study (Hamilton et al., 2021; Lechat et al., 2016; Power et al., 2009; Turvey et al., 2018; Wilson et al., 2014, 2009). Despite this, no TIC additions were observed in OLI columns (Fig. 3.12 D), due to significant undersaturation of hydrated Mg-carbonates in solution (Table 3.2). The extent of Mg-carbonate saturation governs the ability for nucleation to occur (Giammar et al., 2005), with precipitation rates increasing alongside saturation states (Saldi et al., 2012). Grain size may also influence the extent of Mg-carbonate precipitation, with Giammar et al. (2005) finding a reduction from 125-250 μm (0.088

m^2/g) to 250-50 µm (15 m^2/g), resulting in an exceedingly greater extent of precipitation of magnesite. The large grain size and low surface area of the OLI used in our columns likely contribute to the lack of silicate dissolution, and lack of secondary carbonate precipitation observed in this study.

DIC in the OLI and DVK leachates far exceeds the two other column types. Despite the similar DIC concentrations found in OLI and DVK, the former is likely provided by silicate weathering, while the latter is produced by carbonate dissolution. Evidence for this can be seen in the TIC data (Fig. 3.12 A, B), which shows little change in OLI, and a substantial TIC loss in DVK. While carbonate dissolution may be occurring in the OLI columns, it is expected to contribute significantly less, as the change of TIC was <0.01%. DIC additions, regardless of source, are a net positive for DVK as long as secondary precipitation is not allowed to occur, which may pose a challenge considering the supersaturation of aragonite and calcite in the reservoir waters (Table 3.2). The supersaturation of these Ca-carbonates in leachate from a feedstock containing no significant Ca-silicate sources (Table 3.1) is further evidence of carbonate dissolution dominating DVK. Conversely, the DIC in OLI is likely from silicate weathering and has been documented as a primary source of olivine's sequestration capacity (Amann et al., 2020; Montserrat et al., 2017).

The CO_2 fluxes of OLI and DVK illustrate the challenges and limitations of monitoring less reactive feedstocks, including missing CO_2 drawdowns during periodic rainfall events which have been shown to initiate dissolution and drawdown of CO_2 (Stubbs et al., 2022). Measuring CO_2 fluxes of DVK was hindered by significant water pooling at the surface of the column as a result of swelling clays that comprise 44 wt.%

of the kimberlite residues. Measuring fluxes when the columns are in this state would not have provided accurate data, which occurred for nearly half of the outdoor phase (Fig. 3.9) as a result of significant precipitation in the Fall of 2021 (Fig.3.1). The effect of these clays caused water retention to be at >80% for most of the experiment. While OLI did not miss any measurements due to pooling, the interval between measurements may have been too large and resulted in missed drawdown. Negative fluxes were measured shortly after the water additions during the lab phase, yet these were not consistent, and fluxes became positive as the olivine sand dried (Fig. 3.11). Stubbs et al. (2022) reported similar results that suggest all CO_2 drawdown measured was stored as a dissolved phase when the material was at its highest saturation, which led to degassing as evaporation occurred. Our results agree with this finding, as both OLI columns only experienced negative fluxes at their most saturated, followed by rapid degassing and positive fluxes.

The release of deleterious metals and nutrients

Feedstock weathering resulted in low amounts of Ni and Cr being released from all columns on a per-mass basis. However, most columns show a higher release of Ni and Cr on a per-mass basis during the outdoor phase, which may indicate their presence in the bulk silicate rather than carbonates or labile components. Columns containing DVK released relatively higher amounts of Ni and Cr despite only experiencing the outdoor phase. Significantly more Ni was released than Cr in all columns, despite comprising similar concentrations in most samples whole rock geochemistry. The Ni that is mobilized via weathering is often a stable form with high mobility in aqueous solutions (Ni^{2+}), compared to less soluble sates of Cr that are released and governed by their

oxidation states (Kabata-Pendias, 2000), resulting in the discrepancy between values observed in this study.

The release of Ni and Cr is an important consideration for the selection of ERW feedstocks (Beerling et al., 2018; Flipkens et al., 2021; Haque et al., 2020a). This assessment must be done on a case-by-case basis and should consider factors such as the rate of application (Haque et al., 2020a; Vasiluk et al., 2019), long-term effects on crops and native flora (ten Berge et al., 2012), and soil parameters including organic content, clay fractions, physical attributes, pH, and redox potential, which have all been shown to affect bioavailability and mobility of Ni and Cr in soils (Kabata-Pendias, 2000; McClain and Maher, 2016; Smolders et al., 2009; Soubrand-Colin et al., 2007). Thus, for meaningful determinations of a feedstocks safety to be made, columns must be constructed in a way that simulate the environment feedstocks are being applied to i.e., including soils in columns.

Amending depleted soils with mineral fertilizers, including olivine and wollastonite, can improve crop yields, and increase food security (Amann et al., 2020; Anda et al., 2015, 2013b; Dietzen et al., 2018; Haque et al., 2020c, 2019; L. L. Taylor et al., 2021; Van Straaten, 2006). In this study, there was minimal release of K from WOL while providing the most P compared to all columns. In comparison, there was relatively high K and P releases from OLI. Moreover, all feedstocks were able to buffer the pH of water additions from ~5.6 to >7, which can improve the health of mildly acid soils (Kantola et al., 2017) and decrease N_2O emissions in croplands (Islam et al., 2006; Nunes et al., 2014; Shaaban et al., 2014). However, a drawback to the widespread application of ERW feedstocks to agricultural soils is the possibility of permeability

changes that may occur due to accumulation of mineral phases with slower weathering rates (Andrews and Taylor, 2019). This issue could be made worse by the formation of secondary carbonates, which is well documented in our WOL samples (Fig 3.12). As a result, particle movement and loss could be experienced via overland flow, limiting the impacts of potential nutrients released via ERW (Andrews and Taylor, 2019).

3.4.2 CO_2 removal and carbon accounting

The two pathways identified for CO_2 sequestration via ERW are solubility trapping and mineral trapping, whereby CO_2 is stored as a dissolved phase (e.g. HCO_3^-) and stable carbonate, respectively (Gilfillan et al., 2009). The dissolution and dissociation of $CO_{2(g)}$ into waters (Eq. 3.3) forms carbonic acid (H_2CO_3; Eq. 3.4), which results in the formation of bicarbonate (HCO_3^-; Eq. 3.5) or carbonate ions (CO_3^{2-}; Eq. 3.6) when consumed by the neutralization of a solid base (Power et al., 2013).

$$CO_{2(g)} \leftrightarrow CO_{2\,(aq)} \tag{3.3}$$

$$CO_{2\,(aq)} + H_2O \leftrightarrow H_2CO_3 \tag{3.4}$$

$$H_2CO_3 \leftrightarrow H^+ + HCO_3^- \tag{3.5}$$

$$HCO_3^- \leftrightarrow H^+ + CO_3^{2-} \tag{3.6}$$

Furthermore, the dissolution products resulting from the buffering of carbonic acid for solubility trapping can also be used in the formation of a solid carbonate mineral, resulting in mineral trapping of CO_2 (Eq. 3.7; Mitchell et al., 2010).

$$Ca^{2+} + CO_3^{2-} \leftrightarrow CaCO_3 \tag{3.7}$$

In our study, solubility trapping is calculated using the measured concentrations of DIC in the leachate, representing the total carbon additions as a dissolved phase. Rates

of solubility trapping were calculated for each column using Equation 3.8 and averaged between the duplicate columns:

$$Solubility\ trapping\ (g\ CO_2/kg) = \frac{\left(\frac{DIC}{1000} \times V\right) \times \frac{M_{CO_2}}{M_C}}{m} \quad (3.8)$$

where DIC is the concentration (mg/L) measured in reservoir samples, V is the total water volume that passed through the column (L), M_{CO2} and M_C are the molar masses of CO_2 and C, respectively, and m is the mass of the column (kg). Mineral trapping of CO_2 was calculated based on the ΔTIC of the solids using Equation 3.9, and averaged between duplicates:

$$Mineral\ trapping\ (g\ CO_2/kg) = \frac{\left(\frac{\Delta TIC}{100} \times m\right) \times \frac{M_{CO_2}}{M_C}}{m} \quad (3.9)$$

where ΔTIC is the change of TIC (%) between the initial and final solids, M_{CO2} and M_C are the molar masses of CO_2 and C, respectively, and m is the solid mass in the column. The CO_2 removal rates via solubility and mineral trapping are summarized in Table 3.3.

Table 3.4. Average (n=2) CO_2 sequestration rates (g CO_2/kg) based on changes observed in DIC (solubility trapping) and TIC (mineral trapping) for each column. Positive values indicate the storage of CO_2, while negative values indicate the loss of CO_2 from the material.

	Solubility trapping (g CO_2/kg)	Mineral trapping (g CO_2/kg)	Total sequestration (g CO_2/kg)
GK	0.03 ± 0.001	0.59 ± 0.1	0.62 ±0.1
DVK	0.06 ± 0.001	-3.18 ± 0.8	-3.12 ± 0.7
WOL	0.04 ± 0.006	6.27 ± 0.76	6.31 ± 0.8
OLI	0.49 ± 0.003	-0.53 ± 0.01	-0.04 ± 0.02

CO_2 fluxes were also used to assess CO_2 removal rates by integrating the area under the curve for Figures 3.8 – 3.11. These rates underestimated carbon additions measured

using TIC and DIC data, reporting 39% and 36% of the values of GK and WOL, respectively. Furthermore, the fluxes indicate more favourable results for DVK, although these still report a net efflux of CO_2, while OLI is seen to result in a loss of CO_2. This method is limited by the measurement interval, which was not optimized to capture all reactions over the 1-year duration of the experiment, and therefore, resulted in inconclusive rates. Moreover, the low reactivity of some feedstocks analyzed led to a lack of signal produced from desirable sources, and influence of diurnal temperature fluctuations, further invalidating these results (Stubbs et al., 2022).

Gahcho Kué residues

CO_2 removal using the GK residues was dominated by mineral trapping, which accounted for 96% of the total. Specifically, TIC equated to 0.97 ± 0.2 g of C in each column, indicating secondary carbonate formation. Although TIC increased in the upper 8 cm of the column, the greatest gain was in the bottom layer (14–18 cm). TIC increases at the surface may be caused by the evapoconcentration of carbonate-forming ions (e.g. Ca^{2+} and CO_3^{2-}), resulting in carbonate precipitation (Stubbs et al., 2022). Efflorescence formed by evaporation of process waters have been documented at mines with arid climates (Bea et al., 2012; Wilson et al., 2014) and in experiments where the material has been allowed to dry (Acero et al., 2007). TIC accumulation in the bottom layer may be due to surface carbonate dissolution and precipitation at depth. For instance, the reservoir waters were saturated with respect to calcite, indicating the potential for further carbonate precipitation.

Favourable conditions for precipitation limited solubility trapping from becoming a significant source of CO_2 sequestration for GK columns. The lack of pore water

sampling is a limitation of this column design, which may have revealed higher DIC in pore water before it precipitated at depth. In which case, thinner layers would be more adept for solubility trapping. Stubbs et al. (2021) found that maximum CO_2 drawdown would be achieved when kimberlite was deposited at a depth of 8.5 cm in a system that is dominated by the reaction of labile cations and resulting solubility trapping. In theory, the efficacy of CO_2 sequestration can be improved by an increase in the fluid:rock ratio (Stubbs et al., 2022), which can be realized by dispersing feedstocks over larger areas (Renforth, 2012; Schuiling and Krijgsman, 2006). Regardless of the depth of deposition as determined by a mine waste storage plan, or per recommendations for enhancing reactive mineral exposure, the conditions can be simulated in our columns to provide a monitoring tool for determining rates of CO_2 sequestration.

CO_2 sequestration rates of kimberlite residues have been determined through various methods including reactivity tests (Paulo et al., 2021), CO_2 flux measurements (Stubbs et al., 2022), and quantitative XRD coupled with radiocarbon isotopic analysis (Wilson et al., 2011), yielding various results. The complex mineralogy of kimberlite makes comparison challenging, requiring individual assessment for each sample. For example, Paulo et al. (2021) predicted CO_2 sequestration potentials of kimberlite residues from the Venetia Diamond Mine in the range from 0.1–9 kg CO_2/t, based solely on the easily extractable cations from non-carbonate sources. The results of this study are on the lower end of that range, with a rate of 0.6 ±0.1 kg CO_2/t. Similarly, converting the results of GK columns into a CO_2 removal rate on a per area per year basis equates to 121 ±19 g $CO_2/m^2/yr$, which is within the range determined by Stubbs et al. (2022) who reported CO_2 removal rates of approximately 100 g $CO_2/m^2/yr$. GK has the potential to offset 3.7–

11.8% of the mine's emissions annually, according to Zeyen et al. (2022), who calculated the carbonation potential based on the Mg and Ca released via cation exchange precipitating as hydromagnesite and calcite, respectively. Furthermore, their study found that smectite-rich kimberlites that are carbonate-poor have the greatest potential for CO_2 sequestration via cation exchange.

The columns in this study were successful in measuring CO_2 removal rates using Gahcho Kué kimberlite given their moderate reactivity due to reactive phases, low carbonate content, and potential to precipitate secondary carbonates. However, most research into the CO_2 sequestration of kimberlites is based largely on laboratory and desktop studies, with no published works that include monitoring CO_2 fluxes in large-scale field trials currently. However, significant research has been conducted into the passive weathering rates of kimberlite residues at diamond mines, and how they can be enhanced (Power et al., 2014; Stubbs et al., 2022; Wilson et al., 2011). For example, Wilson et al. (2009) determined that silicate weathering of kimberlite wastes at the Diavik Diamond Mine is responsible for sequestering 102–114 g CO_2 /m^2/yr via passive weathering.

Applying the rate of CO_2 sequestration observed in our columns (0.62 kg CO_2/t) to the 0.91 Mt of residues that Gahcho Kué produces each year (Mervine et al., 2018), 0.67 % of the mine's annual 0.084 Mt of CO_2 emissions would be offset. However, dispersal of residues at a scale of 102 ha would result in the offset of 10% of annual emissions.However, these findings do not consider the climatic conditions of the mines, the depth of residue deposition, or their saturation and therefore do not accurately represent processes occurring at the mine site. Yet, we show that coupling these columns

with large-scale deployment of GK kimberlite in an enhanced weathering scenario or passive weathering monitoring system would allow for validation of CO_2 sequestration.

Venetia Diamond mine kimberlite

The results of the DVK columns illustrate some of the issues faced when determining rates of CO_2 sequestration via enhanced weathering. Zero CO_2 sequestration was observed in DVK columns, despite evidence that this feedstock has the capacity to sequester 5 kg CO_2/t based on easily released cations from non-carbonate sources, as reported by Paulo et al. (2021) and confirmed by chapter 2 of this thesis. Moreover, Stubbs et al. (2022) determined a sequestration rate of ~550 g $CO_2/m^2/yr$ for DVK by measuring direct fluxes of CO_2 at the surface. Therefore, the loss of CO_2 reported in Table 3.4 likely is not a symptom of poor feedstock selection, but rather issues with instrumentation and experiment design.

The loss of initial TIC without the precipitation of secondary phases results in the net loss of CO_2 for these columns. However, the loss of primary carbonates equates to the release of 0.43 moles of Ca which would require ~3400 mg Ca/L to be found in the leachate, or 113 times what was actually observed. Therefore, it is possible that Ca is being precipitated somewhere within the system that wasn't accounted for. One potential explanation is that "missing" Ca was precipitated on the walls of the reservoir, within the discrete sampling cup, inside the fiberglass wicks, or on the column walls. The supersaturation of both calcite and aragonite is evidence for unobserved precipitates in DVK (Table 3.2), which were the highest SI's observed for each mineral in this experiment.

Despite success in determining rates of CO_2 sequestration in GK kimberlite, DVK can be viewed as a failure. However, modifications to the column and experimental design could lead to reliable rate determination for this feedstock in the future. For example, more comprehensive TIC sampling may reveal secondary carbonate precipitation outside of the bulk feedstock. Moreover, the implementation of porewater samplers could allow for a higher level of monitoring in feedstocks like DVK which did not provide much drainage water. Finally, as columns are deployed to monitor ongoing CO_2 sequestration efforts, they will likely be subject to different parameters that reflect the environment they are monitoring, thus leading to different results than what was experienced in this study.

Wollastonite skarn

The majority of the CO_2 sequestered through the WOL columns resulted from carbonate precipitation. TIC additions were observed throughout the column but reduced as depths increased (Fig. 3.12 C). The sequestration rate observed for WOL equates to 6.3 g CO_2/kg, yet the rate for the upper 4 cm was 8 g CO_2/kg. Therefore, spreading the same column mass (6 kg) in a 4 cm layer would have increased the sequestration rate via mineral trapping from ~1200 to ~1600 g CO_2/m^2/yr. Reactions are likely occurring to a greater extent near the surface of WOL columns where the pH of the water has yet to be buffered, and CO_2 is more available. Additionally, evapoconcentration of cations released via those processes during the drying periods allows precipitation to occur more near the surface. Furthermore, the saturation of calcite and aragonite in the leachate shows the potential for precipitation to occur throughout the column (Table. 3.2). The contributions of solubility trapping were not significant, equalling 0.04 g CO_2/kg or 0.5% of the total

rate observed. This is a consequence of favourable carbonate precipitation conditions, not a result of the lack of weathering products.

CO_2 removal rates by wollastonite weathering have been determined in laboratory experiments and large-scale field studies. Determinations of CO_2 sequestration potential based on easily accessible cations from non-carbonate sources conducted in chapter 2 and by Paulo et al. (2021) show the ability of wollastonite skarn to remove 35 kg CO_2/t, which is significantly more than the rates of 6.3 ±0.8 kg CO_2/t determined in this study. Discrepancies between the potential observed by Paulo et al. (2021) and our findings indicate that there are opportunities to improve the sequestration via enhancements (i.e. reducing the grain size, amendments, and thin dispersal). Column experiments conducted by Wood et al. (2022) used the wollastonite from the same mine as this study, but also included treatments that were mixed with soil. The authors determined a CO_2 removal rate of 255 kg CO_2/t, far exceeding this study's estimates. However, Wood et al. (2022) observed a sequestration rate of 667–1820 g CO_2/m^2/yr in their columns containing wollastonite and water alone, which is in close agreement with our results of 1244 ±148 g CO_2/m^2/yr and is a more apt comparison. Lab (Haque et al., 2019) and field studies (Haque et al., 2020) can yield contrasting results, with measured rates of 3930 and 20–24 g CO_2/m^2, respectively, which emphasizes the need for high resolution monitoring of field sequestration rates. Wollastonite amended to the Hubbard Brooke Watershed by Taylor et al. (2021) produced a sequestration rate of 7– 38 g CO_2/kg, which is slightly above the rate observed in WOL columns which was 6.3 CO_2/kg. Higher rates reported by Taylor et al. (2021) may be attributed to the dominance of solubility trapping in their system, which has a 1:2 Ca:C ratio, while in our columns, 99.5% of the CO_2

sequestration was attributed to the precipitation of secondary carbonates. However, both Haque et al. (2020) and Taylor et al. (2021) only considered one stream of sequestration, which is a challenge of monitoring the carbon budget at the scale of an entire watershed, or agricultural field, that can be mitigated through the use of drainage columns.

Leaching columns are suitable for monitoring the weathering of wollastonite skarn as shown by the ease at which CO_2 sequestration rates were determined in this study. Wollastonite weathering is relatively rapid, releasing Ca^{2+} and buffering pH, resulting in calcite formation. The most significant challenge encountered using wollastonite skarn in these columns is the lack of solubility trapping, which is easier to quantify than mineral trapping as it does not require dismantling the column. Coupling our methodology with large-scale ERW trials would require the implementation of multiple replicate columns that allow for their destruction to quantify mineral trapping.

Olivine sand

The results of the OLI columns illustrate the issues faced when monitoring the CO_2 removal using feedstocks with low reactivity. Solubility trapping through olivine weathering was the greatest amongst the materials tested, which is consistent with other enhanced weathering field trials (Hangx and Spiers, 2009; Montserrat et al., 2017; Renforth et al., 2015a). However, the results of mineral trapping show that the dissolution of primary carbonates resulted in a net loss of CO_2 (Table 3.4). As a result, the rate presented indicates that the spreading of olivine would, in turn, release more CO_2 than it can sequester. In reality, this is likely not the case and is a consequence of a small amount of carbonate weathering, overshadowing the low reactivity of the feedstock. Additionally,

the ΔTIC may be so insignificant that it falls within the error of the method, resulting in solubility trapping being the only pathway for CO_2 sequestration. The olivine used in this study has a D50 particle size of 423 μm and a resulting surface area of 0.2 m^2/g, significantly hindering the sequestration results observed. Rinder and von Hagke (2021) estimate that a grain size of <10 μm is required for a significant drawdown of CO_2 in forsterite-rich basalt, reinforced by Hangx and Spiers (2009), who claim that the same grain size is required for the complete dissolution of olivine in seawater over 100 years. Moreover, a particle size of 0.01–0.1 μm is needed for complete dissolution within five years of olivine application to soil (Renforth et al., 2015a). We are not experiencing the reactivity required to offset the loss of primary carbonates, however small, due to the insufficient grain size and surface area. Moreover, no carbonate phases were identified, and initial TIC was present at 0.01 ± 0.006%, which was nearly all lost to dissolution. It can be assumed that the dissolution of these carbonates influenced the solubility trapping, which resulted in the conversion of carbon present as a primary carbonate to a dissolved phase at a 1:1 ratio (Eq. 3.2).

The maximum CO_2 sequestration (R_{CO2}; Eq. 3.10) for the olivine used in this study can be calculated assuming complete carbonation of CaO and MgO at a 1:1 molar ratio (Renforth, 2012).

$$\mathrm{R_{CO_2}} = \frac{M_{\mathrm{CO_2}}}{100}\left[\left(\frac{\%\mathrm{CaO}}{M_{\mathrm{CaO}}} + \frac{\%\mathrm{MgO}}{M_{\mathrm{MgO}}}\right) - molC_{TIC}\right] \times 1000 \tag{3.10}$$

Where M_{CaO}, M_{MgO}, and M_{CO2} represent the molar masses of CaO, MgO, and CO_2, respectively, and $molC_{TIC}$ represents the mols of TIC present in the sample. Based on Eq 3.10, the olivine used in our study has the potential to sequester 545 kg CO_2/t. Despite

such a high sequestration capacity, we observed that 0% of this capacity was met. Consequently, alterations to the physical characteristics of this feedstock must be made. However, a decrease in the efficiency of a feedstock to sequester CO_2 may be observed with an increase in pre-treatment energy costs (Rinder and von Hagke, 2021). Thus, further investigation is required.

3.4.3 Implications

Carbon accounting and drainage monitoring at mine sites

Passive carbonation of alkaline residues occurs via weathering under ambient conditions, resulting in the formation of secondary carbonate minerals, often as efflorescent crusts, hardpans, and coatings on cobbles (Power et al., 2013; Wilson et al., 2009). Passive carbonation has been documented within ultramafic tailings across a range of deposit types (Entezari Zarandi et al., 2016; Gras et al., 2017; Stubbs et al., 2022; Turvey et al., 2018; Wilson et al., 2014, 2009). Passive carbonation rates at chrysotile, diamond, and nickel mines are 2–5 orders of magnitude greater than natural weathering rates in river catchments (Power et al., 2013). Furthermore, these rates can be accelerated to increase CO_2 sequestration through modifying tailings management practices. Quantifying weathering and CO_2 sequestration rates in mine residues has been done using large-scale sampling followed by quantitative XRD (Turvey et al., 2018; Wilson et al., 2014, 2011) and isotopic data (Gras et al., 2017), and CO_2 flux measurements (Stubbs et al., 2022). However, scaling these methods for field application remains challenging. For example, Wilson et al. (2014) required nearly 1000 samples to estimate the passive carbonation via quantitative XRD at the Mount Keith Nickel Mine in Western Australia.

The columns employed in our study allow the monitoring of passive and accelerated weathering rates at a mine site without the need for large-scale sampling and interference with site operations. Deploying multiple columns would allow for their periodic deconstruction for solid sampling and analysis while water and gas sampling remains continuous. Our results emphasize the importance of tailoring the monitoring approach to the feedstock characteristics, in particular its reactivity. As such, the design of the columns does not rely on a single variable for rate determination, making them a flexible tool. Furthermore, these columns can monitor drainage chemistry to assess impacts on water quality, including the release of heavy metals, e.g., Ni and Cr. While this is not currently of concern for most mine sites, as they often have extensive water chemistry monitoring plans already in place and use impoundments designed to limit the feedstock exposure and weathering. However, this practice should allow for more weathering by dispersing the feedstocks onsite or offsite more widely (Stubbs et al., 2022), generating the need for advanced monitoring systems. Furthermore, the release of potential nutrients like P and K is not very important in mine residues due to barriers, including public perception, the spread of indicator minerals, and the potential loss of unrecovered ore (Krüger, 2007).

Implications for CO_2 sequestration at Gahcho Kué

Applying the CO_2 removal rates reported in this study to the scale of the Gahcho Kué Diamond Mine can be used to estimate the potential for reducing emissions during and after the mine's operational life (Fig. 3.14). After the mine's life span in approximately 2030, an estimated 15.5 Mt of fine processed residues will have been

generated, resulting in 1.8 Mt CO_{2e}. According to the rate determined in this study, 4.5% of the mine's emissions will have been offset by the time the mine closes. This estimation assumes that every tonne of residues will sequester 620 g CO_2 per year as the residues are generated. The consumption of reacting minerals in the residues is negligible and therefore ignored in this estimation. After the life of mine, Gahcho Kué will be placed under care and maintenance, a common practice of De Beers. Projecting these rates past the life of the mine indicates that 10% of the mine's greenhouse gas emissions will be offset by 2040, 25% by 2068, and 50% by 2114. However, this rate may vary depending on residue deposition practices, climatic conditions, and other variables. In our study, residues were only 17 cm thick, while the yearly production of 1.12 Mt of residues requires ticker depositions, given the mine's current practices. Additionally, these columns were exposed to the climate of Southern Ontario in the summer, and room-temperature conditions in the winter, leading to year-round weathering, which would not be the case in the Northwest Territories. As such, the CO_2 sequestration at Gahcho Kué has been calculated at rates representing 0.5× and 2× what was observed in this study. At twice the rate, 10% of the mine's emissions would be offset before closure, while this target would take ~100 years to reach at half the rate. Potential offsets are highly sensitive to rate changes and must be assessed at the mine site and monitored closely. In order to achieve the higher rates outlined in Figure 3.4, large-scale trials should be considered, which would increase the area of dispersal and therefore result in more residues being exposed for reactions. In addition, deploying monitoring apparatus like these leaching columns at the mine site would allow for more accurate determinations of rates which reflect changes to deposition practices and climatic conditions. Regardless,

significant CO_2 sequestration is expected to occur past the lifespan of the mine in all three scenarios, emphasizing the importance of the long-term monitoring our columns can provide.

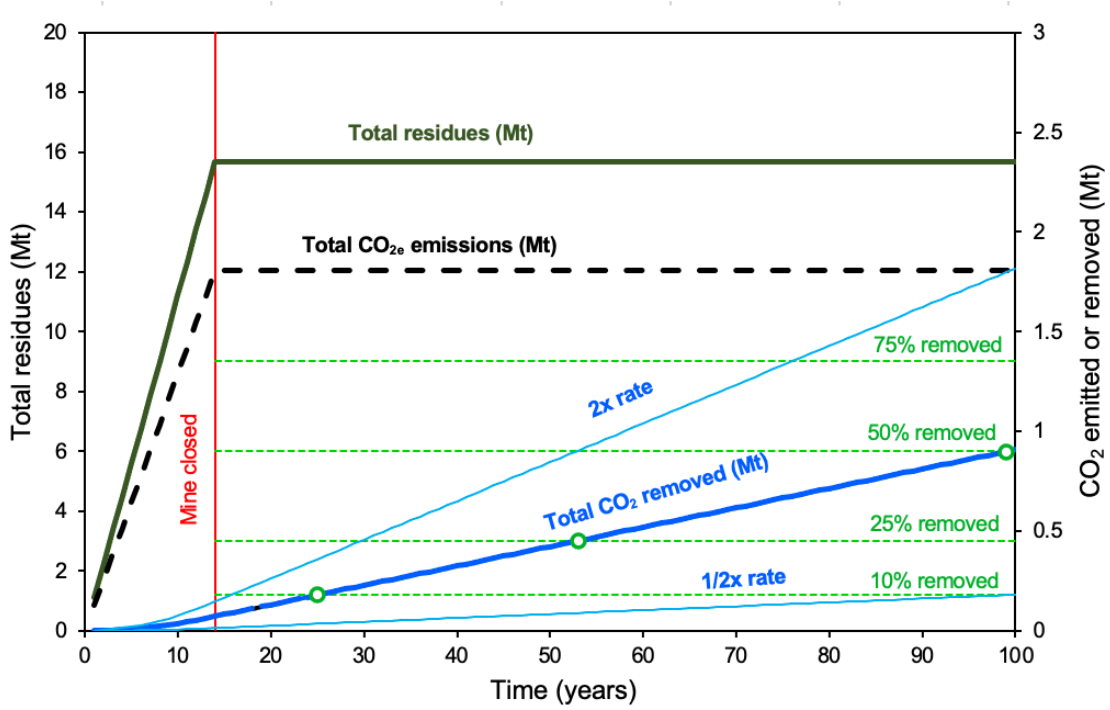

Figure 3.13. Forecasted CO_2 sequestration at the Gahcho Kué Diamond mine, based on the rates reported in this study and publicly available mine operations data.

Carbon accounting and drainage monitoring in ERW trials

Enhanced rock weathering relies on the same processes as passive carbonation of mine wastes but is accelerated by the large-scale dispersal of mafic and ultramafic feedstocks. ERW requires relatively low land use changes in contrast with other negative emissions technologies (Smith et al., 2016), with applications to farmland requiring minimal production interruptions. However, modelling studies have shown that up to 50% of a country's arable land would need to be treated with crushed feedstocks to make significant impacts on global CO_2 concentrations (Beerling et al., 2020; Renforth, 2012).

As such, certain methodologies used for assessing CO_2 sequestration in mine residue impoundments, like quantitative XRD, may not be economically or practically feasible at this scale. In addition, spatial variabilities across large-scale environments would complicate carbon verification tools that rely on representative sampling. For that reason, coupling the widespread application of ERW feedstocks with apparatus designed to replicate a scaled-down version of the process should be preferred.

Accurate carbon verification is necessary for the success of ERW as a NET, as it will provide feedback on the system's realization of forecasted carbon additions. The significance of accuracy in ERW trials stems from the common overestimation of rates in modelling and laboratory studies compared to the real world. Additionally, accurate carbon verification can aid in carbon pricing scenarios, which would become a driving force behind the widespread adoption of NETs (Honegger et al., 2021).

The release of potential nutrients and deleterious metals is an important consideration for ERW, as opposed to mine wastes, which are often contained and already monitored. While measures should be taken to characterize feedstocks and determine their expected element release, there are several site-specific parameters that govern the fate of these elements. Therefore, monitoring these elemental releases in conditions replicating the application site become critical. Additionally, monitoring the beneficial release of P and K can assist in decision-making in agriculture that would allow for the optimization of nutrient delivery systems.

Table 3.5. Summary of carbon verification methods, including their advantages, disadvantages, and examples of how each affected result

Carbon verification method	Advantages	Disadvantages	Examples from this study
Total inorganic carbon	▪ Absolute measure of solid inorganic carbon ▪ Quantifies amorphous carbonates	▪ Establishing accurate initial values is challenging ▪ Primary vs. secondary carbonate distinction is difficult ▪ Does not account for carbon stored as a dissolved phase	✓ TIC changes were conclusive for GK and WOL due to high reactivity and favourable conditions for precipitation. × Inconclusive results for DVK, and OLI due to high initial C and low reactivity, respectively.
Dissolved inorganic carbon	▪ Easily accessible and does not require significant disturbances to a system. ▪ Analyzing waters provides information on cation release, including nutrients and metals	▪ Does not account for carbon stored as a solid phase ▪ Cannot be used to distinguish DIC sources, e.g., carbonate dissolution versus atmospheric CO_2 uptake ▪ Requires strong knowledge of hydrology and water balance of system	✓ DVK and OLI provided strong evidence of solubility trapping despite loss of primary carbonates. × Sequestration provided by GK, and WOL would be insignificant measuring DIC alone.
CO_2 fluxes	▪ Real-time measurement of CO_2 drawdown or release ▪ Can be automated	▪ Does not determine the fate of carbon ▪ Accuracy limited by measurement interval. ▪ Detection limited may be inadequate for low reactivity feedstocks	✓ WOL yielded strong, negative fluxes, but was still hampered by measurement interval. × GK lacked the reactivity to sustain reliable fluxes. × DVK, and OLI were limited by lower reactivity.

Analysis of carbon verification tools

Total inorganic carbon

Verifying CO_2 sequestration via TIC changes is a robust and reliable method that provides an absolute measure of carbon additions to a system (Table 3.4). Measurements of TIC content allow a direct determination of CO_2 sequestration via mineral trapping. Furthermore, this method allows for the quantification of carbonates that are present at <5 wt.%, which are difficult to identify via XRD due to their poor crystal structure and low abundance (Wilson et al., 2011). However, this method can be limited by the ability to

determine an initial TIC content, i.e., a baseline, in large-scale, spatially variable environments. The accuracy of baseline TIC values is contingent mainly upon feedstock heterogeneity and sampling scale. Failure to determine an accurate initial TIC content can result in either over or underestimating rates determined via ΔTIC (Paulo et al., 2021).

Inaccurate estimates of CO_2 removal rates using TIC can be mitigated through several practices, with their applicability being based chiefly on the feedstock and the setting. The two most definitive ways to ensure carbonate dissolution does not occur are to select feedstocks with zero TIC or to remove carbonates from a feedstock via pre-treatment. Both options are impractical because of the prevalence of TIC in feedstocks with no identifiable carbonates, as outlined in our study by the results of olivine. However, chemical pre-treatment can resolve this, but without low-cost processes available, making it an unappealing option (McKelvy et al., 2005). Consequently, the most realistic pathway for dealing with carbonate dissolution is not mitigation but rather a combination of prediction and monitoring. Thus, the columns employed in this study are a valuable tool for differentiating between carbonate and silicate weathering when coupled with characterization methods.

Dissolved inorganic carbon

Similar to monitoring TIC, DIC measurements are an absolute measure of carbon additions via solubility trapping of CO_2 (Table 3.4). Furthermore, DIC can be measured without disturbing solids, such as in this study's use of drainage columns. This method requires a strong understanding of the hydrology and water balance of the system. In other words, the total amount of water that stores the DIC must be known. The drainage columns simplify the hydrology by collecting rainwater and draining into a reservoir for

measurement. A benefit of this method over TIC is that its success is not as contingent upon establishing an initial value, resulting in less overestimation. Moreover, background concentrations of DIC and other water parameters are often monitored already. However, a drawback to this method is the determination of sources of HCO_3^- which can complicate the carbon budget. This is observed in the DVK and OLI columns, which showed a loss of carbonate and significant DIC concentrations. As such, it is unknown if the high DIC concentrations observed in DVK and OLI yielded a net gain of C-additions to the system without analysis of carbonates. This emphasizes the importance of a multi-faceted approach to carbon verification.

CO_2 fluxes

Direct measurements of CO_2 fluxes determine a rate of change in CO_2 concentrations that equate to a diffusion rate to be used in calculating a feedstocks sequestration. CO_2 fluxes have proven to be a valuable tool for verifying carbon removal in various mine wastes and rock powders (Stubbs et al., 2022). However, it requires near-continuous monitoring and has only been employed over short timeframes. Our results show the importance of measurement intervals that allow feedstock reactivity to be adequately observed. Failure to do so results in inconsistent and inconclusive CO_2 sequestration rates, as seen in WOL columns. Furthermore, using CO_2 flux measurements is not well suited to feedstocks with low reactivity, whether due to their geochemical composition, mineralogy, or physical attributes. As such, we could not observe the drawdown of CO_2 into GK, DVK, and OLI, despite evidence of its occurrence as a dissolved and solid phase.

3.5 Conclusion

Alkaline mineral feedstocks can sequester CO_2 as a dissolved or solid phase through ERW. However, the rate at which this occurs can vary greatly, requiring high-resolution monitoring to verify carbon additions to a system. Field-deployable leaching columns are capable of determining rates of CO_2 sequestration using multiple tools for carbon verification, including DIC, TIC, and direct measurements of CO_2 fluxes. Each method proved useful for overcoming challenges posed by the feedstocks, yet no method could provide a reliable sequestration rate alone. Using the ΔTIC was an effective approach for feedstocks with reasonably high reactivities, which produced conditions sufficient for carbon mineralization. However, difficulties were experienced when feedstocks contained low initial TIC and reactivity, resulting in inconclusive carbon verification through this method. Solubility trapping occurred in all columns to varying extents as monitored by DIC concentrations. CO_2 flux measurements were useful in the most reactive columns but would require near-continuous monitoring, limiting its use in some settings. This study also demonstrated that in addition to carbon verification, this column design could be used for monitoring the drainage chemistry of feedstocks, which is an essential consideration for deleterious metals like Ni and Cr and nutrients like P and K. The results of this study emphasize the need for a more comprehensive approach to carbon verification in ERW and in engineered systems like mine sites, which can be facilitated through field-deployable leaching columns.

3.6 References

Acero, P., Ayora, C., Carrera, J., 2007. Coupled thermal, hydraulic and geochemical evolution of pyritic tailings in unsaturated column experiments. Geochim. Cosmochim. Acta 71, 5325–5338. https://doi.org/10.1016/j.gca.2007.09.007

Amann, T., Hartmann, J., 2022. Carbon Accounting for Enhanced Weathering. Front. Clim. 4, 1–9. https://doi.org/10.3389/fclim.2022.849948

Amann, T., Hartmann, J., Hellmann, R., Trindade Pendrosa, E., Malik, A., 2022. Enhanced weathering potentials — the role of in situ CO_2 and grain size distribution. Front. Clim.

Amann, T., Hartmann, J., Struyf, E., De Oliveira Garcia, W., Fischer, E.K., Janssens, I., Meire, P., Schoelynck, J., 2020. Enhanced Weathering and related element fluxes - A cropland mesocosm approach. Biogeosciences 17, 103–119. https://doi.org/10.5194/bg-17-103-2020

Anda, M., Shamshuddin, J., Fauziah, C.I., 2015. Improving chemical properties of a highly weathered soil using finely ground basalt rocks. Catena 124, 147–161. https://doi.org/10.1016/j.catena.2014.09.012

Anda, M., Shamshuddin, J., Fauziah, C.I., 2013. Increasing negative charge and nutrient contents of a highly weathered soil using basalt and rice husk to promote cocoa growth under field conditions. Soil Tillage Res. 132, 1–11. https://doi.org/10.1016/j.still.2013.04.005

Andrews, M.G., Taylor, L.L., 2019. Combating Climate Change Through Enhanced Weathering of Agricultural Soils. Elements 15, 253–258. https://doi.org/10.2138/gselements.15.4.253

Assima, G.P., Larachi, F., Molson, J., Beaudoin, G., 2014. New tools for stimulating dissolution and carbonation of ultramafic mining residues. Can. J. Chem. Eng. https://doi.org/10.1002/cjce.22066

Bea, S.A., Wilson, S.A., Mayer, K.U., Dipple, G.M., Power, I.M., Gamazo, P., 2012. Reactive Transport Modeling of Natural Carbon Sequestration in Ultramafic Mine Tailings. Vadose Zo. J. 11, vzj2011.0053. https://doi.org/10.2136/vzj2011.0053

Beerling, D.J., Kantzas, E.P., Lomas, M.R., Wade, P., Eufrasio, R.M., Renforth, P., Sarkar, B., Andrews, M.G., James, R.H., Pearce, C.R., Mercure, J.F., Pollitt, H., Holden, P.B., Edwards, N.R., Khanna, M., Koh, L., Quegan, S., Pidgeon, N.F., Janssens, I.A., Hansen, J., Banwart, S.A., 2020. Potential for large-scale CO_2 removal via enhanced rock weathering with croplands. Nature 583, 242–248. https://doi.org/10.1038/s41586-020-2448-9

Beerling, D.J., Leake, J.R., Long, S.P., Scholes, J.D., Ton, J., Nelson, P.N., Bird, M., Kantzas, E., Taylor, L.L., Sarkar, B., Kelland, M., DeLucia, E., Kantola, I., Müller, C., Rau, G., Hansen, J., 2018. Farming with crops and rocks to address global climate, food and soil security /631/449 /706/1143 /704/47 /704/106 perspective. Nat. Plants 4, 138–147. https://doi.org/10.1038/s41477-018-0108-y

Bénézeth, P., Saldi, G.D., Dandurand, J.L., Schott, J., 2011. Experimental determination of the solubility product of magnesite at 50 to 200°C. Chem. Geol. 286, 21–31. https://doi.org/10.1016/j.chemgeo.2011.04.016

Brander, M., Ascui, F., Scott, V., Tett, S., 2021. Carbon accounting for negative emissions technologies. Clim. Policy 21, 699–717. https://doi.org/10.1080/14693062.2021.1878009

Brown, P.L., Drummond, S.E., Palmer, D.A., 1996. Hydrolysis of magnesium(II) at elevated temperatures. J. Chem. Soc. - Dalt. Trans. 3071–3075. https://doi.org/10.1039/dt9960003071

Buckingham, F., Henderson, G.M., Holdship, P., Renforth, P., 2022. Soil core study indicates limited CO_2 removal by enhanced weathering in dry croplands in the UK. Appl. Geochemistry 105482. https://doi.org/10.1016/j.apgeochem.2022.105482

Bullock, L.A., James, R.H., Matter, J., Renforth, P., Teagle, D.A.H., Bullock, L.A., 2021. Global Carbon Dioxide Removal Potential of Waste Materials From Metal and Diamond Mining 3, 1–12. https://doi.org/10.3389/fclim.2021.694175

Daval, D., Hellmann, R., Martinez, I., Gangloff, S., Guyot, F., 2013. Lizardite serpentine dissolution kinetics as a function of pH and temperature, including effects of elevated pCO_2. Chem. Geol. https://doi.org/10.1016/j.chemgeo.2013.05.020

De Baere, B., François, R., Mayer, K.U., 2015. Measuring mineral dissolution kinetics using on-line flow-through time resolved analysis (FT-TRA): An exploratory study with forsterite. Chem. Geol. 413, 107–118. https://doi.org/10.1016/j.chemgeo.2015.08.024

Dietzen, C., Harrison, R., Michelsen-Correa, S., 2018. Effectiveness of enhanced mineral weathering as a carbon sequestration tool and alternative to agricultural lime: An incubation experiment. Int. J. Greenh. Gas Control 74, 251–258. https://doi.org/10.1016/j.ijggc.2018.05.007

Entezari Zarandi, A., Larachi, F., Beaudoin, G., Plante, B., Sciortino, M., 2016. Multivariate study of the dynamics of CO_2 reaction with brucite-rich ultramafic mine tailings. Int. J. Greenh. Gas Control 52, 110–119.

https://doi.org/10.1016/j.ijggc.2016.06.022

Flipkens, G., Blust, R., Town, R.M., 2021. Deriving Nickel (Ni(II)) and Chromium (Cr(III)) Based Environmentally Safe Olivine Guidelines for Coastal Enhanced Silicate Weathering. Environ. Sci. Technol. 55, 12362–12371. https://doi.org/10.1021/acs.est.1c02974

Gautier, Q., Bénézeth, P., Mavromatis, V., Schott, J., 2014. Hydromagnesite solubility product and growth kinetics in aqueous solution from 25 to 75°C. Geochim. Cosmochim. Acta 138, 1–20. https://doi.org/10.1016/j.gca.2014.03.044

Giammar, D.E., Bruant, R.G., Peters, C.A., 2005. Forsterite dissolution and magnesite precipitation at conditions relevant for deep saline aquifer storage and sequestration of carbon dioxide. Chem. Geol. https://doi.org/10.1016/j.chemgeo.2004.12.013

Gilfillan, S.M.V., Lollar, B.S., Holland, G., Blagburn, D., Stevens, S., Schoell, M., Cassidy, M., Ding, Z., Zhou, Z., Lacrampe-Couloume, G., Ballentine, C.J., 2009. Solubility trapping in formation water as dominant CO_2 sink in natural gas fields. Nature 458, 614–618. https://doi.org/10.1038/nature07852

Gras, A., Beaudoin, G., Molson, J., Plante, B., Bussière, B., Lemieux, J.M., Dupont, P.P., 2017. Isotopic evidence of passive mineral carbonation in mine wastes from the Dumont Nickel Project (Abitibi, Quebec). Int. J. Greenh. Gas Control 60, 10–23. https://doi.org/10.1016/j.ijggc.2017.03.002

Hamilton, J.L., Wilson, S.A., Turvey, C.C., Morgan, B., Tait, A.W., McCutcheon, J., Fallon, S.J., Southam, G., 2021. Carbon accounting of mined landscapes, and deployment of a geochemical treatment system for enhanced weathering at Woodsreef Chrysotile Mine, NSW, Australia. J. Geochemical Explor. 220.

https://doi.org/10.1016/j.gexplo.2020.106655

Hänchen, M., Prigiobbe, V., Baciocchi, R., Mazzotti, M., 2008. Precipitation in the Mg-carbonate system-effects of temperature and CO_2 pressure. Chem. Eng. Sci. 63, 1012–1028. https://doi.org/10.1016/j.ces.2007.09.052

Hangx, S.J.T., Spiers, C.J., 2009. Coastal spreading of olivine to control atmospheric CO_2 concentrations: A critical analysis of viability. Int. J. Greenh. Gas Control 3, 757–767. https://doi.org/10.1016/j.ijggc.2009.07.001

Haque, F., Chiang, Y.W., Santos, R.M., 2020a. Risk assessment of Ni, Cr, and Si release from alkaline minerals during enhanced weathering. Open Agric. 5, 166–175. https://doi.org/10.1515/opag-2020-0016

Haque, F., Santos, R.M., Chiang, Y.W., 2020b. CO_2 sequestration by wollastonite-amended agricultural soils – An Ontario field study. Int. J. Greenh. Gas Control. https://doi.org/10.1016/j.ijggc.2020.103017

Haque, F., Santos, R.M., Chiang, Y.W., 2020c. CO2 sequestration by wollastonite-amended agricultural soils – An Ontario field study. Int. J. Greenh. Gas Control 97, 103017. https://doi.org/10.1016/j.ijggc.2020.103017

Haque, F., Santos, R.M., Dutta, A., Thimmanagari, M., Chiang, Y.W., 2019. Co-Benefits of Wollastonite Weathering in Agriculture: CO_2 Sequestration and Promoted Plant Growth. ACS Omega 4, 1425–1433. https://doi.org/10.1021/acsomega.8b02477

Harrison, A.L., Dipple, G.M., Power, I.M., Mayer, K.U., 2015. Influence of surface passivation and water content on mineral reactions in unsaturated porous media: Implications for brucite carbonation and CO_2 sequestration. Geochim. Cosmochim. Acta 148, 477–495. https://doi.org/10.1016/j.gca.2014.10.020

Harrison, A.L., Mavromatis, V., Oelkers, E.H., Bénézeth, P., 2019. Solubility of the hydrated Mg-carbonates nesquehonite and dypingite from 5 to 35 °C: Implications for CO_2 storage and the relative stability of Mg-carbonates. Chem. Geol. 504, 123–135. https://doi.org/10.1016/j.chemgeo.2018.11.003

Hartmann, J., West, A.J., Renforth, P., Köhler, P., De La Rocha, C.L., Wolf-Gladrow, D.A., Dürr, H.H., Scheffran, J., 2013. Enhanced chemical weathering as a geoengineering strategy to reduce atmospheric carbon dioxide, supply nutrients, and mitigate ocean acidification. Rev. Geophys. https://doi.org/10.1002/rog.20004

Honegger, M., Poralla, M., Michaelowa, A., Ahonen, H.M., 2021. Who Is Paying for Carbon Dioxide Removal? Designing Policy Instruments for Mobilizing Negative Emissions Technologies. Front. Clim. 3, 1–15. https://doi.org/10.3389/fclim.2021.672996

Horri, N., Sanz-Pérez, E.S., Arencibia, A., Sanz, R., Frini-Srasra, N., Srasra, E., 2020. Effect of acid activation on the CO_2 adsorption capacity of montmorillonite. Adsorption 26, 793–811. https://doi.org/10.1007/s10450-020-00200-z

Hövelmann, J., Putnis, C. V., Ruiz-Agudo, E., Austrheim, H., 2012. Direct nanoscale observations of CO_2 sequestration during brucite [Mg(OH)2] dissolution. Environ. Sci. Technol. 46, 5253–5260. https://doi.org/10.1021/es300403n

Islam, A., White, R.E., Chen, D., 2006. Nitrification activity in acid soils of north-eastern Victoria, Australia, as affected by liming and phosphorus fertilisation. Aust. J. Soil Res. 44, 739–744. https://doi.org/10.1071/SR06058

Kabata-Pendias, A., 2000. Trace Elements in Soils and Plants, 3rd ed. CRC Press. https://doi.org/10.1136/bmj.2.4640.1355-a

Kandji, E.H.B., Plante, B., Bussière, B., Beaudoin, G., Dupont, P.P., 2017. Kinetic testing to evaluate the mineral carbonation and metal leaching potential of ultramafic tailings: Case study of the Dumont Nickel Project, Amos, Québec. Appl. Geochemistry 84, 262–276. https://doi.org/10.1016/j.apgeochem.2017.07.005

Kantola, I.B., Masters, M.D., Beerling, D.J., Long, S.P., DeLucia, E.H., 2017. Potential of global croplands and bioenergy crops for climate change mitigation through deployment for enhanced weathering. Biol. Lett. 13. https://doi.org/10.1098/rsbl.2016.0714

Komadel, P., 2003. Chemically modified smectites. Clay Miner. 38, 127–138. https://doi.org/10.1180/0009855033810083

Krüger, L., 2007. Technical Note TN 2007-07-01 KIMBERLITE AS LOW GRADE FERTILIZER - A REVIEW 1–20.

Lechat, K., Lemieux, J.M., Molson, J., Beaudoin, G., Hébert, R., 2016. Field evidence of CO2 sequestration by mineral carbonation in ultramafic milling wastes, Thetford Mines, Canada. Int. J. Greenh. Gas Control 47, 110–121. https://doi.org/10.1016/j.ijggc.2016.01.036

Liu, Z., Dreybrodt, W., Liu, H., 2011. Atmospheric CO_2 sink: Silicate weathering or carbonate weathering? Appl. Geochemistry 26, S292–S294. https://doi.org/10.1016/j.apgeochem.2011.03.085

Loring, J.S., Schaef, H.T., Turcu, R.V.F., Thompson, C.J., Miller, Q.R.S., Martin, P.F., Hu, J., Hoyt, D.W., Qafoku, O., Ilton, E.S., Felmy, A.R., Rosso, K.M., 2012. In situ molecular spectroscopic evidence for CO_2 intercalation into montmorillonite in supercritical carbon dioxide. Langmuir 28, 7125–7128.

https://doi.org/10.1021/la301136w

Lu, X., Carroll, K.J., Turvey, C.C., Dipple, G.M., 2022. Rate and capacity of cation release from ultramafic mine tailings for carbon capture and storage. Appl. Geochemistry 140, 105285. https://doi.org/10.1016/j.apgeochem.2022.105285

McClain, C.N., Maher, K., 2016. Chromium fluxes and speciation in ultramafic catchments and global rivers. Chem. Geol. 426, 135–157. https://doi.org/10.1016/j.chemgeo.2016.01.021

McKelvy, Chizmeshya, A.V.G., Squires, K., Carpenter, R.W., Bearat, H., 2005. A Novel Approach to Mineral Carbonation: Enhancing Carbonation While Avoid- ing Mineral Pretreatment Process Cost.

Mervine, E.M., Wilson, S.A., Power, I.M., Dipple, G.M., Turvey, C.C., Hamilton, J.L., Vanderzee, S., Raudsepp, M., Southam, C., Matter, J.M., Kelemen, P.B., Stiefenhofer, J., Miya, Z., Southam, G., 2018. Potential for offsetting diamond mine carbon emissions through mineral carbonation of processed kimberlite: an assessment of De Beers mine sites in South Africa and Canada. Mineral. Petrol. 112, 755–765. https://doi.org/10.1007/s00710-018-0589-4

Meysman, F.J.R., Montserrat, F., 2017. Negative CO_2 emissions via enhanced silicate weathering in coastal environments. Biol. Lett. 13. https://doi.org/10.1098/rsbl.2016.0905

Michels, L., Fossum, J.O., Rozynek, Z., Hemmen, H., Rustenberg, K., Sobas, P.A., Kalantzopoulos, G.N., Knudsen, K.D., Janek, M., Plivelic, T.S., Da Silva, G.J., 2015. Intercalation and retention of carbon dioxide in a smectite clay promoted by interlayer cations. Sci. Rep. 5, 2–10. https://doi.org/10.1038/srep08775

Minx, J.C., Lamb, W.F., Callaghan, M.W., Fuss, S., Hilaire, J., Creutzig, F., Amann, T., Beringer, T., De Oliveira Garcia, W., Hartmann, J., Khanna, T., Lenzi, D., Luderer, G., Nemet, G.F., Rogelj, J., Smith, P., Vicente Vicente, J.L., Wilcox, J., Del Mar Zamora Dominguez, M., 2018. Negative emissions - Part 1: Research landscape and synthesis. Environ. Res. Lett. 13. https://doi.org/10.1088/1748-9326/aabf9b

Mitchell, A.C., Dideriksen, K., Spangler, L.H., Cunningham, A.B., Gerlach, R., 2010. Microbially enhanced carbon capture and storage by mineral-trapping and solubility-trapping. Environ. Sci. Technol. 44, 5270–5276. https://doi.org/10.1021/es903270w

Montserrat, F., Renforth, P., Hartmann, J., Leermakers, M., Knops, P., Meysman, F.J.R., 2017. Olivine Dissolution in Seawater: Implications for CO_2 Sequestration through Enhanced Weathering in Coastal Environments. Environ. Sci. Technol. 51, 3960–3972. https://doi.org/10.1021/acs.est.6b05942

Nunes, J.M.G., Kautzmann, R.M., Oliveira, C., 2014. Evaluation of the natural fertilizing potential of basalt dust wastes from the mining district of Nova Prata (Brazil). J. Clean. Prod. https://doi.org/10.1016/j.jclepro.2014.04.032

Oelkers, E.H., Declercq, J., Saldi, G.D., Gislason, S.R., Schott, J., 2018. Olivine dissolution rates: A critical review. Chem. Geol. https://doi.org/10.1016/j.chemgeo.2018.10.008

Parkhurst, D., Appelo, C., 2013. Description of input and examples for PHREEQC Version 3 — A computer program for speciation, batch-reaction, one-dimensional transport, and inverse geochemical calculations. U.S. Geol. Surv. Tech. Methods 497.

Paulo, C., Power, I.M., Stubbs, A.R., Wang, B., Zeyen, N., Wilson, S.A., 2021.

Evaluating feedstocks for carbon dioxide removal by enhanced rock weathering and CO_2 mineralization. Appl. Geochemistry 129, 104955. https://doi.org/10.1016/j.apgeochem.2021.104955

Pokrovsky, O.S., Schott, J., 2000. Kinetics and mechanism of forsterite dissolution at 25 ° C and pH from 1 to 12. Geochim. Cosmochim. Acta 64, 3313–3325.

Pokrovsky, O.S., Shirokova, L.S., Bénézeth, P., Schott, J., Golubev, S. V., 2009. Effect of organic ligands and heterotrophic bacteria on wollastonite dissolution kinetics. Am. J. Sci. 309, 731–772. https://doi.org/10.2475/08.2009.05

Power, I.M., Harrison, A.L., Dipple, G.M., Wilson, S.A., Kelemen, P.B., Hitch, M., Southam, G., 2013. Carbon mineralization: From natural analogues to engineered systems. Rev. Mineral. Geochemistry 77, 305–360. https://doi.org/10.2138/rmg.2013.77.9

Power, I.M., McCutcheon, J., Harrison, A.L., Wilson, S.A., Dipple, G.M., Kelly, S., Southam, C., Southam, G., 2014. Strategizing carbon-neutral mines: A case for pilot projects, Minerals. https://doi.org/10.3390/min4020399

Power, I.M., Wilson, S.A., Thom, J.M., Dipple, G.M., Gabites, J.E., Southam, G., 2009. The hydromagnesite playas of Atlin, British Columbia, Canada: A biogeochemical model for CO_2 sequestration. Chem. Geol. 260, 286–300. https://doi.org/10.1016/j.chemgeo.2009.01.012

Renforth, P., 2012. The potential of enhanced weathering in the UK. Int. J. Greenh. Gas Control 10, 229–243. https://doi.org/10.1016/j.ijggc.2012.06.011

Renforth, P., Pogge von Strandmann, P.A.E., Henderson, G.M., 2015a. The dissolution of olivine added to soil: Implications for enhanced weathering. Appl. Geochemistry.

https://doi.org/10.1016/j.apgeochem.2015.05.016

Renforth, P., Pogge von Strandmann, P.A.E., Henderson, G.M., 2015b. The dissolution of olivine added to soil: Implications for enhanced weathering. Appl. Geochemistry 61, 109–118. https://doi.org/10.1016/j.apgeochem.2015.05.016

Rinder, T., von Hagke, C., 2021. The influence of particle size on the potential of enhanced basalt weathering for carbon dioxide removal - Insights from a regional assessment. J. Clean. Prod. 315. https://doi.org/10.1016/j.jclepro.2021.128178

Saldi, G.D., Jordan, G., Schott, J., Oelkers, E.H., 2009. Magnesite growth rates as a function of temperature and saturation state. Geochim. Cosmochim. Acta. https://doi.org/10.1016/j.gca.2009.06.035

Saldi, G.D., Schott, J., Pokrovsky, O.S., Gautier, Q., Oelkers, E.H., 2012. An experimental study of magnesite precipitation rates at neutral to alkaline conditions and 100-200°C as a function of pH, aqueous solution composition and chemical affinity. Geochim. Cosmochim. Acta 83, 93–109. https://doi.org/10.1016/j.gca.2011.12.005

Schott, J., Pokrovsky, O.S., Spalla, O., Devreux, F., Gloter, A., Mielczarski, J.A., 2012. Formation, growth and transformation of leached layers during silicate minerals dissolution: The example of wollastonite. Geochim. Cosmochim. Acta 98, 259–281. https://doi.org/10.1016/j.gca.2012.09.030

Schuiling, R.D., Krijgsman, P., 2006. Enhanced weathering: An effective and cheap tool to sequester CO_2. Clim. Change. https://doi.org/10.1007/s10584-005-3485-y

Shaaban, M., Peng, Q., Lin, S., Wu, Y., Zhao, J., Hu, R., 2014. Nitrous Oxide emission from two acidic soils as affected by dolomite application. Soil Res. 52, 841–848.

https://doi.org/10.1071/SR14129

Smith, P., Davis, S.J., Creutzig, F., Fuss, S., Minx, J., Gabrielle, B., Kato, E., Jackson, R.B., Cowie, A., Kriegler, E., Van Vuuren, D.P., Rogelj, J., Ciais, P., Milne, J., Canadell, J.G., McCollum, D., Peters, G., Andrew, R., Krey, V., Shrestha, G., Friedlingstein, P., Gasser, T., Grübler, A., Heidug, W.K., Jonas, M., Jones, C.D., Kraxner, F., Littleton, E., Lowe, J., Moreira, J.R., Nakicenovic, N., Obersteiner, M., Patwardhan, A., Rogner, M., Rubin, E., Sharifi, A., Torvanger, A., Yamagata, Y., Edmonds, J., Yongsung, C., 2016. Biophysical and economic limits to negative CO_2 emissions. Nat. Clim. Chang. https://doi.org/10.1038/nclimate2870

Smolders, E., Oorts, K., Van Sprang, P., Schoeters, I., Janssen, C.R., McGrath, S.P., McLaughlin, M.J., 2009. Toxicity of trace metals in soil as affected by soil type and aging after contamination: Using calibrated bioavailability models to set ecological soil standards. Environ. Toxicol. Chem. 28, 1633–1642. https://doi.org/10.1897/08-592.1

Soubrand-Colin, M., Neel, C., Bril, H., Grosbois, C., Caner, L., 2007. Geochemical behaviour of Ni, Cr, Cu, Zn and Pb in an Andosol-Cambisol climosequence on basaltic rocks in the French Massif Central. Geoderma 137, 340–351. https://doi.org/10.1016/j.geoderma.2006.08.017

Strefler, J., Amann, T., Bauer, N., Kriegler, E., Hartmann, J., 2018a. Potential and costs of carbon dioxide removal by enhanced weathering of rocks. Environ. Res. Lett. 13. https://doi.org/10.1088/1748-9326/aaa9c4

Strefler, J., Bauer, N., Kriegler, E., Popp, A., Giannousakis, A., Edenhofer, O., 2018b. Between Scylla and Charybdis: Delayed mitigation narrows the passage between

large-scale CDR and high costs. Environ. Res. Lett. 13. https://doi.org/10.1088/1748-9326/aab2ba

Stubbs, A.R., Paulo, C., Power, I.M., Wang, B., Zeyen, N., Wilson, S.A., 2022. Direct measurement of CO2 drawdown in mine wastes and rock powders: Implications for enhanced rock weathering. Int. J. Greenh. Gas Control 113. https://doi.org/10.1016/j.ijggc.2021.103554

Taylor, Driscoll, C.T., Gro, P.M., Rau, G.H., Blum, J.D., 2021. Increased carbon capture by a silicate- treated forested watershed a ! ected by acid deposition Appendix A : Contributions of rain and snow precipitation to stream-water chemistry Appendix B : Fraction of calcium derived from wollastonite 2, 8–10.

Taylor, L.L., Driscoll, C.T., Groffman, P.M., Rau, G.H., Blum, J.D., Beerling, D.J., 2021. Increased carbon capture by a silicate-treated forested watershed affected by acid deposition. Biogeosciences 18, 169–188. https://doi.org/10.5194/bg-18-169-2021

ten Berge, H.F.M., van der Meer, H.G., Steenhuizen, J.W., Goedhart, P.W., Knops, P., Verhagen, J., 2012. Olivine weathering in soil, and its effects on growth and nutrient uptake in ryegrass (Lolium perenne L.): A pot experiment. PLoS One. https://doi.org/10.1371/journal.pone.0042098

Thom, J.G.M., Dipple, G.M., Power, I.M., Harrison, A.L., 2013. Chrysotile dissolution rates: Implications for carbon sequestration. Appl. Geochemistry 35, 244–254. https://doi.org/10.1016/j.apgeochem.2013.04.016

Turvey, C.C., Wilson, S.A., Hamilton, J.L., Tait, A.W., McCutcheon, J., Beinlich, A., Fallon, S.J., Dipple, G.M., Southam, G., 2018. Hydrotalcites and hydrated Mg-carbonates as carbon sinks in serpentinite mineral wastes from the Woodsreef

chrysotile mine, New South Wales, Australia: Controls on carbonate mineralogy and efficiency of CO_2 air capture in mine tailings. Int. J. Greenh. Gas Control 79, 38–60. https://doi.org/10.1016/j.ijggc.2018.09.015

Van Straaten, P., 2006. Farming with rocks and minerals: Challenges and opportunities. An. Acad. Bras. Cienc. 78, 731–747. https://doi.org/10.1590/S0001-37652006000400009

Vasiluk, L., Sowa, J., Sanborn, P., Ford, F., Dutton, M.D., Hale, B., 2019. Bioaccessibility estimates by gastric SBRC method to determine relationships to bioavailability of nickel in ultramafic soils. Sci. Total Environ. 673, 685–693. https://doi.org/10.1016/j.scitotenv.2019.04.059

Wang, J., Jin, S., Bai, W., Li, Y., Jin, Y., 2016. Comparative analysis of the international carbon verification policies and systems. Nat. Hazards 84, 381–397. https://doi.org/10.1007/s11069-016-2593-5

Wilson, S.A., Dipple, G.M., Power, I.M., Barker, S.L.L., Fallon, S.J., Southam, G., 2011. Subarctic weathering of mineral wastes provides a sink for atmospheric CO_2. Environ. Sci. Technol. https://doi.org/10.1021/es202112y

Wilson, S.A., Dipple, G.M., Power, I.M., Thom, J.M., Anderson, R.G., Raudsepp, M., Gabites, J.E., Southam, G., 2009. Carbon dioxide fixation within mine wastes of ultramafic-hosted ore deposits: Examples from the Clinton Creek and Cassiar Chrysotile deposits, Canada. Econ. Geol. 104, 95–112. https://doi.org/10.2113/gsecongeo.104.1.95

Wilson, S.A., Harrison, A.L., Dipple, G.M., Power, I.M., Barker, S.L.L., Ulrich Mayer, K., Fallon, S.J., Raudsepp, M., Southam, G., 2014. Offsetting of CO_2 emissions by

air capture in mine tailings at the Mount Keith Nickel Mine, Western Australia: Rates, controls and prospects for carbon neutral mining. Int. J. Greenh. Gas Control 25, 121–140. https://doi.org/10.1016/j.ijggc.2014.04.002

Wood, C., Harrison, A.L., Power, I.M., 2022. Impacts of dissolved phosphorus and soil-mineral-fluid interactions on CO_2 removal through enhanced weathering of wollastonite in soils. Appl. Geochemistry 148, 105511. https://doi.org/10.1016/j.apgeochem.2022.105511

Zeyen, N., Wang, B., Wilson, S.A., Paulo, C., Stubbs, A.R., Power, I.M., Steele-MacInnis, M., Lanzirotti, A., Newville, M., Paterson, D.J., Hamilton, J.L., Jones, T.R., Turvey, C.C., Dipple, G.M., Southam, G., 2022. Cation Exchange in Smectites as a New Approach to Mineral Carbonation. Front. Clim. 4. https://doi.org/10.3389/fclim.2022.913632

Chapter 4
Conclusions

Negative emissions technologies (NETs) are necessary to limit Earth's warming to no more than 1.5 ºC above pre-industrial levels (Beuttler et al., 2019). If widely adopted, implementing these technologies can potentially lead to net-negative emissions by 2070 (IPCC, 2018). Enhanced rock weathering (ERW) and mineralization are approaches for reducing CO_2 concentrations via their sequestration and storage as a dissolved phase (e.g. HCO_3^-) or a solid phase (carbonate minerals). While these processes are recognized as a potentially valuable NET (Brander et al., 2021; Minx et al., 2018), there remain questions regarding the numerous rock types that may be employed under various climatic conditions and challenges with quantifying CO_2 removal rates. This thesis aimed to explore improvements for predicting and monitoring CO_2 sequestration rates in suitable feedstocks, including kimberlite, wollastonite, and olivine, while assessing the release of deleterious metals and nutrients.

4.1 Summary of research outcomes

Chapter 2 research demonstrated that batch leaches are a valuable tool for assessing feedstock reactivity and can provide estimates of CO_2 sequestration potentials for a range of rocks and minerals. This approach allows for a rapid evaluation when coupled with traditional characterization methods, including X-ray diffraction (mineralogy), total inorganic carbon (TIC), and X-ray fluorescence spectroscopy (geochemistry), the latter can be used to calculate CO_2 sequestration capacity based on complete carbonation of MgO and CaO contents. Some variables that control the results

were identified, which can be exploited for increasing CO_2 sequestration in these samples. Most prominently, grain size and surface area influence feedstock reactivity. For example, olivine sand samples (OLI) boasted the highest capacity for CO_2 sequestration yet the lowest potentials, owing to a grain size ~42 times larger than what other studies deem requisite for adequate dissolution. Additionally, we found that most of the kimberlites analyzed have the potential to sequester large quantities of CO_2 at the scale they are produced. Thus, demonstrating their value as targets for ERW and CO_2 mineralization.

A secondary objective of the research in Chapter 2 was to evaluate the release of elements of concern (Ni and Cr) and potential nutrients (P and K) during weathering. Results show a low release of Ni and Cr from most kimberlites, coupled with the promising release of P and K. Of the other feedstocks analyzed, only the metabasalt (MBA) could provide such results. While these leach tests demonstrate their ability to quantify easily released elements, the context in which the results can be used is largely outside this study's scope. For example, concentrations of Ni and Cr require the context of the characteristics of the soils into which they are being released for relevant determinations to be made about the risk they pose to the environment. Nevertheless, these leaches accurately assess a feedstocks ability to release these elements, exhibiting their value as a characterization method.

In Chapter 3, field deployable leaching columns were established as a valuable tool for monitoring CO_2 sequestration rates and drainage chemistry of rock and mineral feedstocks. The results of GK and WOL in Chapter 3 proved the most productive, as both feedstocks provided significant CO_2 sequestration, primarily through mineral trapping.

Thus, feedstocks with relatively high reactivity, labile components, and low TIC offer favourable conditions for field deployable drainage columns. Moreover, the results of this chapter showed that combining mineral trapping, determined through TIC, and solubility trapping, determined through DIC, is essential for accurate carbon accounting.

As expected, CO_2 removal rates were mainly based on feedstock characteristics (e.g., grain size, surface area, mineralogy), which can negate the effectiveness of monitoring tools. As such, OLI and DVK columns posed more issues for rate determination than GK and WOL. The importance of TIC is emphasized by the results of this chapter, as demonstrated by the CO_2 sequestration rate of OLI, which changes drastically if TIC is considered to be within error, and solubility trapping is the main pathway for sequestration. Moreover, discrepancies between TIC loss and the Ca concentrations found in the leachate of DVK indicate "missed" carbonate precipitation within the apparatus, which would drastically change its carbon balance.

4.2 Applications of leaching columns

Predicting leachate chemistry from rock and mineral feedstocks using batch laboratory testing is advantageous for both mining and ERW. Despite similar practices often being used for mining operations (e.g., acid-base accounting), the methodologies used in this study were developed for assessing CO_2 removal. Introducing the leaches used in Chapter 2 to the current array of mining and ERW characterization methods allows for a higher confidence level in feedstock selection by providing an otherwise speculative dataset, based on standard methodologies. While predicting the release of elements of interest is often inconsequential in a mining setting due to the prevalence of monitoring and drainage water containment, it is essential to make informed

determinations about the suitability of powdered rocks and minerals for ERW prior to application at sites, e.g., agricultural fields.

The field-deployable columns used in Chapter 3 can be used for monitoring carbon removal, a challenge in ERW settings and something currently not done at mines. Monitoring CO_2 sequestration at mines often relies on large-scale sampling campaigns, like quantitative mineralogical assessments conducted by Wilson et al. (2014), which required almost 1000 solid samples to determine passive sequestration rates at the Mount Keith Nickel Mine. Additionally, columns are a passive method that does not interfere with regular mining practices and may be an attractive option for mine operators. Coupling these columns with the leaches of Chapter 2 starts to define a framework for large-scale carbon removal projects using rock and mineral feedstocks by improving feedstock selection and increasing the resolution at which CO_2 removal can be monitored.

4.3 Applications of feedstocks

4.3.1 Mining

An estimated 13 Gt of tailings with the potential to be used as feedstocks for CO_2 sequestration are generated annually (Bullock et al., 2021), some of which are represented in Chapters 2 and 3 of this thesis. While the mafic and ultramafic mine wastes used in this study are generally considered suitable feedstocks for CO_2 sequestration, there are many other types of deposits which have not been assessed, and it is unclear whether or not they should be used. Feedstock mineralogy and its corresponding reactivity are crucial to determining CO_2 sequestration potential. The highest values were observed in MKM, which contained the most reactive target mineral, brucite. Furthermore, the results of kimberlite indicated good sequestration capacity and

potential in all samples, with the exemption of VSD T3 and VSD T5, due to their lack of reactive mineral phases. However, the results of the leaches were not always in agreement with the results of measured CO_2 sequestration in the field deployable leaching columns. As such, we saw good sequestration rates from GK columns, while poor rates were observed in DVK, despite similar CO_2 sequestration potentials determined through the leaches. Thus, issues with instrumentation are to blame, with the potential for "missed" carbonate precipitation being likely.

4.3.2 Enhanced rock weathering

ERW is the acceleration of natural silicate weathering, which is an important component of Earth's carbon cycle (Amann et al., 2020; Strefler et al., 2018a). However, the suitability of silicate rocks varies greatly and depends on the characteristics of the minerals present. WOL, comprised mainly of wollastonite, yielded the highest CO_2 sequestration potential of all ERW feedstocks, supported by its high rate of sequestration measured in the drainage columns. As such, wollastonite is an excellent feedstock for ERW (Di Lorenzo et al., 2018; Haque et al., 2020c; Wood et al., 2022), and is even more reactive than olivine (Beerling et al., 2018; Montserrat et al., 2017; Renforth et al., 2015b). Despite high sequestration capacity based on whole rock geochemistry, the olivine sand used in our study showed very low CO_2 sequestration potential and presented issues with monitoring its rates due largely to its physical characteristics. Thus, demonstrating the importance of grain size and surface area, even in feedstocks with comparatively high reactivities.

Another critical aspect of ERW is the release of elements that may be a detriment or a benefit to the environment. As such, feedstock selection should be not just predicated

on the CO_2 sequestration they can provide but also consider the potential impacts that their weathering may cause. We found that all ERW feedstocks released Ni at a low rate, and while Cr release was higher in these feedstocks when compared to mine wastes, the values were still <1 mg/kg. Moreover, when exposed to realistic weathering conditions, OLI and WOL released Ni and Cr at a scale less than 5 µg/kg, indicating their safety for widespread use.

4.4 Suggestions for future research

Future research should apply the methodologies that proved valuable in this study to mine and ERW sites. Introducing context into the leaching tests of Chapter 2 would elucidate results that apply to one's specific plan for large-scale ERW. Examples of context could include climatic conditions experienced at the dispersal site, expected rates of application, and soil parameters, with the latter being most prevalent for determinations of elements of interest. Additionally, further investigation into the fate of deleterious metals should be considered and not limited to Ni and Cr, which have been the focus of most ERW studies. Guidelines for maximum acceptable dosages of ERW feedstocks should also be determined, with batch leaches used as a critical tool for this assessment.

The major findings of this thesis show that leaching columns can be used to determine rates of CO_2 sequestration in some feedstocks accurately. Future research should assess the applicability of these columns to monitor large-scale processes where other variables are introduced to the system. For example, constructing these columns to replicate the wollastonite field trials conducted by Haque et al. (2020), which considered mineral trapping alone, and Taylor et al. (2021), which considered solubility trapping

alone, could enhance the resolution of CO_2 sequestration rates by considering multiple pathways. Moreover, these columns could be deployed at mine sites to monitor carbon additions to the system under accurate climatic conditions in a way that is representative of the study area. For example, this could include multiple columns for each impoundment that account for the variable homogeneity of kimberlite residues and changing deposition practices. Additionally, columns can be set up that represent potential enhancements that can be made to the processing circuit and storage conditions of residues to facilitate CO_2 sequestration, which would allow for a higher level of decision-making regarding these changes. Finally, implementing these methods would contribute to the overall understanding of carbon sequestration via enhanced rock weathering and CO_2 mineralization, aiding in its validation and adoption as a preeminent negative emission technology.

4.5 References

Allen, M.R., O.P. Dube, W. Solecki, F. Aragón-Durand, W. Cramer, S. Humphreys, M. Kainuma, J. Kala, N. Mahowald, Y. Mulugetta, R. Perez, M. Wairiu, and K.Z., 2018. Special report: Global warming of 1.5 degrees celcius. IPCC Spec. Rep. 368.

Amann, T., Hartmann, J., Struyf, E., De Oliveira Garcia, W., Fischer, E.K., Janssens, I., Meire, P., Schoelynck, J., 2020. Enhanced Weathering and related element fluxes - A cropland mesocosm approach. Biogeosciences 17, 103–119. https://doi.org/10.5194/bg-17-103-2020

Beerling, D.J., Leake, J.R., Long, S.P., Scholes, J.D., Ton, J., Nelson, P.N., Bird, M., Kantzas, E., Taylor, L.L., Sarkar, B., Kelland, M., DeLucia, E., Kantola, I., Müller, C., Rau, G., Hansen, J., 2018. Farming with crops and rocks to address global climate, food and soil security /631/449 /706/1143 /704/47 /704/106 perspective. Nat. Plants 4, 138–147. https://doi.org/10.1038/s41477-018-0108-y

Beuttler, C., Charles, L., Wurzbacher, J., 2019. The Role of Direct Air Capture in Mitigation of Anthropogenic Greenhouse Gas Emissions. Front. Clim. 1, 1–7. https://doi.org/10.3389/fclim.2019.00010

Brander, M., Ascui, F., Scott, V., Tett, S., 2021. Carbon accounting for negative emissions technologies. Clim. Policy 21, 699–717. https://doi.org/10.1080/14693062.2021.1878009

Bullock, L.A., James, R.H., Matter, J., Renforth, P., Teagle, D.A.H., Bullock, L.A., 2021. Global Carbon Dioxide Removal Potential of Waste Materials From Metal and Diamond Mining 3, 1–12. https://doi.org/10.3389/fclim.2021.694175

Di Lorenzo, F., Ruiz-Agudo, C., Ibañez-Velasco, A., Gil-San Millán, R., Navarro, J.A.R.,

Ruiz-Agudo, E., Rodriguez-Navarro, C., 2018. The carbonation of wollastonite: A model reaction to test natural and biomimetic catalysts for enhanced CO_2 sequestration. Minerals. https://doi.org/10.3390/min8050209

Haque, F., Santos, R.M., Chiang, Y.W., 2020. CO2 sequestration by wollastonite-amended agricultural soils – An Ontario field study. Int. J. Greenh. Gas Control 97, 103017. https://doi.org/10.1016/j.ijggc.2020.103017

Minx, J.C., Lamb, W.F., Callaghan, M.W., Fuss, S., Hilaire, J., Creutzig, F., Amann, T., Beringer, T., De Oliveira Garcia, W., Hartmann, J., Khanna, T., Lenzi, D., Luderer, G., Nemet, G.F., Rogelj, J., Smith, P., Vicente Vicente, J.L., Wilcox, J., Del Mar Zamora Dominguez, M., 2018. Negative emissions - Part 1: Research landscape and synthesis. Environ. Res. Lett. 13. https://doi.org/10.1088/1748-9326/aabf9b

Montserrat, F., Renforth, P., Hartmann, J., Leermakers, M., Knops, P., Meysman, F.J.R., 2017. Olivine Dissolution in Seawater: Implications for CO_2 Sequestration through Enhanced Weathering in Coastal Environments. Environ. Sci. Technol. 51, 3960–3972. https://doi.org/10.1021/acs.est.6b05942

Power, I.M., McCutcheon, J., Harrison, A.L., Wilson, S.A., Dipple, G.M., Kelly, S., Southam, C., Southam, G., 2014. Strategizing carbon-neutral mines: A case for pilot projects, Minerals. https://doi.org/10.3390/min4020399

Renforth, P., Pogge von Strandmann, P.A.E., Henderson, G.M., 2015. The dissolution of olivine added to soil: Implications for enhanced weathering. Appl. Geochemistry 61, 109–118. https://doi.org/10.1016/j.apgeochem.2015.05.016

Strefler, J., Amann, T., Bauer, N., Kriegler, E., Hartmann, J., 2018. Potential and costs of carbon dioxide removal by enhanced weathering of rocks. Environ. Res. Lett. 13.

https://doi.org/10.1088/1748-9326/aaa9c4

Taylor, L.L., Driscoll, C.T., Groffman, P.M., Rau, G.H., Blum, J.D., Beerling, D.J., 2021. Increased carbon capture by a silicate-treated forested watershed affected by acid deposition. Biogeosciences 18, 169–188. https://doi.org/10.5194/bg-18-169-2021

Wilson, S.A., Harrison, A.L., Dipple, G.M., Power, I.M., Barker, S.L.L., Ulrich Mayer, K., Fallon, S.J., Raudsepp, M., Southam, G., 2014. Offsetting of CO_2 emissions by air capture in mine tailings at the Mount Keith Nickel Mine, Western Australia: Rates, controls and prospects for carbon neutral mining. Int. J. Greenh. Gas Control 25, 121–140. https://doi.org/10.1016/j.ijggc.2014.04.002

Wood, C., Harrison, A.L., Power, I.M., 2022. Impacts of dissolved phosphorus and soil-mineral-fluid interactions on CO_2 removal through enhanced weathering of wollastonite in soils. Appl. Geochemistry 148, 105511. https://doi.org/10.1016/j.apgeochem.2022.105511